The Astrophysical Journal, 966:160 (31pp), 2024 May 10 https://doi.org/10.3847/1538-4357/ad2f9f

A Systematic Analysis of the X-Ray Emission in Optically Selected Tidal Disruption Events: Observational Evidence for the Unification of the Optically and X-Ray-selected Populations

Muryel Guolo[1], Suvi Gezari[1,2], Yuhan Yao[3,4,5], Sjoert van Velzen[6], Erica Hammerstein[7,8,9], S. Bradley Cenko[8,10], and Yarone M. Tokayer[11]
[1] Bloomberg Center for Physics and Astronomy, Johns Hopkins University, 3400 North Charles Street, Baltimore, MD 21218, USA
[2] Space Telescope Science Institute, 3700 San Martin Drive, Baltimore, MD 21218, USA
[3] Cahill Center for Astrophysics, California Institute of Technology, MC 249-17, 1200 East California Boulevard, Pasadena, CA 91125, USA
[4] Miller Institute for Basic Research in Science, 468 Donner Lab, Berkeley, CA 94720, USA
[5] Department of Astronomy, University of California, Berkeley, CA 94720, USA
[6] Leiden Observatory, Leiden University, PO Box 9513, 2300 RA Leiden, The Netherlands
[7] Department of Astronomy, University of Maryland, College Park, MD 20742, USA
[8] Astrophysics Science Division, NASA Goddard Space Flight Center, Mail Code 661, Greenbelt, MD 20771, USA
[9] Center for Research and Exploration in Space Science and Technology, NASA/GSFC, Greenbelt, MD 20771, USA
[10] Joint Space-Science Institute, University of Maryland, College Park, MD 20742, USA
[11] Department of Physics, Yale University, PO Box 208120, New Haven, CT 06520, USA
Received 2023 August 23; revised 2024 February 28; accepted 2024 February 29; published 2024 May 2

Abstract

We present a systematic analysis of the X-ray emission of a sample of 17 optically selected, X-ray-detected tidal disruption events (TDEs) discovered between 2014 and 2021. The X-ray light curves show a diverse range of temporal behaviors, with most sources not following the expected power-law decline. The X-ray spectra are mostly extremely soft and consistent with thermal emission from the innermost region of an accretion disk, which cools as the accretion rate decreases. Three sources show formation of a hard X-ray corona at late times. The spectral energy distribution shape, probed by the ratio ($L_{\rm BB}/L_{\rm X}$) between the UV/optical and X-ray, shows a wide range of $L_{\rm BB}/L_{\rm X} \in (0.5, 3000)$ at early times and converges to disklike values of $L_{\rm BB}/L_{\rm X} \in (0.5, 10)$ at late times. We estimate the fraction of optically discovered TDEs with $L_{\rm X} \geqslant 10^{42}$ erg s^{-1} to be at least 40% and show that X-ray loudness is independent of black hole mass. We argue that distinct disk formation timescales are unlikely to be able to explain the diverse range of X-ray evolution. We combine our sample with X-ray-discovered ones to construct an X-ray luminosity function, best fit by a broken power law, with a break at $L_{\rm X} \approx 10^{44}$ erg s^{-1}. We show that there is no dichotomy between optically and X-ray-selected TDEs; instead, there is a continuum of early-time $L_{\rm BB}/L_{\rm X}$, at least as wide as $L_{\rm BB}/L_{\rm X} \in (0.1, 3000)$, with optical/X-ray surveys selecting preferentially, but not exclusively, from the higher/lower end of the distribution. Our findings are consistent with unification models for the overall TDE population.

Unified Astronomy Thesaurus concepts: Tidal disruption (1696); X-ray transient sources (1852); Supermassive black holes (1663); Time domain astronomy (2109); High energy astrophysics (739); Accretion (14)

1. Introduction

The occasional tidal disruption of a star that approaches close enough to a massive black hole (MBH) was predicted by theorists as a signpost for MBHs lurking in the center of galaxies (Hills 1975; Rees 1988; Ulmer 1999). These luminous events, called tidal disruption events (TDEs), are observed throughout the entire electromagnetic spectrum and are now a well-established class of transients (see recent review by Gezari 2021). TDEs are a unique opportunity to probe the existence of quiescent black holes in the low-mass end of the MBH's mass function ($<10^8\ M_\odot$). At higher black hole masses, a TDE is not observable; stars are swallowed whole, since the tidal disruption radius lies inside the event horizon (Hills 1975; van Velzen 2018; Yao et al. 2023).

The first observational evidence for TDEs came from the detection of X-ray flares from the centers of quiescent galaxies during the ROSAT All-Sky Survey (RASS) in 1990–1991 (e.g., Bade et al. 1996; Grupe et al. 1999; Komossa & Greiner 1999; Greiner et al. 2000). The flares exhibited soft spectra with temperatures $T \sim 10^6$ K (for a review of X-ray-selected TDEs, see Saxton et al. 2020). Since 2020, the Spektrum–Roentgen–Gamma (SRG) mission (Sunyaev et al. 2021), with its sensitive eROSITA telescope (Predehl et al. 2021) and 6 month cadence all-sky surveys, has become the most prolific discoverer of TDEs in X-rays, presenting 13 new sources discovered during the first two all-sky scans (Sazonov et al. 2021).

The discovery of TDEs has increased dramatically in the last few years due to the operation of wide-field optical surveys such as iPTF (Blagorodnova et al. 2017, 2019; Hung et al. 2017), Pan-STARRS (Gezari et al. 2012; Chornock et al. 2014; Holoien et al. 2019), ASASSN (Holoien et al. 2014, 2016a, 2016b; Wevers et al. 2019a), and the Zwicky Transient Facility (ZTF; van Velzen et al. 2019, 2021; Hammerstein et al. 2023a; Yao et al. 2023), with ZTF now dominating the number of discoveries with a rate of $\sim$10 yr^{-1} (Hammerstein et al. 2023a; Yao et al. 2023). Although the number of optically selected TDEs dominates over the ones discovered by means of high-energy observations, the nature of what is powering their bright

optical flares is uncertain. Unlike the soft X-ray component detected in some optically selected TDEs—which is similar to the X-ray-selected TDEs and is consistent with thermal emission from the inner radii of an accretion disk—the UV/optical component seems, in most cases, not consistent with the direct emission from the Rayleigh–Jeans tail of the expected disk to form from the circularization of the stellar debris streams around a 10^5–$10^8\,M_\odot$ black hole. This implies the existence of an unknown, larger emitting structure that competing interpretations invoke to be produced either as a result of reprocessing of the extreme-UV (EUV) and X-ray emission (Miller et al. 2015; Dai et al. 2018; Parkinson et al. 2022; Thomsen et al. 2022) or from shocks between intersecting debris streams themselves (Piran et al. 2015; Shiokawa et al. 2015; Jiang et al. 2016; Bonnerot et al. 2017).

Besides the origin of optical emission, a second important aspect of optically selected TDEs is that most of them are X-ray faint. In the unifying reprocessing scenario, the distinct classes of TDEs are given by the viewing angle with respect to the accretion disk and its associated reprocessing layer; the X-ray-bright, "optically faint" TDEs are the ones observed more face-on; the optically bright, X-ray-faint are edge-on; and the ones that show both emission components are seen at intermediate angles (Guillochon et al. 2014; Dai et al. 2018; Parkinson et al. 2022). In this scenario, X-rays from sources at intermediate angles can only break out after the reprocessing gas has expanded enough to become transparent to X-rays (Metzger & Stone 2016; Lu & Kumar 2018; Thomsen et al. 2022). However, in the stream–stream collision scenario, the intrinsically X-ray-faint TDEs have been proposed to be a result of delayed accretion, due to the timescale required for the circularization of the debris into an appreciable accretion disk (Gezari et al. 2017; Liu et al. 2022).

In addition to the study of nascent accretion disks, TDEs can be used to study the formation and evolution of other physical structures related to MBH accretion. Relativistic (e.g., Zauderer et al. 2011; Cenko et al. 2012; Pasham et al. 2015; Brown et al. 2017; Pasham et al. 2023; Yao et al. 2024) and nonrelativistic (e.g., Alexander et al. 2016; Bright et al. 2018; Stein et al. 2021) jets, as well as outflows with velocities varying from 200 to 600 km s^{-1} (Miller et al. 2015; Cenko et al. 2016; Krolik et al. 2016; Blagorodnova et al. 2018; Kosec et al. 2023), up to $0.2c$ (e.g., Lin et al. 2015; Kara et al. 2018) have been detected in several sources.

This paper presents an analysis of the X-ray light curves, X-ray spectral evolution, and broadband UV/optical/X-ray spectral energy distribution (SED) evolution of 16 X-ray-detected, optically discovered TDEs between 2014 and 2021 December and one more simultaneously discovered by SRG/eROSITA (AT 2020ksf) but with extensive UV/optical follow-up. We present new XMM-Newton data for half of our sources and systematically reanalyze all publicly available ZTF, Neil Gehrels Swift Observatory, and XMM-Newton data presented in previous studies on individual sources. In Section 1.1, we present our sample and its selection criteria. In Section 2, we present the data and describe the basic analyses. In Section 3, we present a detailed discussion on the X-ray spectral fitting in TDEs and its general properties. In Section 4, we show our results and their interpretations, which are discussed in terms of the current literature in Section 5; our conclusion are presented in Section 6.

We adopt a standard ΛCDM cosmology with matter density $\Omega_M = 0.3$, dark energy density $\Omega_\Lambda = 0.7$, and Hubble constant $H_0 = 70\,\mathrm{km\,s^{-1}\,Mpc^{-1}}$. Optical and UV magnitudes are reported in the AB system. Uncertainties of X-ray model parameters are reported at the 68% confidence level, and upper limits are reported at 3σ.

1.1. Sample Selection

Aiming to explore the diversity of X-ray evolution in optically selected TDEs, we draw our sample from sources discovered by optical time-domain surveys. We compile sources from ZTF sample papers (van Velzen et al. 2021; Hammerstein et al. 2023b; Yao et al. 2023) as well as studies of individual sources from other surveys (Holoien et al. 2016a, 2016b; Wyrzykowski et al. 2017; Wevers et al. 2019a). We do not consider nuclear transients with preexisting active galactic nuclei (AGN) from TDE candidates; this excludes those with host galaxies with AGN-like broad emission lines or NEOWISE (Mainzer et al. 2014) mid-infrared (MIR) variability before the transient, as well as W1–W2 MIR color exceeding AGN selection criteria (e.g., Stern et al. 2012). We limited the sample based on the epoch of discovery; given that the first optically discovered TDE to be systematically followed up by X-ray telescopes was ASASSN-14li, we delimited the sample with sources discovered after 2014. Our discovery epoch criteria also exclude those sources discovered after 2021 December, allowing us to have more than 1 yr of data for the entire sample. Finally, we require every source to have at least one 3σ Swift X-Ray Telescope (XRT) detection, yielding our final sample of 17 optically selected X-ray-detected TDEs. The complete sample and the basic information on the sources are shown in the upper portion of Table 1, and in Figure 1, we show the distribution of some basic properties of our sample. Besides the observations of the 17 sources that make up our main sample, we also present deep upper limits based on XMM-Newton observations of another nine optically selected TDEs that never show detectable X-ray emission; these sources are shown in the bottom portion of Table 1.

2. Observations, Data Reduction, and Analyses

2.1. Observations and Data Reduction

2.1.1. XMM-Newton

The primary data set underlying this work is based on XMM-Newton observations. These were obtained primarily from a series of announcement-of-opportunity (AO) programs (AO-18 84259, AO-20 88259, PI: Gezari; AO-21 90276, PI: Yao) aimed at the deep X-ray follow-up of ZTF-discovered TDEs. These observations were taken in full-frame mode with the thin filter using the European Photon Imaging Camera (EPIC; Strüder et al. 2001) and are presented here for the first time. We also included publicly available observations from several other AO and Director Discretionary Time proposals. The details of the XMM-Newton observations are shown in Table 2.

The observation data files reduced using the XMM-Newton Standard Analysis Software (SAS; Gabriel et al. 2004). The raw data files were then processed using the `epproc` task. Since the pn instrument generally has better sensitivity than MOS1 and MOS2, we only analyze the pn data. Following the XMM-Newton data analysis guide, to check for background activity and generate "good time intervals," we manually inspected the

Table 1
Sample Information

IAU Name	Discovery Name	Optical/UV Peak (MJD)	Redshift	$N_{H,G}$ (10^{20} cm^{-2})[a]	log ($M_*/M_\odot$)[b]	σ_* (km s^{-1})	log($M_{BH}/M_\odot$)[c]	TDE Classification
AT 2018zr	ZTF 18aabtxvd	58214	0.071	4.17	$10.01^{+0.08}_{-0.14}$	49 ± 5[d]	5.83 ± 0.51	ATel #11444
AT 2018hyz	ASASSN-18zj	58422	0.045	2.59	$9.96^{+0.09}_{-0.16}$	57 ± 1[e]	6.12 ± 0.46	ATel #12198
AT 2019azh	ASASSN-19dj	58558	0.022	4.15	$9.74^{+0.08}_{-0.05}$	77 ± 2[f]	6.68 ± 0.46	ATel #12568
AT 2019dsg	ZTF 19aapreis	58600	0.051	6.46	$10.55^{+0.09}_{-0.12}$	94 ± 1[g]	7.04 ± 0.45	ATel #12752
AT 2019ehz	Gaia 19bpt	58611	0.074	1.42	$9.65^{+0.09}_{-0.12}$	47 ± 11[d]	5.75 ± 0.59	ATel #12789
AT 2019qiz	ZTF 19abzrhgq	58764	0.015	6.35	$10.01^{+0.09}_{-0.12}$	70 ± 2[h]	6.49 ± 0.46	ATel #13131
AT 2019teq	ZTF 19accmaxo	58794	0.087	4.54	$9.95^{+0.07}_{-0.11}$	⋯	6.32 ± 0.49	TNSCR #7482
AT 2019vcb	ZTF 19acspeuw	58838	0.088	1.45	$9.49^{+0.06}_{-0.06}$	⋯	5.59 ± 0.52	TNSCR #7078
AT 2020ddv	ZTF 20aamqmfk	58915	0.16	1.35	$10.30^{+0.13}_{-0.16}$	57 ± 10[d]	6.09 ± 0.55	ATel #13655
AT 2020ksf	Gaia 20cjk	58976	0.092	3.61	$10.12^{+0.13}_{-0.09}$	52 ± 2[i]	5.92 ± 0.48	Gilfanov et al. (2020)
AT 2020ocn	ZTF 18aakelin	58972	0.07	1.28	$10.28^{+0.13}_{-0.70}$	81 ± 8[d]	6.77 ± 0.49	ATel #13859
AT 2021ehb	ZTF 21aanxhjv	59330	0.018	9.88	$10.18^{+0.01}_{-0.02}$	93 ± 5[j]	7.04 ± 0.46	TNSCR #10001
AT 2021yzv	ZTF 21abxngcz	59475	0.286	8.60	$10.65^{+0.04}_{-0.06}$	⋯	7.45 ± 0.47	TNSCR #11890
⋯	ASASSN-14li	56993	0.02	1.95	$9.68^{+0.04}_{-0.09}$	81 ± 2[k]	6.77 ± 0.46	ATEL #6777
⋯	ASASSN-15oi	57259	0.048	4.86	$10.02^{+0.04}_{-0.03}$	⋯	6.42 ± 0.48	ATEL #7936
AT 2018fyk	ASASSN-18ul	58389	0.059	1.16	$10.56^{+0.21}_{-0.12}$	158 ± 1[l]	8.04 ± 0.44	TNSCR #2723
⋯	OGLE 16aaa	57403	0.165	2.72	$10.47^{+0.09}_{-0.11}$	⋯	7.14 ± 0.48	Wyrzykowski et al. (2017)
AT 2018bsi	ZTF 18aahqkbtr	58389	0.051	4.91	$10.62^{+0.05}_{-0.07}$	118 ± 8[d]	7.48 ± 0.46	ATel #12035
AT 2018hco	ATLAS 18way	58479	0.088	4.12	$10.01^{+0.12}_{-0.16}$	⋯	6.40 ± 0.49	ATel #12263
AT 2018iih	ATLAS 18yzs	58558	0.212	3.19	$10.81^{+0.11}_{-0.14}$	⋯	7.70 ± 0.48	van Velzen et al. (2021)
AT 2018lna	ZTF 19aabbnzo	58561	0.091	6.42	$9.56^{+0.08}_{-0.14}$	36 ± 4[d]	5.20 ± 0.53	ATel #12509
AT 2019mha	ZTF 19abhejal	58705	0.148	1.71	$10.01^{+0.14}_{-0.18}$	⋯	6.41 ± 0.49	van Velzen et al. (2021)
AT 2019meg	ZTF 19abhhjcc	58743	0.152	5.08	$9.64^{+0.07}_{-0.08}$	⋯	5.81 ± 0.52	AN-2019-88
AT 2020pj	ZTF 20aabqihu	58866	0.068	2.24	$10.01^{+0.07}_{-0.08}$	⋯	6.43 ± 0.49	TNSCR #7481
AT 2020vwl	ZTF 20achpcvt	59167	0.032	2.23	$9.89^{+0.08}_{-0.08}$	⋯	6.21 ± 0.49	TNSCR #8572
AT 2020wey	ZTF 20acitpfz	59156	0.027	6.19	$9.67^{+0.09}_{-0.12}$	39 ± 3[d]	5.38 ± 0.51	TNSCR #7769

Notes. Top: X-ray-detected TDE (main sample). Bottom: X-ray-nondetected TDEs with new deeper upper limits. Abbreviations: ATel corresponds to the Astronomer's Telegram (https://astronomerstelegram.org), AN corresponds to AstroNotes (https://www.wis-tns.org/astronotes), and TNSCR corresponds to TNS classification reports.
[a] Galactic absorption column density from HI4PI Collaboration et al. (2016).
[b] Host galaxy stellar mass from SED fitting (see Section 2.2.1).
[c] Black hole masses. When a σ_* measurement is available, it is estimated using the Gültekin et al. (2019) σ_*–M_{BH} relation; when σ_* is not available, this is estimated from the M_*–M_{BH} relation presented in Yao et al. (2023).
[d] Hammerstein et al. (2023b).
[e] Short et al. (2020).
[f] Liu et al. (2022).
[g] Cannizzaro et al. (2021).
[h] Nicholl et al. (2020).
[i] T. Wevers et al. (2024, in preparation).
[j] Yao et al. (2022).
[k] Wevers et al. (2019b)
[l] Wevers et al. (2019a).

background light curves in the 10–12 keV band. Using the `evselect` task, we only retained patterns that correspond to single and double events (`PATTERN<=4`). The source spectra were extracted using a source region of $r_{src} = 35''$ around the peak of the emission. The background spectra were extracted from an $r_{bkg} = 108''$ region located in the same CCD. The ancillary response files and response matrix files were created using the `arfgen` and `rmfgen` tasks, respectively. Some of the observations for ASASSN-14li and AT 2020ocn presented pile-up effects. Therefore, we followed the SAS guide by excising the core of the point-spread function (PSF) up to a radius where the pile-up fraction becomes negligible following the `epatplot` command results.

2.1.2. Neil Gehrels Swift Observatory

All the sources were observed by the XRT (Burrows et al. 2005) and the Ultra-Violet/Optical Telescope (UVOT; Roming et al. 2005) on board the Neil Gehrels Swift Observatory (Gehrels et al. 2004). The number of observations varies from a few for the more distant sources to 100 for the most well-sampled sources.

The 0.3–10 keV X-ray count light curves were produced using the UK Swift Data Center online XRT data products tool, which uses the HEASOFT v6.22 software (Arnaud 1996). We used a fixed aperture at the ZTF coordinate of the transient, generating one count rate point per visit (i.e., per ObsID) for most of the

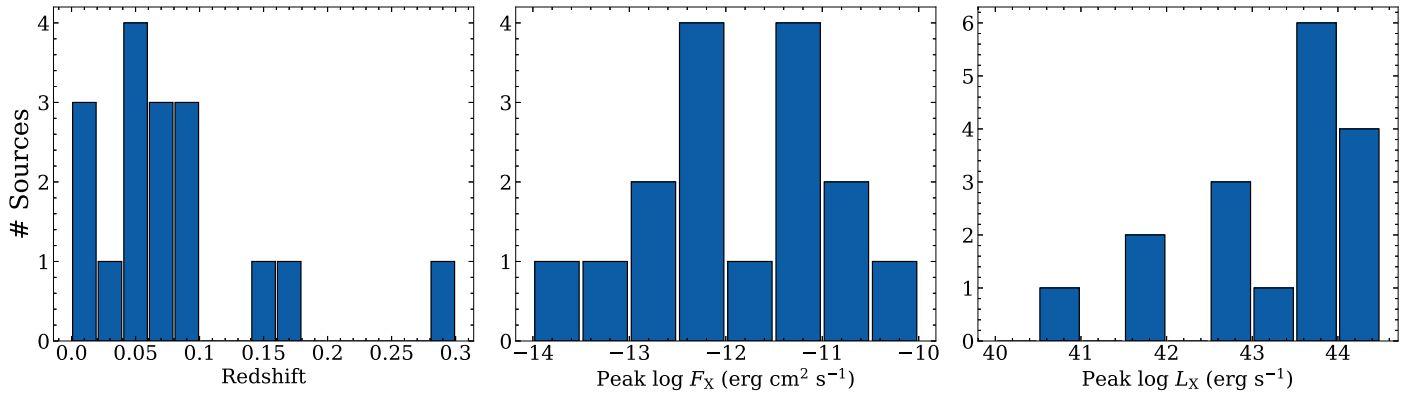

Figure 1. Histogram of the distributions of the properties of our main sample. Redshift (z; left), neutral absorption-corrected peak 0.3–10 keV X-ray flux (F_X; middle), and neutral absorption-corrected peak 0.3–10 keV X-ray luminosity (L_X; right).

sources; for faint sources (AT 2018zr, AT 2018hyz, and AT 2019qiz), in which the count rates of individual visits were close to the XRT detection limit ($\sim 10^{-3}$ counts s^{-1}), we stack a few observations using the "dynamical binning" as described in Evans et al. (2007) in order to obtain a smooth X-ray light curve.

The short XRT exposures do not allow for spectral fitting of individual visits, so we stacked consecutive observations using an automated online tool (Evans et al. 2009). We aimed to have at least 100 counts per stacked spectrum, allowing the bins to be at maximum 100 days long; we also ensured there was no large evolution in the hardness ratio (HR) within each bin. For AT 2018zr, AT 2019vcb, AT 2020ddv, and ASASSN-15oi, there were not enough counts to generate a fitable spectrum, even combining all the XRT observations; therefore, we restrict our XRT analysis of their light curves and only perform spectral analysis in their XMM-Newton data, which will be described in detail in Section 3.

We used the `uvotsource` package to analyze the Swift UVOT photometry, using an aperture of 5″ for all sources except AT 2019azh, AT 2019qiz, and AT 2019dsg, which required a larger aperture to capture the host galaxy light. We subtracted the host galaxy flux estimated from the population synthesis modeling of archival preevent photometry described in Section 2.2.1. We apply Galactic extinction correction on all bands using $E(B-V)$ values at the position of each source from Schlafly & Finkbeiner (2011).

2.1.3. ZTF

We performed PSF photometry on all publicly available ZTF data using the ZTF forced-photometry service (Masci et al. 2019, 2023) in the g and r bands. Similar to UVOT, ZTF photometry was corrected for Galactic extinction.

2.1.4. Additional Data

OGLE 16aaa was discovered by the fourth phase of the Optical Gravitational Lensing Experiment (OGLE-IV; Udalski et al. 2015) survey. We added the I-band (7970 Å) light curve, which is the best-sampled optical light curve of the source; the data were retrieved from the survey website.

The optical peak of AT 2020ksf was missed by ZTF; however, the Asteroid Terrestrial-impact Last Alert System (ATLAS; Tonry et al. 2018) started observing the field containing the source ∼60 days before ZTF, hence allowing us to measure the date of its optical peak; we added available ATLAS data to our light curve of AT 2020ksf. The source was first detected in the X-ray by the SRG/eROSITA; although the spectral data are not yet publicly available, we added the reported detection flux of 1.7×10^{-12} erg cm^{-2} s^{-1} (2.85×10^{-12} erg cm^{-2} s^{-1} unabsorbed) observed on 2020 November 20 (MJD 59162), as well as the previous X-ray upper limit ($\leqslant 2.85 \times 10^{-13}$ erg cm^{-2} s^{-1}) from a visit taken on 2020 May 8 (MJD 58977), which is fortuitously timed at the optical peak of the source, both reported by Gilfanov et al. (2020).

2.2. UV/Optical Data Analyses

2.2.1. Host Galaxy SED Modeling

Before analyzing the transient's UV/optical light curve, the host contamination needs to be subtracted. We followed van Velzen et al.'s (2021) prescription to fit the host galaxy preflare photometry. We compile the host galaxy SED using archival observations in the UV through IR bands. We use the `Prospector` software (Johnson et al. 2021) to run a Markov Chain Monte Carlo (MCMC) sampler (Foreman-Mackey et al. 2013) to obtain the posterior distributions of the flexible stellar population synthesis models (Conroy et al. 2009). We adopted a simple power-law star formation history, with the same ranges and priors as in van Velzen et al. (2021), for the five free parameters: stellar mass, Calzetti et al. (2000) dust model optical depth, stellar population age, metallicity, and e-folding time of the star formation history. The resulting host stellar masses (M_*) are presented in Table 1, and the fitting for all host galaxies of our sample are presented in either van Velzen et al. (2021), Hammerstein et al. (2023a), or Yao et al. (2023); the reader is referred to these papers for the full list of best-fitting parameters. We subtract the host contribution to the transient's UVOT filter's photometry. The UV W1-band (2600 Å, observed frame) host-subtracted light curves are shown in the top panels of Figure 2 for individual sources.

2.2.2. UV/Optical Light Curves

Following the standard approach for optical TDEs (e.g., van Velzen et al. 2021; Hammerstein et al. 2023a), we estimate the integrated UV/optical luminosity (L_{BB}) by fitting the transient UV/optical SED with an evolving Gaussian rise and power-law decay blackbody (BB) function. The model can be

Table 2
Summary of XMM-Newton Observations

Source	ObsID	Obs. Date (MJD)	Phase (Δt)[a] (days)	log F_X^b (erg cm^{-2} s^{-1})	log L_X^b (erg s^{-1})	L_{BB} / L_X	First Presented in
AT 2018zr	0822040301	58220	5	$-13.538^{+0.040}_{-0.045}$	$41.610^{+0.040}_{-0.045}$	$95.46^{+9.26}_{-9.30}$	van Velzen et al. (2019)
	0822040501	58241	25	$-13.831^{+0.052}_{-0.059}$	$41.317^{+0.052}_{-0.059}$	$127.48^{+16.28}_{-16.24}$	
	0822040401	58569	331	$-13.493^{+0.033}_{-0.036}$	$41.656^{+0.033}_{-0.036}$	$12.38^{+0.99}_{-1.00}$	This work
AT 2019azh	0822041101	58579	20	$-12.872^{+0.016}_{-0.017}$	$41.178^{+0.016}_{-0.017}$	$889.10^{+34.07}_{-34.09}$	This work
	0842591001	58760	197	$-10.924^{+0.002}_{-0.002}$	$43.125^{+0.002}_{-0.002}$	$0.58^{+0.01}_{-0.01}$	
	0823810401	58788	225	$-10.881^{+0.001}_{-0.001}$	$43.168^{+0.001}_{-0.001}$	$0.41^{+0.01}_{-0.01}$	
	0842592601	58971	404	$-12.248^{+0.013}_{-0.014}$	$41.801^{+0.013}_{-0.014}$	$2.14^{+0.07}_{-0.07}$	
	0902761101	60049	1458	$-14.114^{+0.116}_{-0.158}$	$39.936^{+0.116}_{-0.158}$	…	
AT 2019dsg	0842590901	58633	31	$-11.483^{+0.004}_{-0.004}$	$43.316^{+0.004}_{-0.004}$	$3.16^{+0.03}_{-0.03}$	Stein et al. (2021)
	0842591901	58779	170	< -13.046	<41.753	>15.99	
AT 2019ehz	0842590801	58633	20	$-13.138^{+0.022}_{-0.023}$	$41.998^{+0.022}_{-0.023}$	$50.89^{+2.63}_{-2.63}$	This work
AT 2019teq	0842591701	58841	43	$-12.549^{+0.011}_{-0.012}$	$42.736^{+0.011}_{-0.012}$	$2.25^{+0.06}_{-0.06}$	This work
	0842592401	58915	111	$-12.173^{+0.005}_{-0.006}$	$43.111^{+0.005}_{-0.006}$	$0.49^{+0.01}_{-0.01}$	
AT 2019vcb	0871190301	58991	140	$-12.967^{+0.020}_{-0.021}$	$42.339^{+0.020}_{-0.021}$	$1.71^{+0.08}_{-0.08}$	Quintin et al. (2023)
	0882591401	59764	851	$-14.136^{+0.106}_{-0.150}$	$41.169^{+0.106}_{-0.150}$	$7.12^{+1.97}_{-2.08}$	This work
AT 2020ddv	0842592501	58967	44	$-12.332^{+0.008}_{-0.008}$	$43.523^{+0.008}_{-0.008}$	$5.05^{+0.09}_{-0.09}$	This work
AT 2020ksf	0882591201	59725	749	$12.280^{+0.009}_{-0.010}$	$43.057^{+0.009}_{-0.010}$	$2.92^{+0.06}_{-0.06}$	This work
AT 2020ocn	0863650101	59048	76	$-12.238^{+0.005}_{-0.006}$	$42.848^{+0.005}_{-0.006}$	$1.42^{+0.02}_{-0.02}$	Pasham et al. (2024)
	0872392901	59349	377	$-11.902^{+0.004}_{-0.004}$	$43.183^{+0.004}_{-0.004}$	$0.06^{+0.01}_{-0.01}$	This work
	0902760701	59712	685	$-13.094^{+0.020}_{-0.021}$	$41.991^{+0.020}_{-0.021}$	$2.73^{+0.13}_{-0.13}$	
AT 2021ehb	0882590101	59430	98	$-10.696^{+0.003}_{-0.004}$	$43.177^{+0.003}_{-0.004}$	$0.49^{+0.01}_{-0.01}$	Yao et al. (2022)
	0882590901	59604	269	$-11.203^{+0.003}_{-0.003}$	$42.670^{+0.003}_{-0.003}$	$0.52^{+0.01}_{-0.01}$	
	0902760101	59825	486	$-11.489^{+0.006}_{-0.006}$	$42.384^{+0.006}_{-0.006}$	$0.67^{+0.01}_{-0.01}$	This work
AT 2021yzv	0882591001	59654	139	$13.844^{+0.054}_{-0.062}$	$42.580^{+0.054}_{-0.062}$	$99.26^{+13.22}_{-13.19}$	This work
	0882591501	59837	281	$-14.222^{+0.301}_{-0.176}$	$42.204^{+0.301}_{-0.176}$	$68.48^{+68.48}_{-22.83}$	
ASASSN-14li	0694651201	56997	3	$10.549^{+0.002}_{-0.002}$	$43.442^{+0.002}_{-0.002}$	$2.33^{+0.01}_{-0.01}$	Miller et al. (2015)
	0694651401	57023	29	$-10.588^{+0.002}_{-0.002}$	$43.403^{+0.002}_{-0.002}$	$1.31^{+0.01}_{-0.01}$	Kara et al. (2018)
	0694651501	57213	215	$-11.135^{+0.004}_{-0.004}$	$42.856^{+0.004}_{-0.004}$	$0.78^{+0.01}_{-0.01}$	
	0770980501	57399	397	$-11.312^{+0.005}_{-0.005}$	$42.679^{+0.005}_{-0.005}$	$0.49^{+0.01}_{-0.01}$	Wen et al. 2020
	0770980701	57726	718	$-11.855^{+0.007}_{-0.008}$	$42.136^{+0.007}_{-0.008}$	$2.04^{+0.04}_{-0.04}$	
	0770980901	58092	1076	$-12.318^{+0.008}_{-0.009}$	$41.673^{+0.008}_{-0.009}$	$5.13^{+0.10}_{-0.10}$	
ASASSN-15oi	0722160501	57324	62	$-12.907^{+0.027}_{-0.029}$	$41.837^{+0.027}_{-0.029}$	$77.94^{+5.07}_{-5.06}$	Gezari et al. (2017)
	0722160701	57482	212	$-12.051^{+0.011}_{-0.011}$	$42.693^{+0.011}_{-0.011}$	$1.22^{+0.03}_{-0.03}$	
AT 2018fyk	0831790201	58461	67	$-12.056^{+0.005}_{-0.005}$	$42.874^{+0.005}_{-0.005}$	$29.62^{+0.31}_{-0.31}$	Wevers et al. (2021)
	0853980201	58783	372	$-11.803^{+0.003}_{-0.003}$	$43.127^{+0.003}_{-0.003}$	$2.97^{+0.02}_{-0.02}$	
OGLE 16aaa	0790181801	57548	124	$-13.563^{+0.056}_{-0.064}$	$42.322^{+0.056}_{-0.064}$	$15.06^{+2.06}_{-2.06}$	Kajava et al. (2020)
	0793183201	57722	273	$-12.543^{+0.012}_{-0.012}$	$43.342^{+0.012}_{-0.012}$	$0.49^{+0.01}_{-0.01}$	
AT 2018bsi	0822040801	58389	164	<-13.453	<41.319	>42	This work
AT 2018hco	0822040901	58479	71	<-13.974	<41.312	>291	This work
AT 2018iih	0822040701	58558	95	<-14.250	<41.867	>254	This work
AT 2018lna	0822041001	58561	48	<-14.057	<41.260	>309	This work
AT 2019mha	0842592201	58705	33	<-14.288	<41.483	>43	This work
AT 2019meg	0842592101	58743	40	<-13.919	<41.878	>82	This work
AT 2020wey	0902760401	59851	676	<-13.0857	<41.1449	…[c]	This work
AT 2020pj	0902760801	59809	882	<-13.5102	<41.5488	…[c]	This work
AT 2020vwl	0902760301	59776	590	<-13.568	<40.8932	…[c]	This work

Notes.
[a] Relative to the rest-frame UV/optical peak.
[b] 0.3–10.0 keV band; upper limits are 3σ.
[c] No simultaneous UV/optical detections available.

written as

$$L_{\rm BB}(t) = L_{\rm BB,peak}\frac{\pi B_\nu(T(t))}{\sigma_{\rm SB}T^4(t))} \times \begin{cases} e^{-(t-t_{\rm peak})^2/2\sigma^2}, & t \leqslant t_{\rm peak} \\ [(t-t_{\rm peak})/t_0]^p, & t > t_{\rm peak} \end{cases}. \quad (1)$$

We consider a nonparametric temperature evolution; we fit the temperature at grid points spaced ± 30 days apart beginning at peak and use a lognormal Gaussian prior at each grid point. We use a Gaussian likelihood function to estimate the parameters of the models above; we use the `emcee` sampler (Foreman-Mackey et al. 2013). Details of the fitting process and resulting UV/optical integrated light curves can be seen in either van Velzen et al. (2021) or Hammerstein et al. (2023a) for all the sources. The time-dependent model assumed in Equation (1) was assumed for the first 350 days of the optical light curve; after that, the light-curve shape usually deviates from the power-law decay (van Velzen et al. 2021; Hammerstein et al. 2023a). For the later epochs, we measured the integrated UV/optical luminosity by fitting again with a blackbody function for the available UV/optical photometry

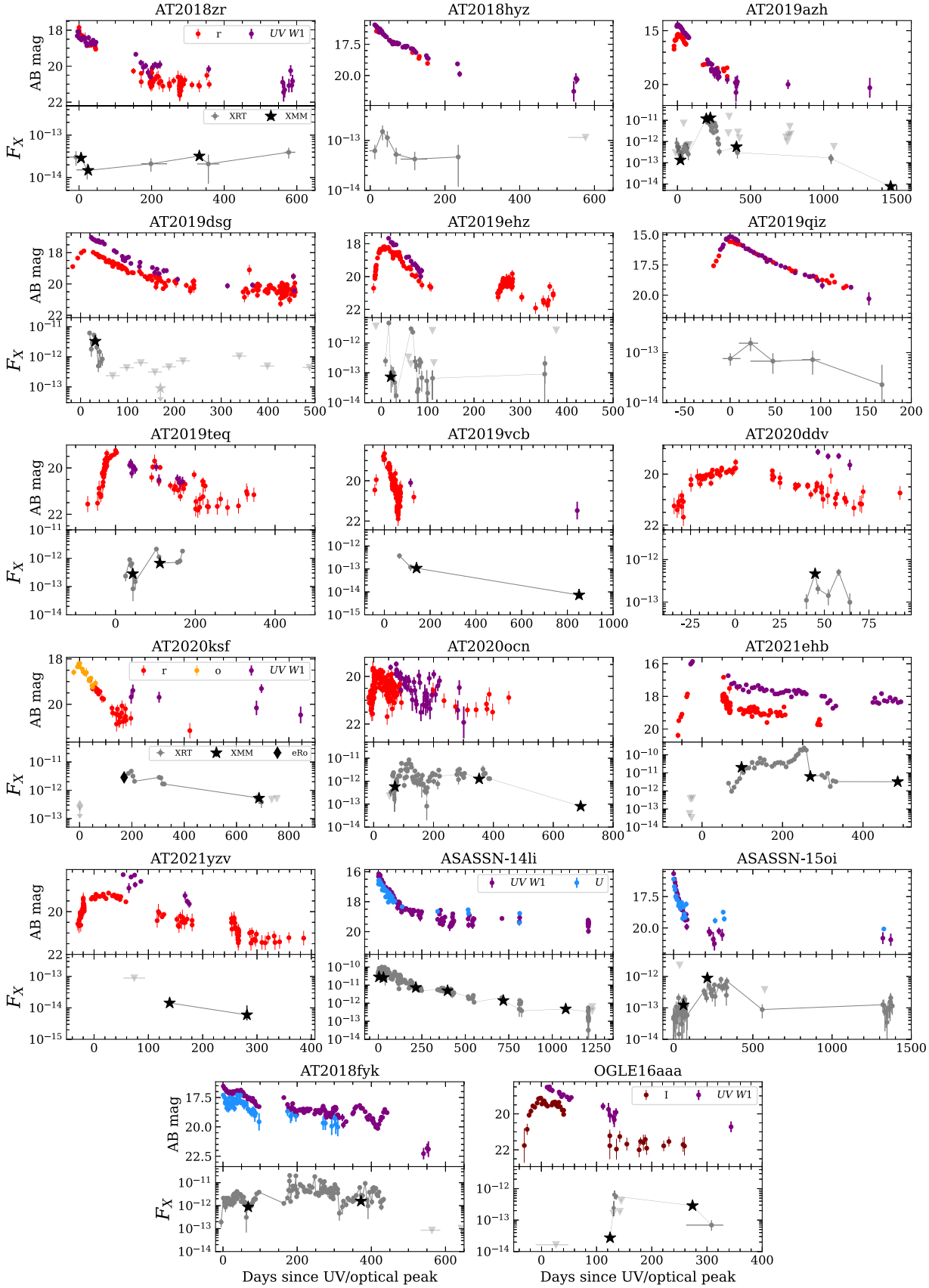

Figure 2. UV/optical (top panels) and X-ray (bottom panels) light curves from our sample of 17 optically selected X-ray-detected TDEs. In the top panels, we show the ZTF *r* band (red points), Swift/UVOT UV W1 band (purple points), ATLAS *o* band (orange points), and OGLE *I* band (maroon points), all in magnitudes in the AB system. In the bottom panels, we show the neutral absorption-corrected 0.3–10 keV X-ray flux (F_X) for Swift/XRT in gray points, XMM-Newton in stars, and SRG/eROSITA in diamonds.

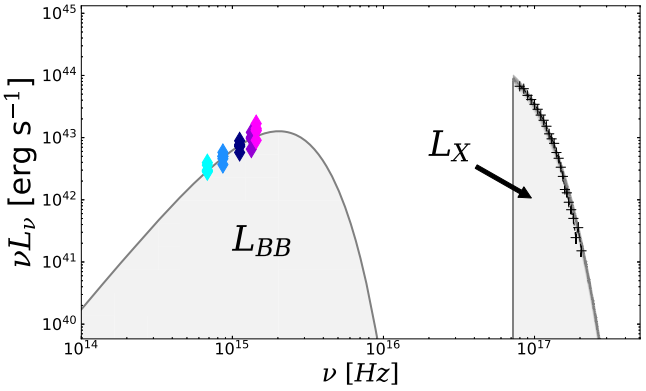

Figure 3. Illustration of how the UV/optical blackbody luminosity (L_{BB}) and the 0.3–10 keV X-ray luminosity (L_X) are measured and what those values represent regarding the full SED of the transient. Colored points indicate observed UV/optical photometry, the best-fitting blackbody function is shown in dark gray, and the area below the curve is the measured L_{BB}. The black plus signs show the observed X-ray spectra and best-fit X-ray model, and the measured L_X is also shown in gray. Both UV/optical and X-ray components are corrected for Galactic extinction/absorption.

data, epoch by epoch, when L_{BB} measurements were necessary (see Section 4). In Figure 3, we illustrate what fitting a blackbody to the UV/optical broadband photometric data means in terms of the full SED of the transient; it also illustrates how misleading it can be to interpret L_{BB} as a "bolometric" luminosity, as is commonly done by some authors; such aspects will be further explored in Section 4.4.

2.3. Black Hole Masses

The black hole masses (M_{BH}) of the TDE hosts were estimated from the host galaxy scaling relations. If a measurement of the velocity dispersion (σ_*) of their nuclear stellar populations was publicly available (e.g., Wevers et al. 2019b; Hammerstein et al. 2023b; Yao et al. 2023), M_{BH} was estimated from the σ_*–M_{BH} relation by Gültekin et al. (2019). Alternatively, if σ_* was not available, M_{BH} was estimated from the host galaxy mass (M_*, as measured from Section 2.2.1) using the relation presented in Yao et al. (2023). The σ_*, M_*, and M_{BH} values are shown in Table 1. Uncertainties in M_{BH} are the result of the addition in quadrature of the statistical uncertainty of σ_*/M_* and the systematic spread of the scaling relations and are usually $\sim$0.5 dex.

3. X-Ray Spectral Fitting

The following procedures were performed using the python version of `xspec` (Arnaud 1996), `pyxspec`.[12] For all spectral models described below, we included the Galactic absorption using the `TBabs` model (Wilms et al. 2000), with the hydrogen-equivalent neutral column density $N_{H,G}$ fixed at the values shown in Table 2 (HI4PI Collaboration et al. 2016). We shifted the TDE emission using the convolution model `zashift`, with the redshift z shown in Table 1. XMM-Newton spectra were grouped to have at least 25 counts bin^{-1} but limiting the oversampling of the instrumental resolution to a factor of 5; we assume a χ^2 statistic. For Swift/XRT data fitting, the stacked spectra were grouped to have at least 1 count bin^{-1}; we assume a C-statistic (Cash 1979). To convert the count rate of each visit to flux, we assume the closest in time best-fit model to the stacked spectra. We check for the convergence of the fitting using the `steppar` command in `xspec`.

[12] https://heasarc.gsfc.nasa.gov/xanadu/xspec/python.

3.1. General Spectral Properties

The most distinct characteristic property of the X-ray spectra of TDEs is softness—a visual inspection of our XMM-Newton observations confirms this trend for our optically detected X-ray-bright TDE sample—which makes TDE X-ray spectra clearly distinguishable from the dominant sources of extragalactic X-ray emission from AGN. While AGN usually emit from the soft X-ray up to the hard X-ray ($E \gg 10$ keV), with a nonthermal (power-law) spectrum, TDEs rarely show emission at energies higher than 2.0 keV.

To demonstrate this, we compare the X-ray spectral properties of our TDE sample with the X-ray properties of the nonblazar type I and type II AGN of the BAT AGN Spectroscopic Survey (BASS; Ricci et al. 2017). Details of how the BASS comparison sample was retrieved are described in Appendix C. In the left panels of Figure 4, we compare the model-independent—but instrument-dependent—HR of the samples, which is defined as HR $=$ (H $-$ S)/(H $+$ S), where S is the 0.3–2.0 keV count rate and H is the 2.0–10.0 keV count. Our entire TDE sample has HR $\leqslant -0.5$, with 85% having HR $\leqslant -0.80$. The type I AGN sample is concentrated in the range $-0.7 \leqslant$ HR $\leqslant 0.0$, while the increased column density (N_H) in obscured type II AGN makes their HR range from 0.0 to 1.0. Such an HR is dependent on the X-ray instrument response; these values are valid for Swift/XRT and/or XMM-Newton, which have similar relative soft-to-hard sensibility.

3.2. Absorbed Power-law Model

In AGN, the main X-ray emission originates from the ubiquitous corona, and it is usually fitted with a phenomenological `powerlaw` model. Fitting a TDE's extremely soft spectra with an absorbed power law (i.e., `TBabs*zashift*(TBabs*powerlaw)` in `xspec`), like in AGN, usually results in a best-fit Γ parameter higher than 5; such high values are nonphysical in the case of inverse upscattering of seed photons by a hot corona (Titarchuk & Lyubarskij 1995) and hence do not represent any meaningful physical measurement.

Nevertheless, fitting with `powerlaw` may be useful to differentiate X-ray TDE spectra from AGN ones. In the right panels of Figure 4, we compare the photon index Γ with those of AGN from the BASS comparison sample. In AGN, both type I and type II, Γ only varies between $\sim$1.0 and 2.5, while in TDEs, these are much steeper, with $\Gamma \in (2, 12)$. The large uncertainties in the spectra with $\Gamma \geqslant 4$ are not due to a low signal-to-noise ratio (S/N); instead, by the inadequacy of the absorbed power law to describe TDE spectra and the large degeneracy between the intrinsic N_H and Γ, when a power-law model is fitted in an underlying thermal/soft spectrum, epochs/spectra with $\Gamma \leqslant 4$ are those in which corona formation is observed (see Section 4.3).

In summary, an absorbed power-law model is an inappropriate model for the emission of nonjetted TDEs, and usually no physical interpretation can be derived from a such fit; however, it still may be a good tool to differentiate (when more

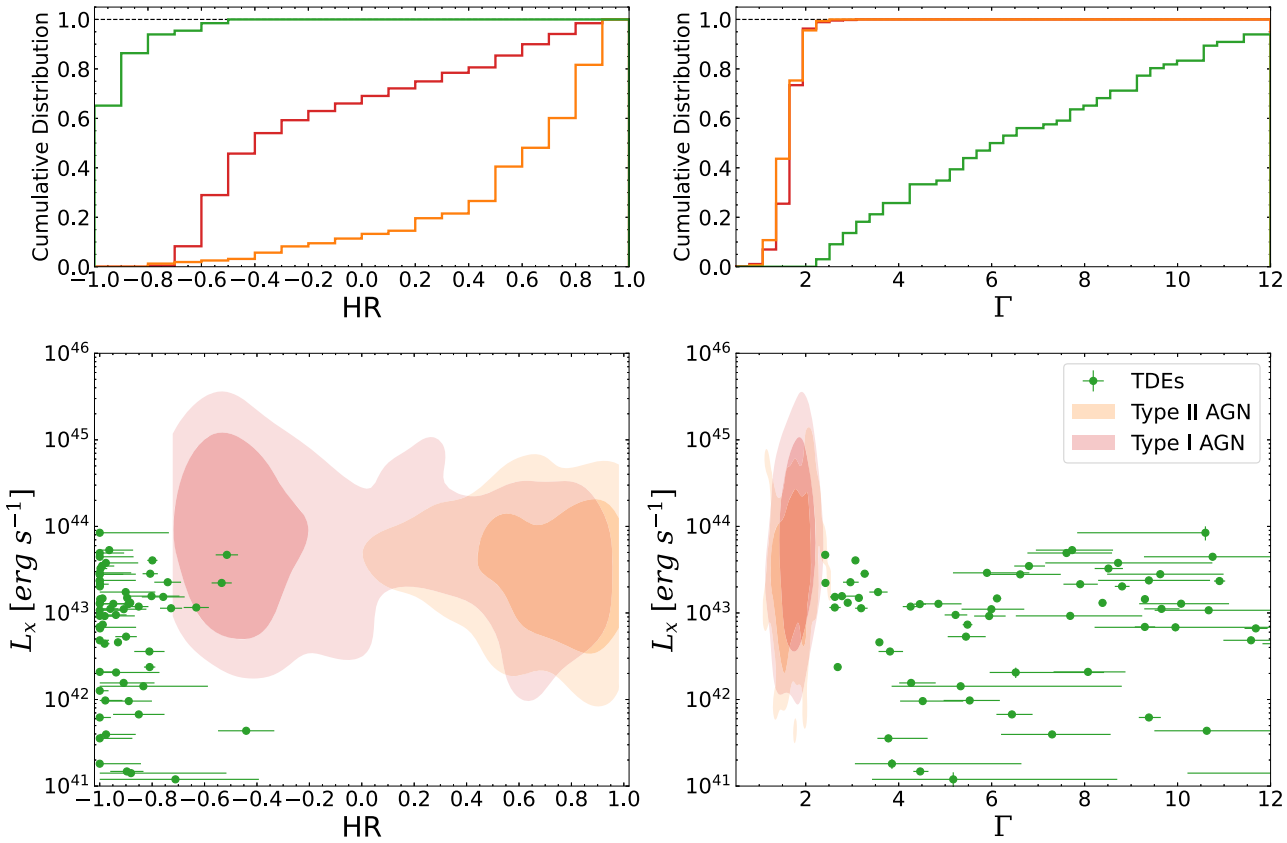

Figure 4. Comparison between X-ray spectral properties of TDEs (green) and AGN (type I in red and type II in gold) from BASS (Ricci et al. 2017). In the left panels, we compare the Swift/XRT or XMM-Newton HR (see text for definition); in the right panels, we compare the Γ power-law index when TDEs are fitted with an absorbed power-law model. The top panels show the cumulative distribution of the parameters, while the bottom panels show the distribution of samples in the L_X vs. HR and L_X vs. Γ parameter space. For AGNs, the contours represent 68% and 90% of the sample distribution; for TDEs, each point is an XMM-Newton or Swift/XRT stacked spectrum.

information is lacking) TDEs from AGN, as clearly demonstrated by Figure 4.

3.3. Single-Temperature Blackbody Model

TDE soft spectra can be fitted with thermal models; in their simplest form, a single-temperature blackbody (`blackbody` or `bbodyrad` in `xspec`) has been used for some of the first X-ray-discovered TDEs (see review by Saxton et al. 2020). We employed such a model in our data (`TBabs*zashift*bbodyrad` in `xspec`), and the model fits spectra with low S/N well. However, the model seems to be insufficient to fit spectra of high count rate observations, in which the model results in systematically worse fits (in terms of reduced χ^2) than multitemperature thermal models, which are usually associated with a standard accretion disk (Shakura & Sunyaev 1973; Mitsuda et al. 1984; Mummery 2021; see below). Furthermore, as shown by Mummery (2021), `bbodyrad` can led to unphysical emitting region sizes.

3.4. Accretion Disk + Comptonization Model

In terms of multitemperature thermal models, the `diskbb` model (Shakura & Sunyaev 1973; Mitsuda et al. 1984) developed for stellar black holes in X-ray binaries (XRBs) is usually employed in TDE spectra. The model, however, assumes quasi-static-state conditions that are not necessarily present in the newly formed accretion disk of TDEs.

Recently, Mummery (2021) developed a model specifically tailored for TDE accretion disks; the author based the modeling on the convenient property of TDE disks being relatively cool, with their spectra peaking below the low bandpass of X-ray telescopes, $kT \leqslant 0.3$ keV. This means that X-ray observations of TDE disks probe the quasi-Wien tail of the disk spectrum; hence, no assumption about the disk temperature profile needs to be made. Instead, the only assumption inherent to the model is that each disk radius emits like a color-corrected blackbody and that there exists some disk radius where the disk temperature peaks. The `xspec` model, called `tdediscspec`, fits the following expression to the observed X-ray spectra (Mummery & Balbus 2021; Mummery 2021):

$$F_\nu(R_p, \tilde{T}_p, \gamma) \simeq \frac{4\pi\xi_1 h\nu^3}{c^2 f_{\rm col}^4}\left(\frac{R_p}{D}\right)^2\left(\frac{k\tilde{T}_p}{h\nu}\right)^\gamma \exp\left(-\frac{h\nu}{k\tilde{T}_p}\right), \quad (2)$$

where $\tilde{T}_p \equiv f_{\rm col} f_\gamma T_p$ and T_p is the parameter of interest, i.e., the hottest temperature in the accretion disk. The factor f_γ is the photon energy-shift factor, defined as the ratio of the observed photon frequency ν to the emitted photon frequency $\nu_{\rm emit}$, $f_\gamma = \nu/\nu_{\rm emit} \approx 1/\sqrt{2}$ (see Mummery & Balbus 2021, and references therein, for details), while $f_{\rm col}$ is the "color-correction" factor, which is included to model disk opacity effects. This correction factor generally takes a value $f_{\rm col} \sim 2.3$ for typical TDE disk temperatures (Done et al. 2012;

Mummery 2021; Mummery et al. 2023), which is the value assumed in the tdediscspec model. The radius R_p is a normalization parameter that corresponds to the radius of the hottest region. The constant γ depends on assumptions about both the inclination angle of the disk and the disk's inner boundary condition and is limited to the range $1/2 \leqslant \gamma \leqslant 3/2$. The properties of γ are discussed in more detail in Mummery (2021, and references therein). In practice, the observed accretion disk spectrum is only weakly dependent on γ, which cannot be strongly constrained from observations (Mummery 2021). In this model, γ is therefore treated as a nuisance parameter, letting it vary between its allowed limits for each source. In fact, the 1σ uncertainties on γ typically fill the entire permitted range, and as such, the γ parameter merely extends the uncertainty range of the parameters T_p and R_p.

We fit our spectra with TBabs×zashift ×tdediscspec. The model shows better fitting quality in terms of both fitting statistics (see Table 3 and Appendix D) and physical interpretation of the derived parameters as compared to the aforementioned models; hence, we adopted it as our main model for the soft component in TDEs.

For several sources/epochs, when fitted only with a soft component, a large residual at higher energies is present. Such a "hard excess" is well described by a power-law function, was already reported for both X-ray (e.g., Saxton et al. 2017) and optically selected TDEs (e.g., Wevers et al. 2021; Yao et al. 2022), and is associated with Compton upscattering of the soft photons by a corona of hot electrons near the accretion disk (Titarchuk & Lyubarskij 1995).

In AGN, this component is the dominant component of their X-ray spectra and is modeled with a phenomenological model ($F(E) \propto E^{-\Gamma}$, powerlaw in xspec). However, for soft and intermediate-state XRBs, which, in contrast to AGN and similar to TDEs, have both their main continuum and power law in the X-ray band, a more physically motivated and self-consistent model was developed by Steiner et al. (2009) to describe the Comptonization process, called simPL in xspec. The model has two free parameters, f_{sc}[13] and Γ_{sc}[14]; the first is the fraction of photons from the soft component that are upscattered to create the power law, and the second is the photon index of the resulting power law. A more detailed discussion of using simPL on X-ray TDE spectra is presented in Appendix A.

We employ the models described above, either tdediscspec or simPL⊗tdediscspec, depending on the need for the "hard tail," based on a simple χ^2/dof analysis. Therefore, our X-ray modeling has either two free parameters (T_p and R_p), if fitted only with tdediscspec, or four free parameters (T_p, R_p, f_{sc}, and Γ_{sc}), if fitted with simPL⊗tdediscspec. We also check whether an additional intrinsic neutral absorption was necessary by adding a zTBabs component to the model. Only for ASASSN-14li and AT 2019dsg did N_H of, respectively, $\sim 5 \times 10^{20}$ and $\sim 3 \times 10^{20}$ cm^{-2} significantly improve the residuals at the softest energies and were added to the final model. For all other sources, the intrinsic absorption component was negligible to the fit quality, which constrained their intrinsic N_H to be $\ll 10^{20}$ cm^{-2}.

The stacked Swift/XRT spectrum of AT 2019qiz and the second XMM-Newton epoch of AT 2019teq show a divergent degeneracy between some of the model parameters and hence no uncertainties on the parameters could be determined; therefore, no interpretation of the derived best-fitting parameters will be done, although we use the best-fit parameters to scale the count rates to flux/luminosity. The measured temperature of the second epoch of AT 2019teq is hotter than the T_p maximum limit on the quasi-Wien approximation of tdediscspec; similarly, no physical interpretation is attributed from the derived physical parameter of this epoch.

In Figure 5, we show the best-fit value and its evolution for all four parameters in our modeling. A representative XMM-Newton observation and modeled spectra, as well as residuals for each source, are shown in Figure 6. In Table 4, we summarize the spectral fitting procedures and models described in this section.

Our final continuum models fit the continuum of most observations (χ^2/dof ~ 1.0) very well. However, some sources present features that resemble absorption lines, usually associated with O VII (∼0.54 keV) and/or O VIII (∼0.65 keV); these can be highly blueshifted (up to $0.2c$) and interpreted as ultrafast outflows (e.g., Kara et al. 2018). We will explore these absorption lines' detection, physical interpretation, and modeling in separate publications for those sources in which the statistical significance of the absorption detection can be assured.

4. Results

In Figure 5, we show the best-fitting parameters from the X-ray spectral fitting, first for the main parameters of tdediscspec, peak temperature (T_p), and apparent radius in which T_p occurs (R_p), and then for the power-law component (simPL), the fraction of the Comptonized photons (f_{sc}), and the photon index of the power law (Γ_{sc}); the latter is only shown for three sources (AT 2018fyk, AT 2020ocn, and AT 2021ehb) in which a strong enough power law is detected at some epoch (i.e., $f_{sc} \geqslant 0.1$), given the high uncertainty in Γ_{sc} when the component is only marginally detected. We also do not show the measurements of T_p and R_p for the epochs in which $f_{sc} \geqslant 0.2$ given that the power-law emission completely dominates the spectra; hence, no trustworthy information on the underlying thermal emission can be recovered, as discussed in Appendix A.

In Figure 7, we show in the left panels the neutral absorption-corrected 0.3–10 keV luminosity (L_X) and in the right panels the ratio (L_{BB}/L_X) between the UV/optical integrated luminosity (L_{BB}; Equation (1)) and L_X for the light curves of all the sources, as classified below.

4.1. Diversity of X-Ray Light Curves

A surprising characteristic of optically discovered X-ray-bright TDEs—first observed in ASASSN-15oi by Gezari et al. (2017)—is that their X-ray light curve does not necessarily follow the theoretically expected fallback rate ($\propto t^{-5/3}$; Rees 1988), not even a more general power-law decay ($\propto t^{-\alpha}$), which is now established as the general evolution of their optical component (Hammerstein et al. 2023a). Instead, a wide diversity of time evolution and luminosity ranges is

[13] This should not be confused with the fractional flux of the power law with respect to the total flux; at $f_{sc} \sim 0.3$, the total flux is already dominated by the power-law component as shown in Appendix A.

[14] We will use Γ_{sc} for the power-law photon index when the TDE X-ray spectra are fitted with simPL⊗tdediscspec and Γ when the spectra are fitted with the powerlaw model.

Table 3
Best-fit Parameters for Final X-Ray Models: `tdediscspec` or `simPL` ⊗`tdediscspec`

Source	MJD	Instrument	T_p (K)	R_p (cm)	f_{sc}	Γ_{sc}	Statistics[a]/dof
AT 2018zr	58220	XMM-Newton	$1.1^{+0.1}_{-0.1} \times 10^6$	$2.5^{+1.1}_{-0.7} \times 10^{10}$	⋯	⋯	6.3/8
	58241	XMM-Newton	$1.0^{+0.2}_{-0.1} \times 10^6$	$2.0^{+1.0}_{-0.6} \times 10^{10}$	⋯	⋯	6.0/6
	58569	XMM-Newton	$5.2^{+0.6}_{-0.4} \times 10^5$	$2.0^{+1.0}_{-0.6} \times 10^{11}$	⋯	⋯	11.3/7
AT 2018hyz	58463^{+30}_{-28}	Swift/XRT	$1.2^{+0.3}_{-0.2} \times 10^6$	$1.1^{+0.9}_{-0.5} \times 10^{10}$	⋯	⋯	13.0/22
AT 2019azh	58579	XMM-Newton	$5.7^{+1.4}_{-0.7} \times 10^5$	$8.9^{+4.2}_{-1.9} \times 10^{10}$	$0.03^{+0.06}_{-0.02}$	$2.2^{+1.2}_{-0.7}$	10.3/16
	58760	XMM-Newton	$4.1^{+0.1}_{-0.3} \times 10^5$	$2.4^{+0.3}_{-0.3} \times 10^{12}$	$0.01^{+0.02}_{-0.01}$	$1.3^{+2.3}_{-1.3}$	30.2/18
	58788	XMM-Newton	$3.5^{+0.1}_{-0.1} \times 10^5$	$4.0^{+0.2}_{-0.1} \times 10^{12}$	$0.01^{+0.01}_{-0.01}$	$4.3^{+0.5}_{-0.2}$	34.4/21
	58971	XMM-Newton	$2.8^{+0.1}_{-0.1} \times 10^5$	$6.2^{+6.0}_{-1.6} \times 10^{12}$	⋯	⋯	16.1/7
AT 2019dsg	58625^{+4}_{-5}	Swift/XRT	$6.7^{+1.4}_{-1.0} \times 10^5$	$2.3^{+3.7}_{-1.3} \times 10^{12}$	⋯	⋯	26.0/41
	58633	XMM-Newton	$5.7^{+0.1}_{-0.6} \times 10^5$	$2.6^{+0.2}_{-0.9} \times 10^{12}$	⋯	⋯	33.3/22
	58641^{+7}_{-7}	Swift/XRT	$5.1^{+0.9}_{-0.7} \times 10^5$	$2.8^{+5.1}_{-1.5} \times 10^{12}$	⋯	⋯	36.4/34
AT 2019ehz	58628^{+1}_{-1}	Swift/XRT	$1.1^{+0.1}_{-0.1} \times 10^6$	$2.5^{+0.4}_{-0.3} \times 10^{11}$	⋯	⋯	84.8/78
	58633	XMM-Newton	$8.2^{+0.6}_{-0.5} \times 10^5$	$8.3^{+1.9}_{-1.4} \times 10^{10}$	⋯	⋯	6.5/9
	58682^{+2}_{-2}	Swift/XRT	$1.1^{+0.1}_{-0.1} \times 10^6$	$1.9^{+0.4}_{-0.3} \times 10^{11}$	⋯	⋯	52.4/58
AT 2019teq	58841	XMM-Newton	$1.9^{+0.1}_{-0.1} \times 10^6$	$2.5^{+0.6}_{-0.1} \times 10^{10}$	⋯	⋯	34.2/41
	58915	XMM-Newton	⋯	⋯	⋯	⋯	82.5/48
AT 2019vcb	58991	XMM-Newton	$5.4^{+0.4}_{-0.3} \times 10^5$	$3.9^{+2.4}_{-1.2} \times 10^{11}$	⋯	⋯	25.1/18
	59764	XMM-Newton	$4.0^{+1.0}_{-0.5} \times 10^5$	$2.9^{+9.5}_{-0.5} \times 10^{11}$	⋯	⋯	9.1/8
AT 2020ddv	58967	XMM-Newton	$7.0^{+0.2}_{-0.1} \times 10^5$	$8.4^{+0.7}_{-0.5} \times 10^{11}$	⋯	⋯	29.8/16
AT 2020ksf	59185^{+5}_{-5}	Swift/XRT	$8.0^{+0.4}_{-0.4} \times 10^5$	$7.0^{+1.2}_{-0.9} \times 10^{11}$	⋯	⋯	48.9/57
	59202^{+3}_{-3}	Swift/XRT	$6.5^{+0.5}_{-0.4} \times 10^5$	$1.1^{+0.3}_{-0.2} \times 10^{12}$	⋯	⋯	38.8/35
	59311^{+3}_{-3}	Swift/XRT	$6.8^{+0.5}_{-0.4} \times 10^5$	$1.0^{+0.3}_{-0.2} \times 10^{12}$	⋯	⋯	39.6/42
	59725	XMM-Newton	$4.3^{+0.2}_{-0.1} \times 10^5$	$2.1^{+0.3}_{-0.1} \times 10^{12}$	⋯	⋯	21.4/13
AT 2020ocn	59041^{+1}_{-1}	Swift/XRT	$8.0^{+0.7}_{-0.6} \times 10^5$	$4.5^{+1.4}_{-1.0} \times 10^{11}$	⋯	⋯	29.7/42
	59048	XMM-Newton	$4.9^{+0.1}_{-0.4} \times 10^5$	$2.3^{+0.1}_{-0.4} \times 10^{12}$	⋯	⋯	35.2/15
	59051^{+2}_{-3}	Swift/XRT	$5.4^{+0.4}_{-0.4} \times 10^5$	$8.2^{+2.8}_{-1.9} \times 10^{11}$	⋯	⋯	27.8/34
	59067^{+4}_{-6}	Swift/XRT	$9.1^{+0.5}_{-0.4} \times 10^5$	$3.2^{+0.5}_{-0.4} \times 10^{11}$	⋯	⋯	62.0/59
	59094^{+12}_{-9}	Swift/XRT	$8.9^{+0.2}_{-0.2} \times 10^5$	$3.8^{+0.3}_{-0.3} \times 10^{11}$	⋯	⋯	89.4/84
	59131^{+18}_{-18}	Swift/XRT	$5.1^{+0.3}_{-0.3} \times 10^5$	$1.1^{+0.2}_{-0.2} \times 10^{12}$	⋯	⋯	30.7/36
	59189^{+18}_{-18}	Swift/XRT	$7.9^{+0.5}_{-0.4} \times 10^5$	$3.1^{+0.6}_{-0.5} \times 10^{11}$	⋯	⋯	39.4/51
	59278^{+9}_{-8}	Swift/XRT	7.9×10^5 (fixed)	$2.7^{+0.2}_{-0.2} \times 10^{11}$	$0.31^{+0.69}_{-0.12}$	$3.0^{+0.4}_{-0.4}$	70.4/90
	59349	XMM-Newton	7.9×10^5 (fixed)	$1.5^{+0.8}_{-0.2} \times 10^{11}$	$0.44^{+0.18}_{-0.24}$	$2.9^{+0.1}_{-0.2}$	56.4/56
	59373^{+12}_{-11}	Swift/XRT	7.9×10^5 (fixed)	$2.0^{+0.2}_{-0.2} \times 10^{11}$	$0.48^{+0.25}_{-0.15}$	$2.6^{+0.2}_{-0.2}$	117.4/126
	59712	XMM-Newton	7.9×10^5 (fixed)	$2.9^{+3.3}_{-0.2} \times 10^{11}$	$0.12^{+0.07}_{-0.06}$	$3.1^{+0.8}_{-0.5}$	12.2/16
AT 2021ehb	59407^{+10}_{-10}	Swift/XRT	$1.3^{+0.2}_{-0.1} \times 10^6$	$2.5^{+0.6}_{-0.3} \times 10^{10}$	$0.04^{+0.04}_{-0.01}$	$1.4^{+1.3}_{-0.4}$	78.8/98
	59430	XMM-Newton	$6.0^{+0.2}_{-0.2} \times 10^5$	$1.4^{+0.2}_{-0.1} \times 10^{12}$	$0.06^{+0.02}_{-0.01}$	$4.4^{+0.2}_{-0.2}$	48.7/45
	59441^{+15}_{-16}	Swift/XRT	$6.4^{+1.1}_{-0.6} \times 10^5$	$3.8^{+1.8}_{-1.3} \times 10^{11}$	$0.21^{+0.10}_{-0.12}$	$4.1^{+0.3}_{-0.5}$	153.2/156
	59475^{+12}_{-12}	Swift/XRT	$9.3^{+0.5}_{-0.5} \times 10^5$	$1.5^{+0.2}_{-0.2} \times 10^{11}$	$0.13^{+0.03}_{-0.02}$	$2.7^{+0.2}_{-0.2}$	262.8/250
	59509^{+12}_{-16}	Swift/XRT	$1.2^{+0.1}_{-0.1} \times 10^6$	$7.6^{+1.4}_{-1.0} \times 10^{10}$	$0.20^{+0.04}_{-0.03}$	$2.2^{+0.1}_{-0.1}$	285.4/306
	59539^{+10}_{-10}	Swift/XRT	$1.5^{+0.1}_{-0.1} \times 10^6$	$4.0^{+0.8}_{-0.6} \times 10^{10}$	$0.27^{+0.04}_{-0.04}$	$1.9^{+0.1}_{-0.2}$	285.4/359
	59565^{+8}_{-9}	Swift/XRT	$1.0^{+0.1}_{-0.1} \times 10^6$	$1.3^{+0.7}_{-0.3} \times 10^{11}$	$0.59^{+0.04}_{-0.05}$	$2.0^{+0.1}_{-0.1}$	401.2/467
	59585^{+7}_{-7}	Swift/XRT	$1.3^{+0.2}_{-0.2} \times 10^6$	$9.7^{+4.1}_{-2.5} \times 10^{10}$	$0.59^{+0.07}_{-0.06}$	$1.9^{+0.1}_{-0.1}$	455.9/476
	59604	XMM-Newton	$1.2^{+0.1}_{-0.1} \times 10^6$	$8.6^{+0.7}_{-0.6} \times 10^{10}$	$0.13^{+0.02}_{-0.02}$	$2.8^{+0.1}_{-0.1}$	77.6/79
	59640^{+7}_{-7}	Swift/XRT	$1.1^{+0.1}_{-0.1} \times 10^6$	$5.6^{+1.5}_{-0.9} \times 10^{10}$	$0.20^{+0.05}_{-0.04}$	$2.3^{+0.2}_{-0.2}$	183.5/214
	59661^{+7}_{-7}	Swift/XRT	$3.9^{+1.3}_{-1.2} \times 10^5$	$8.3^{+22.9}_{-5.1} \times 10^{11}$	$0.31^{+0.15}_{-0.09}$	$3.5^{+0.3}_{-0.3}$	66.5/85
	59825	XMM-Newton	$1.6^{+0.2}_{-0.1} \times 10^6$	$2.8^{+0.6}_{-0.5} \times 10^{10}$	$0.22^{+0.04}_{-0.04}$	$2.2^{+0.1}_{-0.1}$	77.2/71
AT 2021yzv	59654	XMM-Newton	$1.0^{+0.6}_{-0.3} \times 10^6$	$1.5^{+13.2}_{-0.9} \times 10^{11}$	⋯	⋯	2.9/3
ASASSN-14li	56997	XMM-Newton	$4.1^{+0.1}_{-0.1} \times 10^5$	$3.7^{+0.1}_{-0.1} \times 10^{12}$	⋯	⋯	66.3/31
	57023	XMM-Newton	$4.0^{+0.1}_{-0.1} \times 10^5$	$3.8^{+0.1}_{-0.1} \times 10^{12}$	⋯	⋯	98.9/25
	57213	XMM-Newton	$3.3^{+0.1}_{-0.1} \times 10^5$	$4.2^{+0.1}_{-0.1} \times 10^{12}$	⋯	⋯	21.6/19
	57399	XMM-Newton	$3.0^{+0.1}_{-0.1} \times 10^5$	$4.9^{+0.2}_{-0.2} \times 10^{12}$	⋯	⋯	26.5/18
	57726	XMM-Newton	$2.7^{+0.1}_{-0.1} \times 10^5$	$4.8^{+0.3}_{-0.3} \times 10^{12}$	⋯	⋯	22.7/12
	58092	XMM-Newton	$2.3^{+0.1}_{-0.1} \times 10^5$	$6.0^{+0.6}_{-0.5} \times 10^{12}$	⋯	⋯	18.3/13
ASASSN-15oi	57324	XMM-Newton	$5.2^{+0.1}_{-0.5} \times 10^5$	$5.4^{+0.4}_{-1.6} \times 10^{11}$	⋯	⋯	12.7/7
	57482	XMM-Newton	$3.3^{+0.3}_{-0.1} \times 10^5$	$3.3^{+1.8}_{-0.1} \times 10^{12}$	⋯	⋯	15.8/10
AT 2018fyk	58404^{+13}_{-21}	Swift/XRT	$1.3^{+0.1}_{-0.1} \times 10^6$	$1.1^{+0.2}_{-0.1} \times 10^{11}$	$0.01^{+0.04}_{-0.01}$	$1.9^{+1.5}_{-0.9}$	101.5/108
	58436^{+23}_{-16}	Swift/XRT	$1.2^{+0.1}_{-0.1} \times 10^6$	$1.4^{+0.4}_{-0.2} \times 10^{11}$	$0.05^{+0.06}_{-0.03}$	$2.4^{+0.6}_{-0.6}$	128.1/117
	58461	XMM-Newton	$1.2^{+0.1}_{-0.1} \times 10^6$	$1.5^{+0.1}_{-0.1} \times 10^{11}$	⋯	⋯	32.5/31

Table 3
(Continued)

Source	MJD	Instrument	T_p (K)	R_p (cm)	f_{sc}	Γ_{sc}	Statistics[a]/dof
	58476^{+15}_{-12}	Swift/XRT	$1.3^{+0.1}_{-0.1} \times 10^6$	$1.1^{+0.3}_{-0.2} \times 10^{11}$	$0.01^{+0.02}_{-0.01}$	$1.4^{+0.7}_{-0.5}$	112.9/103
	58598^{+34}_{-35}	Swift/XRT	$1.7^{+0.1}_{-0.1} \times 10^6$	$9.1^{+0.9}_{-0.7} \times 10^{10}$	$0.19^{+0.03}_{-0.02}$	$2.1^{+0.1}_{-0.1}$	428.0/470
	58681^{+30}_{-45}	Swift/XRT	$1.4^{+0.1}_{-0.1} \times 10^6$	$1.2^{+0.3}_{-0.2} \times 10^{11}$	$0.27^{+0.05}_{-0.04}$	$2.3^{+0.1}_{-0.1}$	372.8/354
	58745^{+34}_{-28}	Swift/XRT	$1.8^{+0.3}_{-0.3} \times 10^6$	$4.7^{+2.2}_{-1.1} \times 10^{10}$	$0.13^{+0.09}_{-0.05}$	$1.8^{+0.3}_{-0.3}$	165.6/194
	58783	XMM-Newton	$1.3^{+0.1}_{-0.1} \times 10^6$	$1.1^{+0.1}_{-0.1} \times 10^{11}$	$0.16^{+0.01}_{-0.01}$	$2.2^{+0.1}_{-0.1}$	160.4/136
	58822^{+35}_{-38}	Swift/XRT	$2.1^{+0.2}_{-0.2} \times 10^6$	$4.0^{+1.0}_{-0.6} \times 10^{10}$	$0.14^{+0.06}_{-0.04}$	$1.7^{+0.2}_{-0.2}$	221.4/282
OGLE 16aaa	57548	XMM-Newton	$5.6^{+0.9}_{-0.8} \times 10^5$	$4.1^{+4.6}_{-1.6} \times 10^{11}$	⋯	⋯	11.1/16
	57558^{+1}_{-1}	Swift/XRT	$5.6^{+0.9}_{-0.7} \times 10^5$	$2.5^{+2.1}_{-1.0} \times 10^{12}$	⋯	⋯	9.2/15
	57722	XMM-Newton	$5.5^{+0.2}_{-0.2} \times 10^5$	$1.4^{+0.2}_{-0.1} \times 10^{12}$	⋯	⋯	12.0/15

Note.
[a] χ^2 statistics for XMM-Newton spectra and "C-statistics" (Cash 1979) for Swift/XRT spectra.

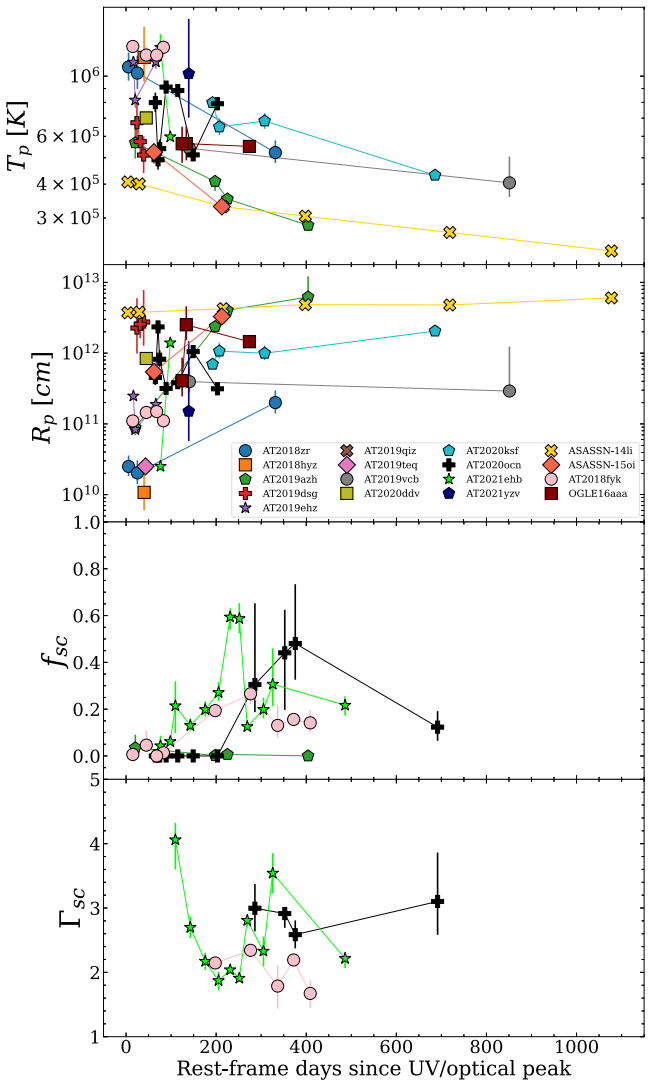

Figure 5. Best-fitting parameters from X-ray spectral modeling as a function of time from the UV/optical peak. From top to bottom: peak temperature (T_p) and radius (R_p) from `tdediscspec`; fraction of Comptonized photons (f_{sc}) and power-law photon index (Γ_{sc}) of `simPL`.

observed, in extreme contrast with some predictions, for example, those by Lodato & Rossi (2011). This diversity also means that the time evolution of the ratio between the UV/optical and X-ray components also evolves in distinct ways in different sources. To search for a general picture of such diversity, we classified the sources in groups with similar evolution in terms of L_X and L_{BB}/L_X; in Figure 7, we show the following classes from top to bottom.

Power-law decaying—ASASSN-14li, AT 2019dsg, and AT 2019cvb are the only three sources to show prompt bright ($L_X \geqslant 10^{43}$ erg s^{-1}) X-ray emission during the optical peak. The three sources show a power-law-like decay X-ray light curve, although the decay rate of the X-ray light curve in AT 2019dsg is much higher than that in ASASSSN-14li and AT 2019cvb. Given the X-ray behavior, their L_{BB}/L_X do not show much variability, staying in the $0.5 \leqslant L_{BB}/L_X \leqslant 10$ range during the entire evolution of the sources.

Late-time brightening—Most sources in our sample show $L_{BB}/L_X \gg 100$ near the optical peak, usually resulting from the faint X-ray emission ($L_X \leqslant 10^{42}$ erg s^{-1}) at early times. However, between 100 and 200 days after the optical peak, they show a significant brightening (more than an order of magnitude, $L_X \geqslant 10^{43}$ erg s^{-1}) in the X-ray, simultaneously with the UV/optical dimming and plateau; consequently, L_{BB}/L_X tends to approach $\sim$1.

X-ray faint—AT 2018zr, AT 2018hyz, and AT 2019qiz also show $L_{BB}/L_X \gg 100$ near the optical peak, again resulting from the faint X-ray emission ($L_X \leqslant 10^{42}$ erg s^{-1}) at early times. However, the three sources never show a bright X-ray phase, although similar to previous classes, their L_{BB}/L_X values also decrease with time.

Flaring—AT 2019ehz shows a unique behavior: the X-ray light curve shows flares of almost 2 orders of magnitude, from $L_X \sim$ few $\times 10^{41}$ erg s^{-1} up to $L_X \sim$ few $\times 10^{43}$ erg s^{-1} on a short timescale of tens of days, while L_{BB} shows a standard smooth evolution.

We could fit 13 of our 17 sources into these four classes; however, for the remaining sources, we do not have enough time coverage to assign them to one of these classes of X-ray evolution due to a lack of either sampling (AT 2021yzv), long-term follow-up (AT 2019vcb and AT 2020ddv), or observations within the first 50 days from the optical peak (AT 20220ocn). The latter is fundamental to access whether the prompt bright X-ray emission is present or not.

4.2. Temperature and Radius Evolution

In this section, we explore the evolution of the temperature (T_p) and radius (R_p) derived from the X-ray continuum fitting

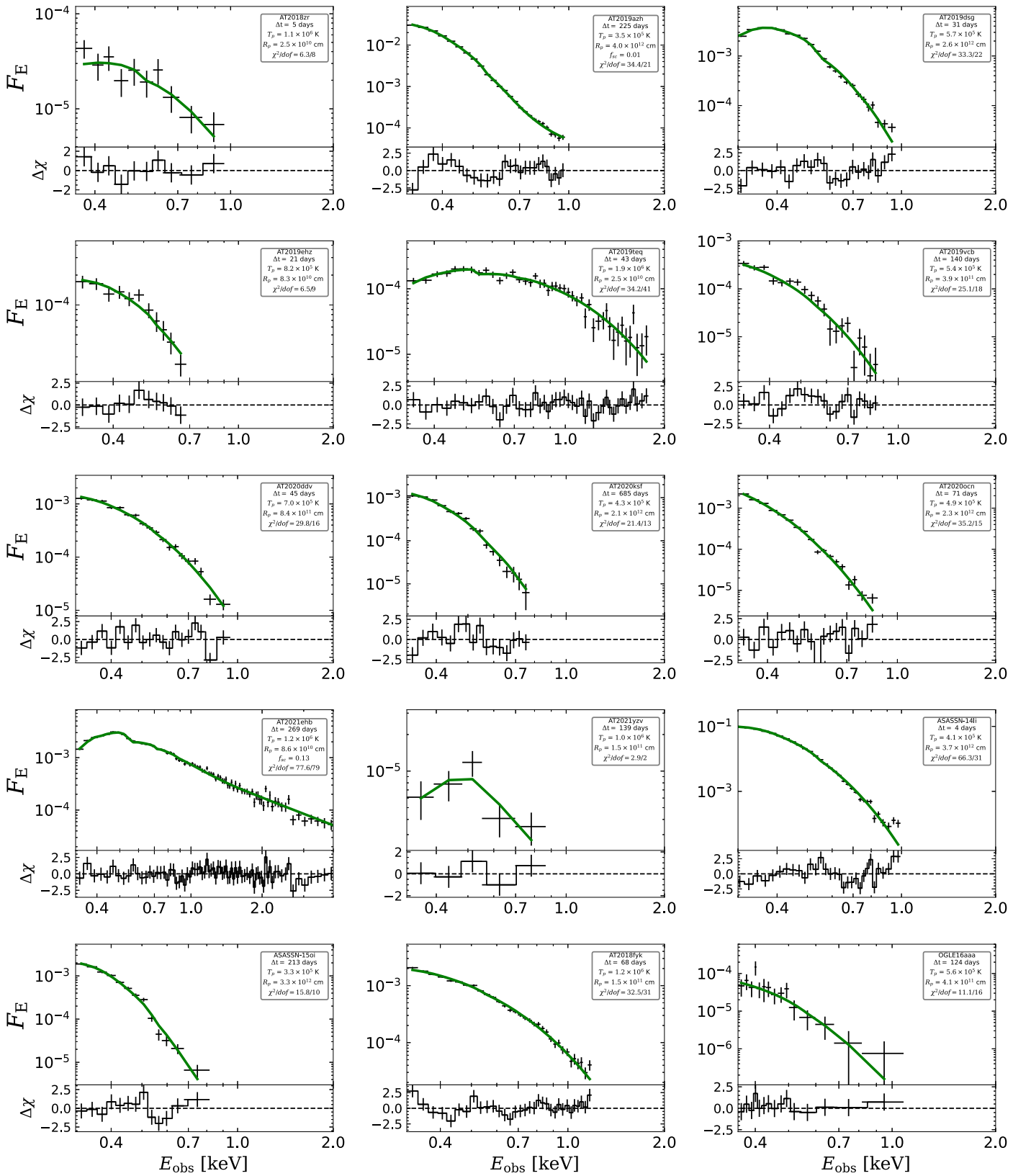

Figure 6. Representative unfolded spectra, best-fit model, and residuals for all the sources with available XMM-Newton data in our sample. Top panels show the unfolded spectra in black and the best-fitting model in green (either `tdediscspec` or `simPL⊗tdediscspec`) in units of keV cm^{-2} s^{-1} keV^{-1}. Bottom panels show the residuals in $\Delta\chi$.

(`tdediscspec`); we focus our analysis on the sources with higher temporal coverage in which some assessments of the long-term evolution of the derived parameters can be made. Due to the degeneracy between f_{sc} and T_p at high values of f_{sc}, and because the underlying thermal cannot be uniquely recovered (see Appendix A), we exclude the sources with

Table 4
Summary of X-Ray Spectral Modeling Described in Section 3

Model	XSPEC[a]	Free Parameters	Notes
Absorbed power law	TBabs × powerlaw	N_H, Γ, norm	• Inappropriate model for X-ray emission of nonjetted TDEs • Overestimates intrinsic N_H • It can be used to differentiate the emission of AGN and TDEs (see Figure 4)
Single-temperature BB	bbodyrad	T, R	• Better fit than absorbed power law • Good fit for low-S/N spectra • Leaves significant residuals for high-S/N spectra
Accretion disk	tdediscspec[b]	T_p, R_p	• Good fit for most sources • Final model[c] for source with no "hard excess" • Leaves residuals at high energies for source with some hard emission
Accretion disk + Comptonization	simPL⊗tdediscspec[a]	T_p, R_p, f_{sc}, Γ_{sc}	• Accounts for Comptonization of a fraction of disk's photons • Final model[c] for source with "hard excess"

Notes.
[a] All models were preceded by TBabs ×zashift ×.
[b] tdediscspec has an additional nuance parameter γ; see text for discussion.
[c] We also check whether an additional intrinsic neutral absorption was necessary by adding a zTBabs component to the model. Only for ASASSN-14li and AT 2019dsg did it significantly improve the fit and was hence added to the final model. For all other sources, the intrinsic neutral absorption component was negligible.

strong corona formation (i.e., $f_{sc} \geqslant 0.1$) from this analysis; these sources will be separately discussed in Section 4.3.

The temporal evolution of T_p is shown in Figure 8. The cooling of the X-ray continuum is clearly observed: most sources show a peak X-ray temperature at their first available spectra, i.e., the closest to the peak of the UV/optical emission, with a decreasing T_p with time. This behavior is observed even for the sources with faint X-ray emission at early times.

In a Newtonian time-evolving standard disk (Shakura & Sunyaev 1973; Cannizzo et al. 1990), the peak temperature follows a power law in time for a power-law declining accretion rate, $T_p \propto t^{(-n/4)}$, where n depends on the boundary conditions of the accretion disk. For finite stress at the innermost stable circular orbit (ISCO), $n \approx 0.8$, for a vanishing ISCO stress $n \approx 1.2$ (Mummery & Balbus 2020). These solutions seem to qualitatively agree with the observed behavior shown by the solid ($T_p \propto t^{(-1.2/4)}$) and dotted ($T_p \propto t^{(-0.8/4)}$) black lines in Figure 8. The current quality/cadence of available data on X-ray TDEs does not allow for a more detailed assessment of the temperature evolution.

For a standard disk emission, T_p should also correlate with the bolometric luminosity in the form $L_{\rm disk,bol} \propto T^4$, while the relation with the observed X-ray luminosity should have a more general form of $L_X \propto T^{\alpha}$, where α is related to both the temperature evolution (i.e., n) and the measured temperature itself, given that the latter dictates the fraction of the bolometric luminosity emitted in the X-ray band.

In the top panel of Figure 9, we show that such a correlation is observed for several sources. However, some sources, namely, AT 2018zr, AT 2019azh, ASASSN-15oi, and OGLE 16aaa, show a decoupling between L_X and T_p. Such a decoupling is a result of their maximum T_p occurring at early times (like all other sources), while their X-ray luminosity is at the faintest levels at early times ($L_X \leqslant 10^{42}$), which runs contrary to the expectation of higher luminosity at higher temperatures. All these sources are either late-time brightening or X-ray-faint sources. The resulting decoupling, driven by the faint early-time X-ray emission, can also be seen by the color of the points in Figure 9 representing their L_{BB}/L_X values: all sources that show $L_X \propto T^{\alpha}$ (top panel) have $L_{BB}/L_X < 10$ in all epochs, sources with decoupling between L_X and T_p have epochs with $L_{BB}/L_X \gg 10$, and it is in those specific epochs that the decoupling is observed. These results points toward a suppression of the X-ray flux/luminosity in these sources/epochs, while the observed T_p seems be following its expected behavior. An X-ray spectrum of AT 2020ksf (another late-time brightening source) at its early-time X-ray-faint phase is not available to confirm whether such decoupling from the expected relationship is also present.

A similar analysis can be done regarding the apparent radius of the peak disk temperature (R_p); for a standard disk (with no ionizing/neutral absorption and/or reprocessing), the temperature should peak near the ISCO, i.e., $R_p \approx R_{\rm ISCO} = (1\text{–}6) \times R_g$ (depending on the MBH spin), where $R_g = GM_{\rm BH}/c^2$ is the gravitational radius. Given that the (systematic plus statistical) uncertainties in $M_{\rm BH}$ derived from scaling relations (see Section 2.3) are on the order of 0.5 dex, any measured radius in the $0.3 \leqslant R_p/R_g \leqslant 20$ range is still statically consistent with being emitted near the $R_{\rm ISCO}$.

From Figures 10 and 11, it is clear that for most sources/epochs, the recovered R_p are within the physically valid interval (i.e., $0.3 \leqslant R_p/R_g \leqslant 20$) and hence are consistent with $R_{\rm ISCO}$, in agreement with Mummery et al.'s (2023) findings. However, some epochs/sources show unphysically low values, i.e., $R_p/R_g \ll 0.3$; interestingly, these sources show a large apparent R_p evolution, from unphysical values at early times to valid reasonable values at late times. A consequence of this is that the R_p/R_g seems closely connected with L_{BB}/L_X (and hence the distinct light-curve evolution classes): the epochs with $R_p/R_g \ll 0.3$ are the epochs with higher L_{BB}/L_X. This correlation is observed not only for the general sample but also in distinct epochs of the same source (see, e.g., AT 2019azh, OGLE 16aa, and AT 2018zr in Figure 11).

The L_{BB}/L_X (hence the shape of the SED) for a standard accretion disk also has a limiting range of values; based on our simulation shown in Appendix B, for the T_p range measured in our sample (i.e., $5.5{\rm K} \leqslant \log T_p \leqslant 6.1$ K), the ratio between the observed L_{BB} and L_X can only be $5 \times 10^{-2} \leqslant L_{BB}/L_X \leqslant 70$. Combing the valid ranges for L_{BB}/L_X and R_p/R_g, in Figure 11, we show in the gray shaded region the space of parameters in

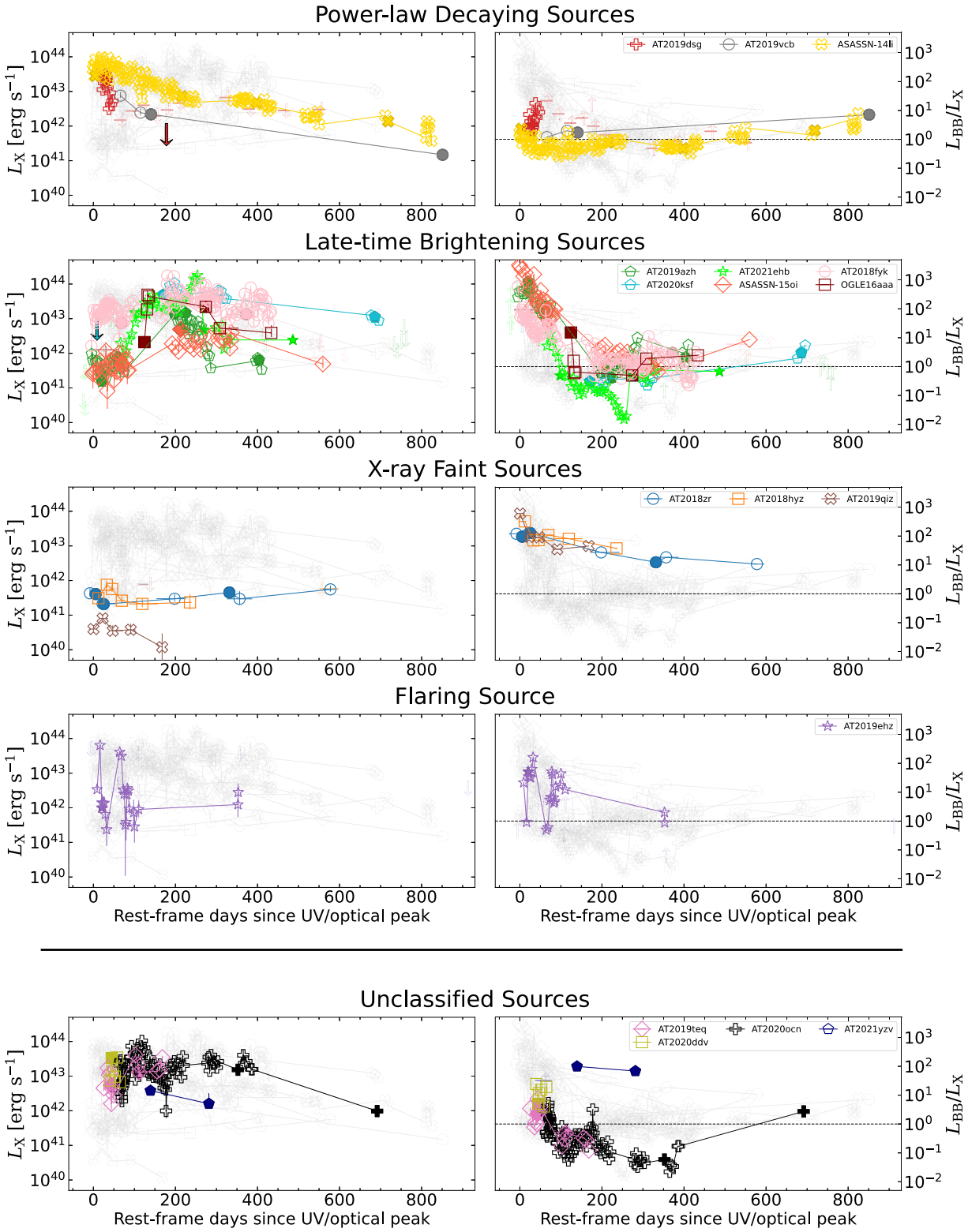

Figure 7. Left: the 0.3–10 X-ray luminosity (L_X). Right: ratio of UV/optical blackbody luminosity to X-ray luminosity (L_{BB}/L_X), where the gray dotted line shows $L_{BB} = L_X$. Top to bottom panels show the different classes of X-ray evolution as described in Section 4.1.

which derived properties *could*, in principle, be explained by a *bare/unreprocessed* accretion disk. For observations that fall outside this region, however, the derived parameters are inconsistent with the ones of a *bare/unreprocessed* disk; hence, additional radiative processes must be present. Interestingly, the epochs/sources in which the measured L_{BB}/L_X and R_p/R_g fall outside the disk region are the same epochs/sources that are decoupled from the $L_X \propto T^{\alpha}$ relation, i.e., all sources showing faint X-ray emission at early times.

In the following paragraphs, we aim to demonstrate that the apparently unphysical R_p/R_g values derived from *X-ray-faint* sources and the early-time observations of *late-time brightening*

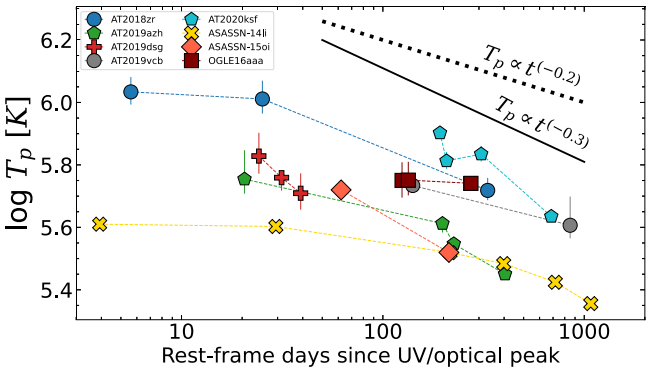

Figure 8. Peak temperature (T_p) of the accretion disk model as a function of days since the UV/optical peak. Only sources with at least two fittable spectra and with no corona emission (see Section 4.3) are shown. The solid black line shows the expected theoretical evolution for a finite stress at the ISCO.

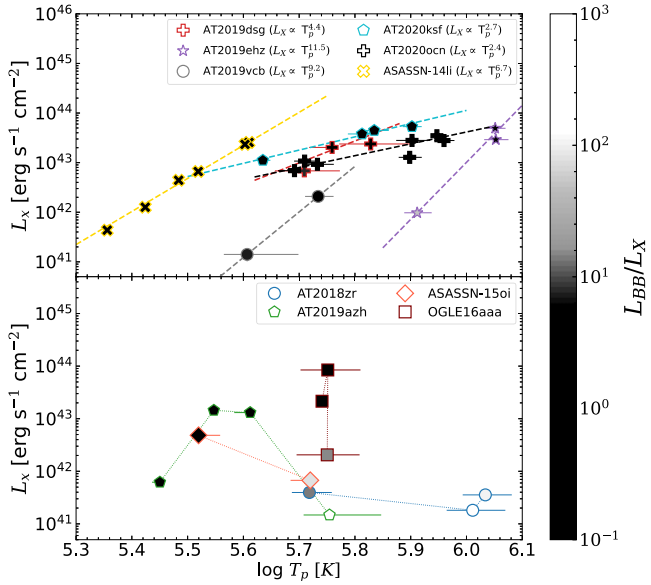

Figure 9. X-ray luminosity (L_X) as a function of peak temperature (T_p). The upper panel shows sources where an $L_X \propto T_p^{\alpha}$ relation is observed, with the best-fit α for each source shown in the legend. The bottom panel shows the source where a clear decoupling between L_X and T_p is present. The color of the markers maps the L_{BB}/L_X ratio between the UV/optical luminosity and the L_X following the color bar on the right side of the figure.

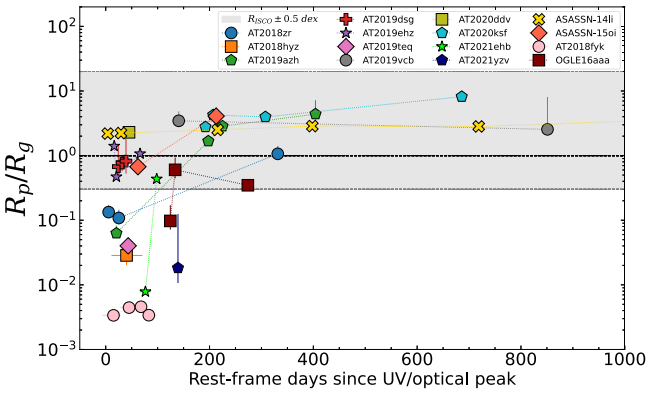

Figure 10. Apparent radius (R_p) of the peak temperature normalized by the gravitational radius (R_g) as a function of days since the UV/optical peak. Only sources with no corona emission (see Section 4.3) are shown. The gray shaded region shows the $0.3 \leqslant R_p/R_g \leqslant 20$ interval in which the measured R_p/R_g is statistically consistent with R_{ISCO}.

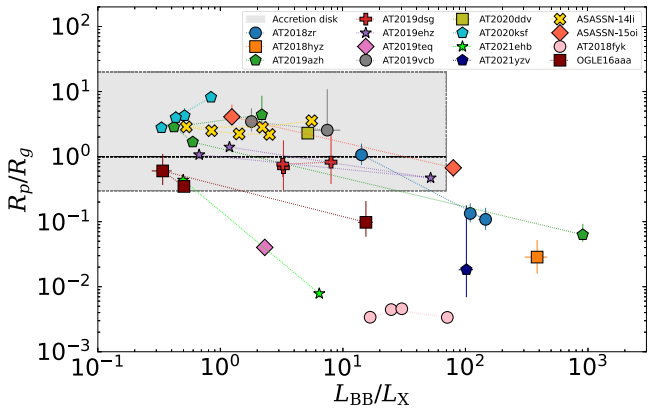

Figure 11. Distribution of the apparent disk radius (R_p) normalized by the gravitational radii (R_g) and the L_{BB}/L_X ratio between the UV/optical luminosity and the X-ray luminosity. The shaded gray region delimits the parameter space in which the emission can be explained by a *bare/unreprocessed* standard accretion disk; see text for details. Several sources/epochs fall outside this region having unphysically low R_p/R_g values while also having SED shapes (L_{BB}/L_X) that deviate from the allowed SED shape of the disk and require additional radiative processes.

are evidence for the suppression of the emitted X-ray in these sources/epochs and can be explained by the way that R_p is "measured" by the X-ray continuum fitting.

In the color-corrected quasi-Wien approximation of `tde-discspec`,[15] the X-ray spectrum ($F_X(\nu)$) is related to R_p and T_p as follows:

$$F_X(\nu) \propto \left(\frac{R_p}{D}\right)^2 \tilde{T}_p^{\gamma} \exp\left(-\frac{h\nu}{k\tilde{T}_p}\right), \quad (3)$$

where $\tilde{T}_p = f_{col} f_{\gamma} T_p$ (see definitions in Section 3) and D is the source luminosity distance. This means that the shape of the X-ray spectra depends exclusively on T_p and not on R_p, which is only a *"physically scaled"* normalization factor that translates the observed count rate per energy bin to a flux per energy bin. Similarly,

$$L_X \propto R_p^2 \tilde{T}_p^{\gamma} \int_{\nu_i}^{\nu_f} \exp\left(-\frac{h\nu}{k\tilde{T}_p}\right) d\nu, \quad (4)$$

where $\nu_i = \frac{0.3\ \mathrm{keV}}{h}$ and $\nu_f = \frac{10\ \mathrm{keV}}{h}$. Therefore, for a constant T_p, $L_X \propto R_p^2$, while L_X decreases with decreasing T_p for a constant R_p.

As we have shown, all sources—including those with faint X-ray emission at early times—show a decreasing or constant T_p with time; this means that their faint X-ray emission and late-time X-ray brightening (or constant L_X, in AT 2018zr) will translate into to an extremely low R_p at early times and an order-of-magnitude increase in R_p at late times. Such behavior is a consequence of Equation (4), in which R_p cannot be constant with time if T_p is decreasing (or held constant) and L_X is not decreasing—as is the case for all sources in the bottom panel of Figure 9.

One can take the earliest ($\Delta t = 21$ days) spectrum of AT 2019azh as an example: the measured temperature and apparent radius were $\log T_p \approx 5.75$ K and $R_p/R_g \approx 6 \times 10^{-2}$, while $L_X \approx 2 \times 10^{41}$ erg s^{-1}. In order for the R_p/R_g to be within the

[15] The specific equations are for `tdediscspec`, but the same arguments hold for any thermal model.

physically valid range (i.e., to be at least 0.3), based on Equation (4), the observed luminosity would have to be higher by a factor of $\left(\frac{0.3}{0.06}\right)^2 \approx 25$; similarly, for the early-time R_p/R_g to be at the same value as the late-time $R_p/R_g \approx 3$ (hence a physically valid and approximately constant value during its entire evolution), the observed early-time L_X would have to be higher by a factor of $\left(\frac{3}{0.06}\right)^2 \approx 2 \times 10^3$. Such an increase would make the early-time L_X coupled to the T_p during the entire evolution of the source, as can be seen by the bottom panel of Figure 9.

A similar analysis can be done for the early-time spectra of all the *late-time brightening* and *X-ray-faint* sources that show this unphysical value/evolution of the apparent R_p; for all of them, an increase in the L_X by a factor of $\gg$10 is necessary for a physical value of R_p/R_g, given their measured temperature evolution.

In summary, the unphysical values of R_p/R_g, accompanied by decoupling between L_X and T_p and an SED shape (L_{BB}/L_X) inconsistent with an accretion disk, indicate suppression of the emitted X-rays in these epochs/sources. However, such suppression of the X-ray emission seems to have a small effect on the measured T_p—given that the cooling of the accretion disk is still observed and is independent of the observed flux level—while suppression of the total observed X-ray flux is high. We will discuss the possible mechanisms responsible for such suppression in Section 5.1. In Mummery et al. (2023), when the authors averaged all R_p values obtained in each spectrum to find a $\langle R_p \rangle$ for each source, the information on the unphysical nature of the R_p/R_g obtained at early times was missed. Furthermore, important data such as the high-S/N X-ray spectra of, for example, AT 2019azh at early times and AT 2018zr at late times, as well as an M_{BH}–σ_* measurement of AT 2018zr's black hole mass, were not available to the authors but are presented here. Although we agree with the authors' main claim, i.e., R_p is tracing R_{ISCO}, we show that this is only valid in the cases where the X-rays are not suppressed and the SED is consistent with a *bare/unreprocessed* disk, which is usually not the case for the very early times of optically discovered TDEs (as we will discuss in Section 4.4).

4.3. Soft → Hard Transition: Real-time Corona Formation

The X-ray spectra of AT 2018fyk, AT 2020ocn, and AT 2021ehb exhibit extreme softness at early times ($\Delta t \leqslant 100$ days), similar to other spectra in our sample. However, these three sources undergo a transition to a hard power-law-like state with a timescale of ~200 days after the UV/optical peak. The power-law component dominates the disk emission in this state and extends to much higher energies than in the soft state. As an extreme example, the NuSTAR spectra of AT 2021ehb presented by Yao et al. (2022) show power-law emission detected above background up to 30 keV.

In the case of AT 2018fyk, a faint hard excess ($f_{sc} \leqslant 0.05$) emerges around $\Delta t \approx 50$ days, followed by rapid formation of a strong coronal component in the range 50 days $\leqslant \Delta t \leqslant$ 200 days. By $\Delta t = 209^{+34}_{-35}$ days, the Swift/XRT spectrum already exhibits $f_{sc} \approx 0.2$, and the corona emission peaks at $\Delta t = 209^{+45}_{-30}$ days with $f_{sc} \approx 0.3$. During this phase, the power-law component dominates the X-ray flux over the thermal component, with the fraction of upscattered photons decreasing to $f_{sc} \approx 0.15$ at $\Delta t \approx 350$ days, remaining relatively constant until the source becomes undetectable in the X-ray at $\Delta t = 500$ days.

In the case of AT 2020ocn, the state transition is more extreme, remaining completely soft and disk-dominated ($f_{sc} = 0.00$) up to $\Delta t \approx 200$ days. However, a spectrum taken after a seasonal gap at $\Delta t \approx 290$ days reveals the corona dominating the X-ray emission ($f_{sc} \approx 0.5$). The source persists in this hard state for at least 100 days, transitioning to an intermediate state again at $\Delta t \approx 700$ days. For AT 2021ehb, a hard excess ($f_{sc} \approx 0.02$–0.05) is present from the first X-ray detections at $\Delta t \approx 70$–100 days. f_{sc} then gradually increases to ~0.15 at $\Delta t \approx 200$ days, followed by an abrupt transition to a corona-dominated state ($f_{sc} \approx 0.5$) at $\Delta t \approx 250$ days, resembling typical AGN X-ray spectra. The source subsequently transitions back to an intermediate state around $\Delta t \approx 300$ days. Figure 12 illustrates the evolution of the softest early-time spectrum (left panels), the hardest spectrum (middle panels), and the intermediate state at very late times (right panels) for the three sources, depicting the formation of the corona.

Transitions from a soft disk-dominated state to a hard corona-dominated state are commonly observed in stellar-mass black holes in XRB systems. They follow a standard *q*-shaped evolution in the hardness–intensity diagram (HID; e.g., Remillard & McClintock 2006; Wang et al. 2022). However, in the case of MBHs, the corona is a ubiquitous and dominant component of the X-ray spectra of AGN. Dramatic state transitions, such as the appearance or disappearance of X-ray power-law emission, are usually not observed in AGN, except in the case of the changing-look AGN 1ES 1927+654 (Trakhtenbrot et al. 2019; Ricci et al. 2020), where the corona was destroyed and later reformed. Therefore, X-ray-bright TDEs provide a new window for studying the emission and formation of this poorly understood component.

A study by Wevers et al. (2021) suggested that AT 2018fyk exhibits a "fainter harder brighter softer" behavior similar to XRB outbursts. Additionally, Wevers (2020) argued that this behavior could be ubiquitous in X-ray-bright TDEs. The HID analysis conducted by Wevers et al. (2021) involved using the α_{OX} parameter, defined as the logarithmic ratio between the UV flux (representing the disk emission) and the 2 keV flux (representing the corona emission), along with the bolometric luminosity (L_{Bol}) normalized by the Eddington luminosity (L_{Edd}).

The HID in the left panel of Figure 13 illustrates corona formation for the three sources using $\frac{f_{sc}}{\max(f_{sc})}$ for hardness and $\frac{L_{BB}+L_X}{L_{Edd}}$ for intensity. Given the uncertainty in the SED shape between the UV and X-ray regions, we use $L_{BB}+L_X$ as a proxy for L_{Bol}[16] and $\frac{L_{BB}+L_X}{L_{Edd}}$ as a proxy for the Eddington ratio. From the left panel of Figure 13, it can be observed that all three sources start in a soft state and then quickly transition to a hard state. The transition occurs at $\frac{L_{BB}+L_X}{L_{Edd}}$ values between 5×10^{-3} and 5×10^{-2} for the three sources. However, as time passes and the luminosity decreases, all sources undergo further transitions, either returning to a completely soft state or transitioning to an intermediate state ($0.05 \leqslant f_{sc} \leqslant 0.15$); this

[16] A significant portion of the bolometric luminosity should be emitted in the unobserved EUV range. The shape of the SED between the UV and X-ray regions is not fully understood and highly dependent on models, especially when the total SED deviates from a standard accretion disk SED (e.g., when $L_{BB}/L_X \gg 10$; see Section 4.4). The actual value of L_{Bol} would be much higher if the EUV emission were taken into account.

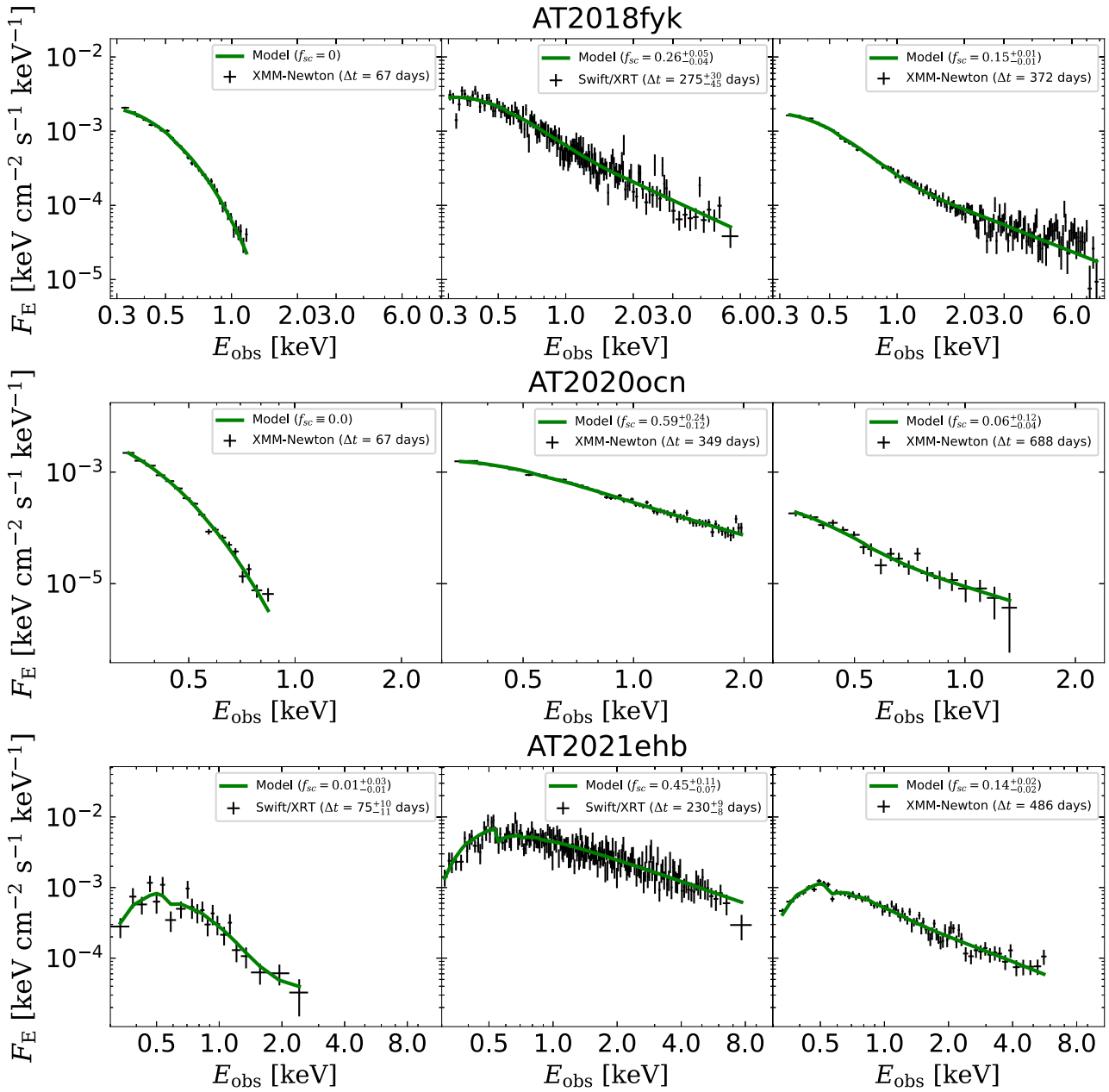

Figure 12. Spectral evolution of the three sources that show soft → hard state transition, i.e., corona formation. From top to bottom: AT 2018fyk, AT 2020ocn, and AT 2021ehb. From left to right: early-time soft-state spectra, hardest-state spectra, and late-time intermediate-state spectra. Unfolded spectra are show with black plus signs, and the best-fit model is shown in green.

behavior contrasts with the *fainter harder brighter softer* pattern.

In the right panel of Figure 13, we compare the power-law index (Γ_{sc}) of the emerging corona in the three TDEs showing a state transition ($f_{sc} \geqslant 0.1$) to the corona power-law index (Γ) measured from the population of unobscured ($N_H \leqslant 10^{22}$ cm^2) AGN in BASS (Ricci et al. 2017). In the AGN population, Γ exhibits values in a narrow range between 1.2 and 2.5 with a mean value of $\Gamma \approx 1.7$. TDEs, however, even at their harder state, are rarely as hard as AGN; instead, their Γ_{sc} can exhibit a broader range of values between 1.7 and 4.0.

The characteristic power-law spectrum is thought to be produced by the Comptonization of lower-energy photons emitted by the accretion disks by a corona of hot electrons (Haardt & Maraschi 1991; Titarchuk & Lyubarskij 1995) located within a light-hour from the accreting MBH (Fabian et al. 2009). The process depends on the Compton parameter y, given by

$$y = \frac{k\ T_e}{m_e\ c^2} \max(\tau_e, \tau_e^2), \quad (5)$$

where τ_e and T_e are, respectively, the corona optical depth and electron temperature of the corona; the resulting power-law spectrum has a photon index with an inverse dependence on y.

Although the exact mechanism responsible for the corona formation is still to be fully understood, the need for a strong magnetic field is a common feature of the different models. In all three sources, the spectrum is soft at early times, and the complete hardening of the X-ray spectrum is only observed at $\Delta t \geqslant 200$ days. This gradual hardening process suggests that it

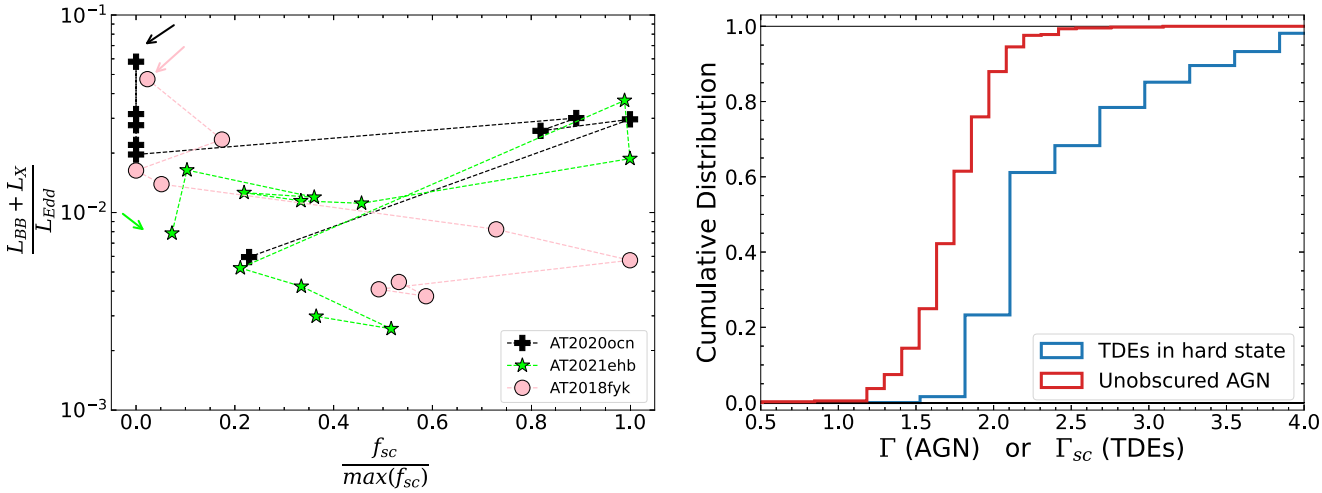

Figure 13. Properties and evolution of the corona emission in TDEs. Left: HID, the total observed luminosity ($L_{\rm BB} + L_{\rm X}$) in units of the Eddington luminosity, as a function of the hardness as traced by the normalized fraction ($f_{\rm sc}$) of the photons upscattered by the corona. The arrows indicate the first available spectra for each source, and the points are connected by increasing Δt. Right: comparison between the power-law index of the corona emission spectra in local AGN (Γ; red) from BASS and TDEs ($\Gamma_{\rm sc}$; blue) that show corona formation (AT 2020ocn, AT 2021ehb, and AT 2018fyk).

takes approximately 10^2 days for the magnetically dominated hot corona region to develop. The initial weak magnetic fields present in the bound debris could undergo amplification through the combined effects of the disk's differential rotation and the magnetorotational instability (Balbus & Hawley 1991; Miller & Stone 2000; Yao et al. 2022).

Although the corona forms in these sources, their hard state is short-lived, transitioning back to a soft/intermediate state at later times ($\Delta t \gg 400$ days). This suggests that the high optical depth corona cannot be sustained as the accretion rate onto the black hole decreases. Another indicator of inefficient corona formation is the measured $\Gamma_{\rm sc}$ (see the right panel of Figure 13). TDE spectra exhibit higher power-law indices compared to typical AGN spectra, translating to lower values of $T_e \times \max(\tau_e, \tau_e^2)$—based on Equation (5) and the inverse relation between Γ and y—when compared with the AGN corona. Distinguishing between the τ_e and T_e effects requires detecting the cutoff energy ($E_{\rm cut}$) of the power-law spectra, feasible with instruments like NuSTAR for bright AGN but currently challenging for TDEs. The proposed High Energy X-ray Probe (Madsen et al. 2019) may enable $E_{\rm cut}$ measurements in bright TDEs. The reasons why only these three sources exhibit corona formation remains unclear; while all three have $M_{\rm BH} \geqslant 5 \times 10^6\ M_\odot$—at the high-mass end of the TDE $M_{\rm BH}$ function and consistent with sub-Eddington accretion requirements—a high $M_{\rm BH}$ alone does not seem sufficient, as other TDEs with similar $M_{\rm BH}$ did not show such state transitions.

4.4. SED Evolution

A natural consequence of the diversity of X-ray light curves and the uniformity of the UV/optical light curves is that the SED shows very distinct shapes and evolution. The shape of the broadband SED can be probed by the $L_{\rm BB}/L_{\rm X}$ ratio. As shown in the right panels of Figure 7, these ratios can vary between few $\times 10^3$ and few $\times 10^{-2}$. In Figure 14, we show the cumulative distribution of $L_{\rm BB}/L_{\rm X}$ at three time bins: early times ($\Delta t \leqslant 50$ days) in purple, late times (150 days $\leqslant \Delta t \leqslant 250$ days) in orange, and very late times (400 days $\leqslant \Delta t \leqslant 800$ days) in black. The SEDs also show a

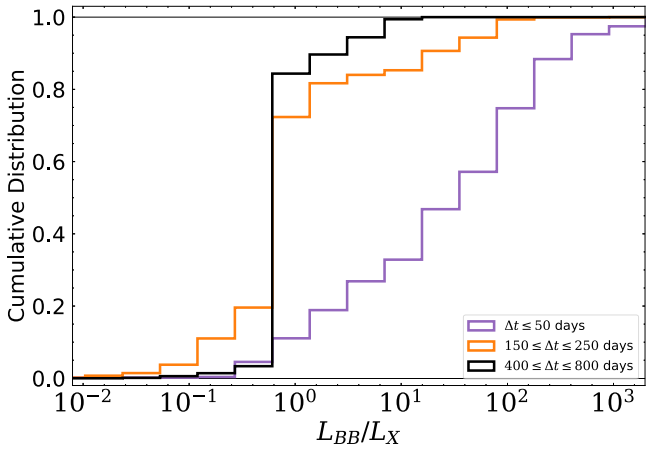

Figure 14. Evolution of the distribution of SED shapes as traced by the ratio ($L_{\rm BB}/L_{\rm X}$) between the UV/optical luminosity ($L_{\rm BB}$) and the 0.3–10 keV luminosity ($L_{\rm X}$). Each color shows the distribution in a different time bin. The contribution of each source for the total distribution was weighed by the number of spectral observations available in each Δt interval.

noticeable trend: at early times, they have an $L_{\rm BB}/L_{\rm X}$ as large as 3000 and as low as 0.5 but with most sources showing $L_{\rm BB}/L_{\rm X} \geqslant 10$; with increasing time from the optical peak, this range of $L_{\rm BB}/L_{\rm X}$ shrinks, and at very late times, all sources show $0.5 \leqslant L_{\rm BB}/L_{\rm X} \leqslant 10$.

As discussed in Section 4.2 and demonstrated in Appendix B, the SED produced by a *bare/unreprocessed* standard accretion disk with T_p in the range of values found in TDEs (i.e., 5.5K $\leqslant \log T_p \leqslant$ 6.1 K) can only produce $5 \times 10^{-2} \leqslant L_{\rm BB}/L_{\rm X} \leqslant 70$. Therefore, the values of $L_{\rm BB}/L_{\rm X}$ in the range 100–3000 found in the early times of a large fraction of our sources indicate that an additional emission mechanism that deviates from a standard accretion disk corona is operating. The deviation from a standard disk is stronger at early phases, given that the $L_{\rm BB}/L_{\rm X}$ ratios converge toward the expected disk values at late times.

In Figure 15, we explore how a standard disk SED compares with the observed SED for three distinct TDEs: one *power-law decaying*, one *late-time brightening*, and one *X-ray-faint*. We assume a color-corrected disk solution, where the SED can be

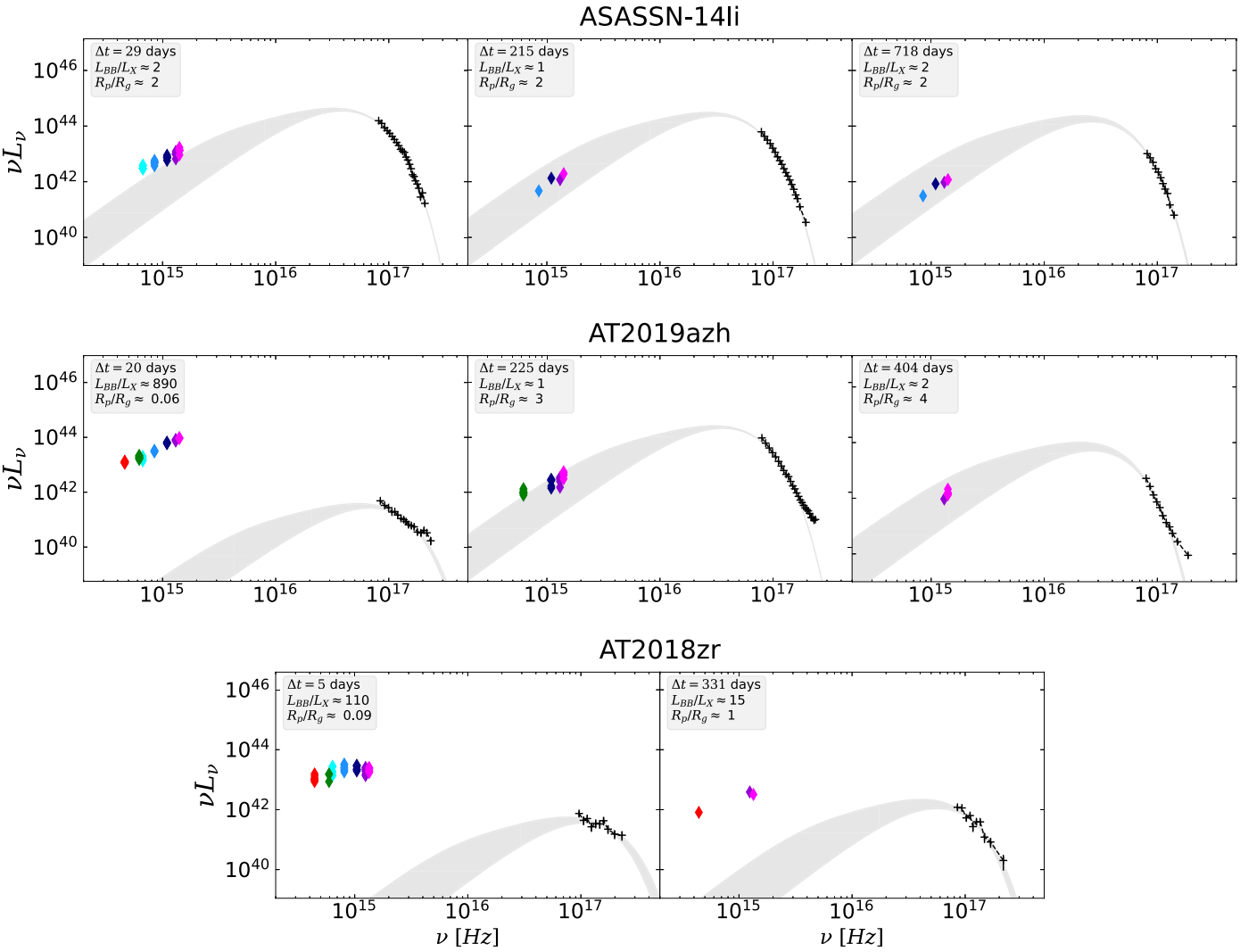

Figure 15. Evolution of the SED for three sources, one *power-law decaying* (top), one *late-time brightening* (middle), and one *X-ray-faint* (bottom). Left panels show early-time ($\Delta t \leqslant 30$ days) SEDs, middle panels show late-time SEDs ($\Delta t \approx 200$ days), and right panels show very-late-time SEDs ($\Delta t \approx 400$ days). No X-ray spectrum of AT 2018zr around $\Delta t \approx 200$ days is available. The colored points show the observed UV/optical photometry (ZTF + Swift/UVOT), the black plus signs show the unfolded X-ray spectrum, the gray line shows the best-fit disk model (and uncertainty) for the X-ray spectra, and extrapolation to the UV/optical band is shown in the shaded region (see text for details). The main parameters of interest are shown in the legend for each epoch.

obtained numerically, as approximately

$$L(\nu) \approx \frac{8\pi^2}{f_{\rm col}^4} \int_{R_p}^{R_{\rm out}} B_\nu(\nu, f_{\rm col}\, T(r))\, r\, dr, \tag{6}$$

where $B_\nu(\nu, T)$ is a Planck function, $T(r)$ is the temperature radial profile of the disk, $T(R_p) = T_p$, and $R_{\rm out}$ is the outer radius of the disk. For given values of the inner temperature ($T_p \pm \delta T_p$) and radius ($R_p \pm \delta R_p$)—obtained from the X-ray fitting—the expected UV/optical emission will depend on the extended disk structure; its size, i.e., $R_{\rm out}/R_p$ ratio; and its temperature profile $T(r)$. At early times, $R_{\rm out}$ should be limited to the circularization radii ($R_{\rm circ}$), which for a solar-like disrupted star are

$$R_{\rm out} = R_{\rm circ} = 2R_T = 94 R_g (M_{\rm BH}/10^6 M_\odot)^{-2/3}, \tag{7}$$

where R_T is the tidal disruption radius. However, at late times, such a requirement is lifted due to the viscous spread of the disk. To emulate our ignorance on the extended properties of the disk, we generated a series of solutions to Equation (6), assuming disk sizes between $R_{\rm out}/R_p \in (5,\ 50)$, temperature profiles of $T(r) \propto r^{-3/4}$ (for a vanishing ISCO stress; Shakura & Sunyaev 1973; Cannizzo et al. 1990) and $T(r) \propto r^{-7/8}$ (for a finite ISCO stress; Agol & Krolik 2000; Schnittman et al. 2016), and the range of the 1σ uncertainty for T_p and R_p. The shaded gray region in Figure 15 represents the region of possible solutions resulting from the assumed parameters. Our goal is to visualize how much the full SED deviates from a standard disk SED and how much UV/optical "excess" is present.

From the top panel of Figure 15, we can see that the SED of ASASSN-14li is not far from an accretion disk SED. Very little UV/optical excess is present even at early times; at late times, the SED is consistent with an accretion disk. Furthermore, the evolution in SED shape with time is very small and compatible with the cooling of the disk. The same holds for the other *power-law decaying* sources, although for AT 2019dsg, the rapid decay of X-ray emission indicates a quicker cooling of the disk (Cannizzaro et al. 2021).

For AT 2019azh, however, the disk emission extrapolated from the X-rays underpredicts the UV/optical emission by

more than 2 orders of magnitudes, as can be seen from the left middle panel of Figure 15. This is mainly a consequence of the low X-ray luminosity $L_X \approx 5 \times 10^{41}$ erg s^{-1} and high T_p that result in both an unphysical R_p/R_g and a high $L_{BB}/L_X \approx 890$. At later times, however, L_{BB} decays and L_X brightens ($L_{BB}/L_X \approx 1$), and the SED is consistent with a standard accretion disk. Such behavior is observed in all *late-time brightening* sources. One should notice that in AT 2021ehb, the L_{BB}/L_X reaches an extremely low value of $\sim 10^{-2}$ given the strong corona formation that increases L_X, consequently decreasing L_{BB}/L_X.

In the case of AT 2018zr, the early time is very similar to AT 2019azh; however, even at $\Delta t \approx 331$ days, the SED is not yet consistent with a standard disk, although the UV/optical excess does decrease, while L_X is approximately constant during the entire evolution. Similar behavior is found in the other *X-ray-faint sources*. The physical interpretation of the diversity of SED shapes at early times and the convergence to a disklike SED at late times will be discussed and compared with the theoretical expectations in Section 5.1.

As discussed in Section 4.2, there is a clear anticorrelation between L_{BB}/L_X and the radius derived from the X-ray spectral fitting. R_p/R_g assumes nonphysical values at the highest L_{BB}/L_X (usually with $L_{BB}/L_X \gg 10$); this can also be seen in the legend of Figure 15. In light of the discussion of this section and Section 4.2, we can conclude that R_p/R_g values are nonphysical when the SED strongly deviates from the SED of a standard disk. Both lines of evidence point toward the suppression of the observed X-ray emission as discussed in Section 4.2.

4.5. The Ratio of X-Ray-loud TDEs in Optical Surveys and Its (In)dependence on M_{BH}

A surprising characteristic of the population of TDEs discovered by optical surveys is the lack of detectable X-ray emission in most sources, contrary to the first theoretical expectation (Rees 1988) and the fact that the first TDEs were discovered in the X-ray (e.g., Bade et al. 1996). We would like to determine the fraction ($N_{opt,x}/N_{opt}$) of optically discovered TDEs that show X-ray emission. Therefore, a controlled sample of the total discovered TDEs and X-ray-bright TDEs needs to be compared.

We will use the first 3 yr of the ZTF (2018 October–2020 August for ZTF-I and 2020 September–2021 August for ZTF-II) survey to determine this ratio. After a ZTF TDE candidate (see van Velzen et al. 2021; Yao et al. 2023 for selection criteria) is spectrally classified, a few Swift observations are performed to confirm the UV brightness characteristic of the TDE and check whether the source is detected in the X-ray. The number of visits and the cadence vary from source to source, but at a minimum, a few 1–2 ks long observations (usually with a total of ∼10 ks) are performed, leading to a detection limit of $\sim 5 \times 10^{-14}$ erg cm^{-2} s^{-1} with XRT, which means any TDE with $L_X > 10^{42}$ erg s^{-1} can be detected up to $z \approx 0.09$, while $L_X \sim 10^{41}$ erg s^{-1} can only be detected if extremely nearby ($z < 0.04$). Therefore, we will use $L_X \geqslant 10^{42}$ erg s^{-1} to define the subsample of X-ray-bright TDEs. During the first 3 yr of ZTF, 10 sources showed, at some point in time, $L_X \geqslant 10^{42}$ erg s^{-1}; therefore, $N_{opt,x} = 10$.

To construct the control sample, we start with all TDEs discovered by ZTF during the same time period (from van Velzen et al. 2021; Hammerstein et al. 2023a; Yao et al. 2023). For sources at $z < 0.09$ (24 sources), we select those with Swift/XRT observations; for sources with no XRT detection, we stack all their Swift/XRT observations and check whether the L_X upper limit (after correcting for Galactic absorption) was deeper than 10^{42} erg s^{-1}. Only for three sources (AT 2021mhg, AT 2021sdu, and AT 2021yte) the upper limit were not deep enough to constrain the presence $L_X \geqslant 10^{42}$ erg s^{-1}, particularly because of their higher Galactic absorption $N_{H,G} \geqslant 10^{21}$ cm^{-2}, than the typical $N_{H,G} \approx$ few $\times 10^{20}$ cm^{-2} of the other sources. For our typical exposure times, the XMM-Newton detection limit is around 5×10^{-15} erg cm^{-2} s^{-1}; this means that we can detect $L_X > 10^{42}$ erg s^{-1} up to $z \approx 0.25$. Therefore, we include all sources at $0.09 \leqslant z \leqslant 0.25$ that had at least one XMM-Newton visit to our control sample (adding four more sources). This results in 25 sources in which $L_X \geqslant 10^{42}$ erg s^{-1} could be (or was) detected if such a level of emission was present, hence $N_{opt} = 25$. Therefore, for ZTF, we obtain $N_{opt,x}/N_{opt} = 10/25$, meaning that in ZTF, ∼40% of the discovered TDEs (eventually) had some X-ray-bright emission ($L_X \geqslant 10^{42}$ erg s^{-1}). The list of the 25 TDEs and their redshift is presented in Table 5. Given the nonuniformity of the X-ray follow-up, particularly at late times for those at higher z, the ratio should be seen as a lower limit.

We also use the above-defined subsamples to investigate whether the presence of $L_X \geqslant 10^{42}$ is dependent on M_{BH}. In Figure 16, we show the cumulative distribution of M_{BH} for the two subsamples (L_X higher and lower than 10^{42} erg s^{-1}), where the underlying distribution was constructed by adding a normalized probability distribution function (PDF) based on the estimated M_{BH} and their uncertainties (see Section 2.3).

Table 5
ZTF Control Sample, Described in Section 4.5

Source	z	$L_X \geqslant 10^{42}$ erg s^{-1}	log ($M_{BH}/M_\odot$)[a]
AT 2018zr	0.075	False	5.83 ± 0.51
AT 2018bsi	0.051	False	7.46 ± 0.47
AT 2018hco	0.088	False	6.44 ± 0.48
AT 2018iih	0.212	False	7.93 ± 0.48
AT 2018hyz	0.046	False	6.12 ± 0.46
AT 2018lna	0.091	False	5.21 ± 0.54
AT 2019azh	0.022	True	6.68 ± 0.46
AT 2019dsg	0.051	True	7.04 ± 0.45
AT 2019ehz	0.074	True	5.75 ± 0.59
AT 2019mha	0.148	False	6.41 ± 0.49
AT 2019meg	0.152	False	5.81 ± 0.52
AT 2019qiz	0.015	False	6.49 ± 0.49
AT 2019teq	0.087	True	6.32 ± 0.49
AT 2020pj	0.068	False	6.43 ± 0.49
AT 2019vcb	0.088	True	5.59 ± 0.52
AT 2020ddv	0.160	True	6.09 ± 0.55
AT 2020ksf	0.092	True	5.92 ± 0.48
AT 2020ocn	0.070	True	6.77 ± 0.49
AT 2020mot	0.070	False	7.04 ± 0.47
AT 2020wey	0.027	False	5.38 ± 0.51
AT 2020zso	0.057	False	6.12 ± 0.48
AT 2020vwl	0.033	False	5.80 ± 0.48
AT 2021ehb	0.018	True	7.04 ± 0.46
AT 2021nwa	0.047	False	7.21 ± 0.46
AT 2020ksf	0.092	True	5.92 ± 0.48
AT 2021yzv	0.286	True	7.45 ± 0.47

Note.
[a] Black hole masses. When a σ_* measurement is available, it is estimated using the Gültekin et al. (2019) σ_*–M_{BH} relation; when σ_* is not available, this is estimated from the M_*–M_{BH} relation presented in Yao et al. (2023).

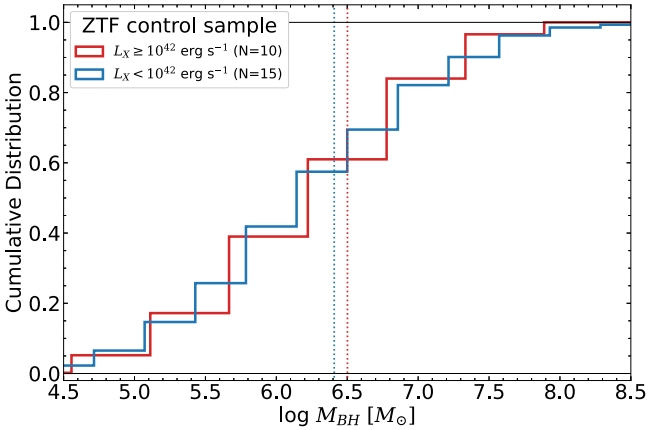

Figure 16. Cumulative distribution of black hole mass for the *ZTF control sample* (see Section 4.5 for definition) with L_X higher or lower than 10^{42} erg s^{-1}. The underlying distribution was constructed by adding the normalized PDF of individual sources M_{BH} based on the estimated values and uncertainties. No statistically significant difference in the distributions is observed.

From Figure 16, there seems to be no distinction between the M_{BH} distribution of TDE L_X higher/lower than 10^{42} erg s^{-1}: the difference in the median of the distributions (dotted vertical lines) is only ∼0.1 dex, which is much smaller than the typical uncertainty in M_{BH}. In order to statistically investigate the (lack of) difference between the distributions, we apply a Kolmogorov–Smirnov test. Assuming the null hypothesis that the two samples are drawn from the same distribution, we recover a p-value of ∼0.2, which means the null hypothesis cannot be excluded; hence, there is no statistically significant difference between the distributions. This result is in agreement with previous ones that, although they use distinct samples or selection criteria, also did not find any correlation between X-ray loudness and M_{BH} (Wevers et al. 2019b; French et al. 2020; Hammerstein et al. 2023a, 2023b),

4.6. X-Ray Luminosity Function

When examining sources with constant flux, such as quasars, the estimation of their luminosity function (LF) involves assigning weights to each source based on its maximum detectable volume, V_{max}, as introduced by Schmidt (1968). This approach enables plotting of the number of sources per unit volume as a function of their luminosity. Shifting to transient events, like supernovae and TDEs, our interest lies in understanding their volumetric rate, i.e., the number of events per unit volume per unit time relative to their peak luminosity. Extracting this rate from survey data involves applying the "$1/V_{max}$" method, with a modification accounting for both survey duration and area. This adaptation leads to the definition of a modified parameter, $\mathcal{V}_{max}$:

$$\mathcal{V}_{max} = V(z_{max})\, A_{survey} \times \tau_{survey}, \quad (8)$$

where $A_{survey} \times \tau_{survey}$ denotes the product of the effective survey duration and survey area and $V(z_{max})$ is the volume (per unit solid angle) corresponding to the maximum redshift observable with the survey, given its limiting flux.

The LFs of TDEs across different bands have been investigated by a few studies. Van Velzen (2018) initially presented a *relative* LF in the single-band optical and integrated UV/optical for TDEs, utilizing 13 events discovered before 2018 through UV/optical surveys. Subsequently, Yao et al. (2023) provided an *absolute* UV/optical LF derived from a sample of 33 homogeneously selected TDEs identified by ZTF. In the X-ray domain, Sazonov et al. (2021) constructed the first LF based on 13 events selected from X-ray transients detected in the $0° < l < 180°$ hemisphere during SRG/eROSITA's second sky survey. The X-ray LF spanned from $10^{42.5}$ to $\leqslant 10^{45}$ erg s^{-1} and was best fit with a power-law slope of 0.6 ± 0.2. However, as the X-ray-bright TDEs in our study were not discovered by an X-ray survey but through inhomogeneous follow-up X-ray observations of optically discovered TDEs, and given the nonuniform criteria and cadence for X-ray follow-up, we refrain from obtaining an *absolute* X-ray LF akin to Sazonov et al. (2021). Instead, we propose combining TDEs detected by X-ray surveys with our sample of optically selected X-ray-detected TDEs to construct a *relative* LF. This approach aims to provide a broader luminosity range and reduced uncertainty per luminosity bin compared to the one derived from SRG/eROSITA, thereby enhancing our ability to constrain its shape.

To construct a large sample of X-ray TDEs, we combine our 17 sources, the 13 discovered by SRG/eROSITA (Sazonov et al. 2021), 6 discovered by ROSAT/RASS, and 8 discovered by the XMM-Newton Slew Survey as presented in the recent review by Saxton et al. (2020), resulting in 44 X-ray-detected TDEs in the range 10^{41} erg s^{-1} $\leqslant L_X \leqslant 10^{45}$ erg s^{-1}.

We follow the procedures detailed in van Velzen (2018) to construct a *relative* LF from a combined sample discovered by distinct surveys with distinct selection functions and detection efficiency, assuming that each survey discovers events from the same parent distribution so that we can use the discovered/detected number of TDEs in each survey to compare the selection efficiencies and thus obtain the *relative* LF. The *effective* $(A_{survey} \times \tau_{survey})^*$ (see Equation (8)) for each survey can be estimated from

$$(A_{survey} \times \tau_{survey})^* \approx \frac{N_{TDE,\,detected}}{\dot{N}\, V(z_{max*})}, \quad (9)$$

where $N_{TDE,detected}$ is the number of TDEs detected by the survey and $V(z_{max*})$ denotes the comoving volume (per solid angle) corresponding to the maximum redshift (z_{max*}) at which the survey can detect a "typical" X-ray TDE. We define a "typical" X-ray TDE to have $L_X^* = 10^{43}$ erg s^{-1} and $T_p^* = 60$ eV and use the detection limit flux ($F_{X,lim}$) of each survey (see Table 6) to determine the z_{max*} for each survey. For the optical survey, we assume $F_{X,lim}$ to be the flux limit of Swift/XRT in a stacked exposure time of 10 ks. In Equation (9), $\dot{N}$ is the *assumed* mean event rate, which was chosen to be $\dot{N} = 2 \times 10^{-7}$ Mpc^{-3} yr^{-1}, following Sazonov

Table 6
Survey Properties

Survey	N_{TDE}	$F_{X,lim}$ (erg cm^{-2} s^{-1})	$(A_{survey} \times \tau_{survey})^*$[a] (deg^2 yr)
ASASSN+Swift/XRT	6 (3)[b]	8×10^{-14}	138
ZTF+Swift/XRT	12	8×10^{-14}	273
OGLE+Swift/XRT	1	8×10^{-14}	22
ROSAT	6	2×10^{-13}	2009
XMMLS	9	5×10^{-13}	6484
eROSITA	14	8×10^{-14}	645

Notes.
[a] Effective $A_{survey} \times \tau_{survey}$ as measured from Equation (9).
[b] Three were part of both in ZTF and ASASSN.

Table 7
LF Data

Source	z	"Peak" L_X (erg s^{-1})	Survey
AT 2018zr	0.071	5.55×10^{41}	ZTF
AT 2018hyz	0.045	7.51×10^{41}	ZTF/ASASSN
AT 2019azh	0.022	1.65×10^{43}	ZTF/ASASSN
AT 2019dsg	0.051	3.90×10^{43}	ZTF
AT 2019ehz	0.074	6.35×10^{43}	ZTF
AT 2019qiz	0.015	8.06×10^{40}	ZTF/ASASSN
AT 2019teq	0.087	4.06×10^{43}	ZTF
AT 2019vcb	0.088	1.66×10^{43}	ZTF
AT 2020ddv	0.160	3.45×10^{43}	ZTF
AT 2020ksf	0.092	1.07×10^{44}	ZTF/eROSITA
AT 2020ocn	0.070	1.04×10^{44}	ZTF
AT 2021ehb	0.018	1.78×10^{44}	ZTF
ASASSN-14li	0.020	9.77×10^{43}	ASASSN
ASASSN-15oi	0.048	4.93×10^{42}	ASASSN
AT 2018fyk	0.059	1.76×10^{44}	ASASSN
OGLE 16aaa	0.165	4.92×10^{43}	OGLE
AT 2021yzv	0.288	3.83×10^{42}	ZTF
J135514.8+311605	0.199	5.80×10^{43}	eROSITA
J013204.6+122236	0.123	4.20×10^{43}	eROSITA
J153503.4+455056	0.231	8.80×10^{43}	eROSITA
J163831.7+534020	0.581	2.50×10^{44}	eROSITA
J163030.2+470125	0.294	2.00×10^{44}	eROSITA
J021939.9+361819	0.387	2.50×10^{44}	eROSITA
J161001.2+330121	0.131	1.20×10^{43}	eROSITA
J171423.6+085236	0.036	5.30×10^{42}	eROSITA
J071310.6+725627	0.104	1.10×10^{44}	eROSITA
J095928.6+643023	0.045	8.90×10^{44}	eROSITA
J091747.6+524821	0.187	4.80×10^{44}	eROSITA
J133053.3+734824	0.150	3.40×10^{43}	eROSITA
J144738.4+671821	0.125	2.70×10^{43}	eROSITA
NGC 5905	0.011	7.00×10^{42}	ROSAT
RX J1624+7554	0.064	2.00×10^{44}	ROSAT
RBS 1032	0.026	1.00×10^{43}	ROSAT
RX J1420+5334	0.147	2.50×10^{44}	ROSAT
RX J1242–1119	0.050	4.00×10^{44}	ROSAT
TDXF 1347–3254	0.037	7.00×10^{42}	ROSAT
NGC 3599	0.003	1.20×10^{41}	XMMLS
SDSS J1323+48	0.087	4.40×10^{43}	XMMLS
SDSS J0939+37	0.184	2.60×10^{44}	XMMLS
2MASX J0203–07	0.062	2.80×10^{43}	XMMLS
2MASX J02491–04	0.019	2.10×10^{42}	XMMLS
SDSS J1201+30	0.146	3.00×10^{44}	XMMLS
2MASX 0740–85	0.017	2.00×10^{43}	XMMLS
XMMSL2 J1446+68	0.029	6.00×10^{42}	XMMLS
XMMSL1 J1404	0.043	3.00×10^{43}	XMMLS

et al. (2021). The resulting $(A_{\rm survey} \times \tau_{\rm survey})^*$ for each survey is shown in Table 6, while Table 7 shows the detailed information from individual sources.

In the upper panel of Figure 17, we show the distribution of the 44 TDEs in the redshift-versus-peak L_X diagram, where the boundaries of the nine $\Delta\log L_X$ bins are indicated with vertical lines. For a certain bin j with n_j TDEs and width $\Delta_j \log L_X$, the rate LF is $\phi_j = \left[\sum_{i=1}^{n} \frac{1}{V_{\rm max,i}}\right] \Big/ \Delta_j \log L_X$, and we compute the corresponding uncertainty of ϕ_j based on the Poisson error (Gehrels 1986). For example, when $n_j = 1$, the upper and lower limits of ϕ_j are $\phi_j^u = \phi_j \times 3.30/1$ and $\phi_j^l = \phi_j \times 0.17/1$, and when $n_j = 11$, $\phi_j^u = \phi_j \times 14.27/11$ and $\phi_j^l = \phi_j \times 7.73/11$. We show ϕ_j versus $\log L_X$ in the bottom panel of Figure 17.

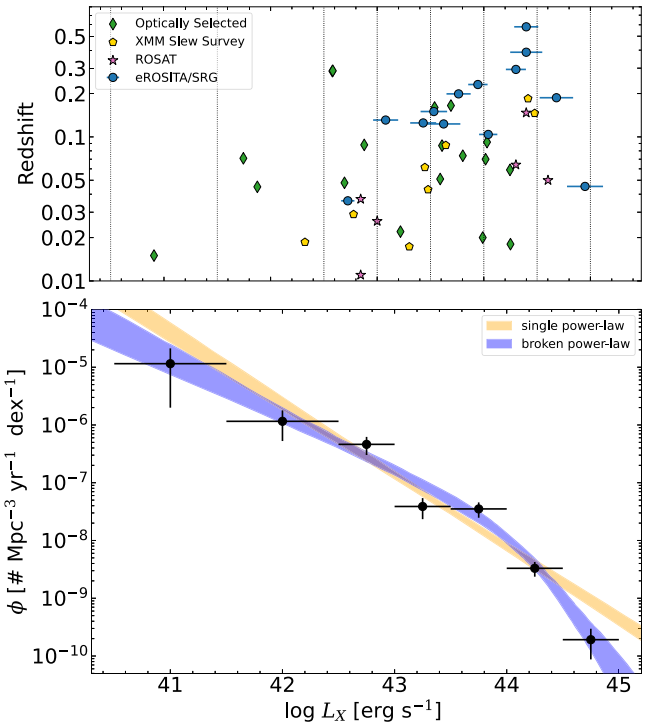

Figure 17. Top: distribution of redshift × peak X-ray luminosity (L_X) for all the sources included in the X-ray LF analyses. Bottom: derived LF (black points), best-fit single power law (orange), best-fit broken power law (blue).

First, we fit the seven LF data points with a single power law of

$$\phi(L_X) = \dot{N}_0 \left(\frac{L_X}{L_0}\right)^{-\gamma}. \quad (10)$$

For $L_0 = 10^{43}$ erg s^{-1}, we obtained $\gamma = 1.2 \pm 0.1$. The best-fit model, shown as an orange line in the bottom panel of Figure 17, is steeper than the power-law model with $\gamma = 0.6 \pm 0.2$ presented by Sazonov et al. (2021); however, the fit seems to slightly overpredict the number of low-L_X sources and the number of sources with $L_X \geqslant 10^{44.5}$ erg s^{-1}.

Next, we describe the LF with a broken (or double) power law in the form of

$$\phi(L_X) = \dot{N}_0 \left[\left(\frac{L_X}{L_{\rm bk}}\right)^{\gamma_1} + \left(\frac{L_X}{L_{\rm bk}}\right)^{\gamma_2}\right]^{-1}. \quad (11)$$

Performing a broken power-law fit to the LF of TDEs, with $-\gamma_1$ representing the faint-end slope, $-\gamma_2$ the bright-end slope, and $L_{\rm bk}$ the characteristic break luminosity, we utilize MCMC to obtain $\gamma_1 = 0.96^{+0.21}_{-0.24}$, $\gamma_2 = 2.65^{+1.1}_{-0.90}$, and $\log L_{\rm bk} = 44.1^{+0.4}_{-0.5}$ erg s^{-1}. The Bayesian information criterion (BIC) favors the broken power-law fit over the single power-law fit, with a smaller BIC value by 7.1. This suggests that the broken power-law LF provides a superior description of the data. Notably, our determined γ_1 below the break is steeper than the $\gamma = 0.6 \pm 0.2$ reported by Sazonov et al. (2021), indicating a potential underestimation of the low-L_X end and/or overestimation of the high end of the LF in their work. The selection bias in Sazonov et al.'s (2021) criteria, favoring sources with an observed flux at least 10 times brighter than the previous upper limit, may contribute to underestimating the low-luminosity end. Our findings reveal an extension of the LF to L_X values below $10^{42.5}$ erg s^{-1} (Sazonov et al.'s 2021 lowest L_X bin),

reaching as low as $L_X \approx 10^{41}$ erg s^{-1}. This suggests a sizable population of X-ray-emitting TDEs that are too faint for current instruments unless occurring at very low redshifts, emphasizing that the absolute rate estimated by Sazonov et al. (2021) represents a lower limit on the rate of X-ray-emitting TDEs.

In the case where the X-ray luminosities of TDEs are Eddington-limited, and hence their fraction $l_x = L_X/L_{Edd}$ is <1, the observed suppression of the TDE rate at $M_{BH} > 10^8\ M_\odot$ (van Velzen 2018; Yao et al. 2023) can naturally explain the break in the X-ray LF at $\sim 10^{44}$ erg s^{-1}. Indeed, based on such arguments, Mummery (2021) estimated a *maximum* X-ray luminosity of $\sim 10^{44}$ erg s^{-1} for nonjetted TDEs.[17] Although a couple TDEs have shown a peak $L_X > 10^{44}$ erg s^{-1} (see top panel of Figure 17), the steep break from $\gamma \approx 1.0$ to $\gamma \approx 2.7$ in the LF is still in qualitative agreement with the limiting luminosity expectation, given that a TDE with peak $L_X = 10^{45}$ erg s^{-1} should be $\sim$1000 times rarer than a TDE with peak $L_X = 10^{44}$ erg s^{-1}.

5. Discussion

5.1. On the Diversity of X-Ray Evolution: Delayed Accretion or Variable Optical Depth? An Orientation Effect?

As we have shown in Section 4.1, optically selected TDEs have a large diversity in X-ray evolution, with sources rarely showing prompt ($\Delta t \leqslant 100$ days), bright ($L_X \geqslant 10^{43}$ erg s^{-1}) X-ray emission that decays as a power law with time as predicted from simple fallback accretion models. Instead, most sources show a faint X-ray emission at early times, with a subset showing a delayed increase in the observed X-ray luminosity, while others show a faint and approximately constant X-ray luminosity during the UV/optical evolution.

From our X-ray spectral and SED analyses, a number of conclusions can be drawn.

1. The X-ray emission temperature (T_p) decreases with time (see Figure 8).
2. The decrease in T_p is independent of L_X, given that *late-time brightening* sources show the highest T_p at early times, when the L_X is minimum.
3. This independent T_p and L_X evolution creates a decoupling between the two parameters in these epochs/sources. Other epochs/sources show an $L_X \propto T^\alpha$ relation (see Figure 9).
4. The highest T_p with the lowest L_X results in an unphysical value for the X-ray emission radius (R_p/R_g) for these sources/epochs. For other sources/epochs R_p is consistent with R_{ISCO} (see Figure 10).
5. The epochs with unphysical R_p/R_g are also the epochs in which the UV/optical-to-X-ray ratio (L_{BB}/L_X) is too high to be produced by a *bare/unreprocessed* accretion disk (see Figure 11).
6. There is a large range of observed L_{BB}/L_X values at early times ($0.5 \leqslant L_{BB}/L_X \leqslant 3000$); at late times, these values converge to ($0.5 \leqslant L_{BB}/L_X < 10$); see Figure 14.
7. There is no M_{BH} dependence on the presence/absence of luminous X-ray emission ($L_X \geqslant 10^{42}$ erg s^{-1}).

Viable theoretical models for the TDE emission mechanism must be able to reproduce these observational findings.

A possible explanation for the late-time brightening of the X-ray emission, put forward by several authors (e.g., Gezari et al. 2017; Liu et al. 2022), is the delayed formation of the accretion disk in these sources. Some problems arise from this interpretation.

(i) Soft X-ray emission (though faint, $L_X \leqslant 10^{42}$ erg s^{-1}) is detected in early times for all of the *late-time brightening* sources in which an observation deep enough to detect such faint emission is available,[18] which means that the structure responsible for X-ray emission in these sources is already present at very early times, i.e., is promptly formed.

(ii) The temperatures of these X-ray-faint phases are as high as or higher than the temperatures at the late time.

(iii) The overall evolution of the temperature is consistent with a cooling accretion disk (see Figure 8), which would not necessarily be the case if the late-time X-ray emission is tracing a different physical structure (disk) than the early time is tracing (stream–stream shocks), as proposed by Liu et al. (2022).

(iv) If the presence of bright X-ray emission ($L_X > 10^{42}$ erg s^{-1}) is driven by the successful circularization of the debris streams, while in sources with $L_X \leqslant 10^{42}$ erg s^{-1}, these do not circularize to form a disk, there should be a distinct M_{BH} distribution underlying the two populations given the strong M_{BH} dependence in the circularization time (Bonnerot et al. 2016). As we have shown in Figure 16, there is no difference in their M_{BH} distributions.

As we argued in Section 4.2, the observed properties seem to point toward the presence of prompt but suppressed X-ray emission in the early times of the *late-time brightening* and *X-ray-faint* sources. Suppression of the X-ray emission is an expected consequence of different TDE models that invoke the reprocessing of the high-energy emission into the UV/optical wavelengths by an optically thick material. These models (e.g., Loeb & Ulmer 1997; Ulmer 1999; Coughlin & Begelman 2014; Metzger & Stone 2016; Roth et al. 2016; Dai et al. 2018; Metzger 2022; Parkinson et al. 2022; Thomsen et al. 2022) assume different physical processes and geometries but have the common property of reprocessing of the X-ray emission at the highest accretion rates, i.e., early times, and its reemission at lower energies. Although a large fraction of the optical TDEs in our sample show suppression of the X-ray emission at early times, some do not, namely, ASASSN-14li, AT 2019vcb, AT 2019dsg, and AT 2019ehz; this is also true for most X-ray-discovered TDEs (a comparison between these populations will be presented in Section 5.4). Instead, there is an at least 3 orders of magnitude range in observed L_{BB}/L_X at early times (see Figures 14 and 15). Some of this diversity was already previously known and had inspired a series of models where the presence/absence of strong reprocessing is orientation-dependent (e.g., Dai et al. 2018; Jonker et al. 2020; Thomsen et al. 2022).

In these models, the optical depth through the line of sight for the high-energy photons has a strong dependence on the accretion rate and likely on the viewing angle at the highest accretion rate, i.e., early times, if the source is seen at lower inclination angles with respect to the disk pole. The optical depth (τ), and hence the reprocessing, is minimal, and the observed SED resembles the one of the underlying disk (i.e., $L_{BB}/L_X \lesssim 10$; see Appendix B), which would explain the

[17] TDEs in which the jet is pointed toward us—so-called jetted or relativistic TDEs—have their luminosity beamed; hence, those can reach $L_X \geqslant 10^{47}$ erg s^{-1}. This is a distinct physical scenario from what is discussed in this section and therefore is not considered.

[18] The upper limits on AT 2020ksf and OGLE 16aa are higher than 10^{42} erg s^{-1}; the two are also the highest-redshift sources.

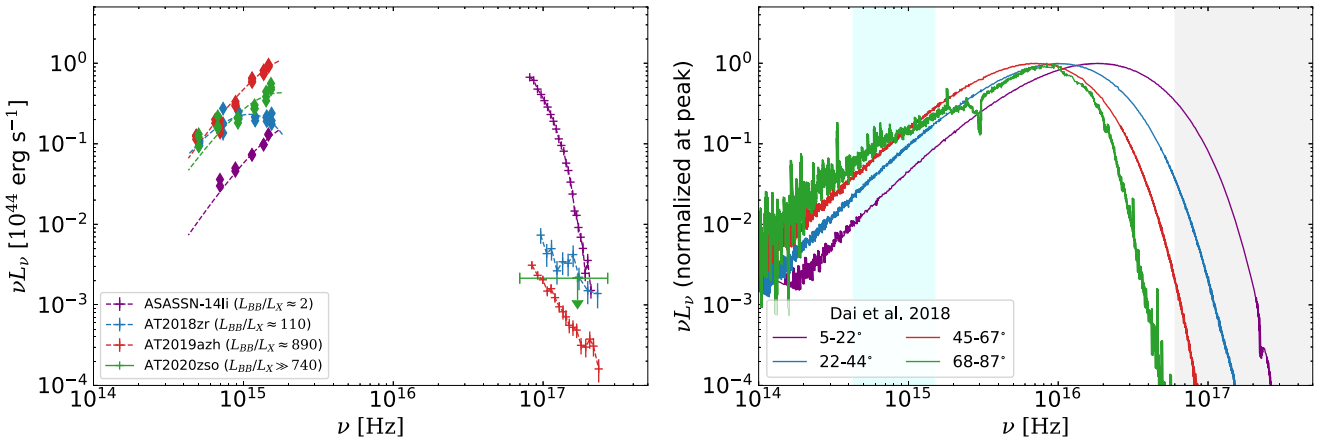

Figure 18. Comparison between observed SEDs and model SEDs by Dai et al. (2018). On the right, we show the early-time (near-UV/optical peak) observed SED for ASASSN14-li, AT 2018zr, and AT 2019azh (this work) as well as for AT 2020zso (Wevers et al. 2022), showing a large range of $L_{\rm BB}/L_{\rm X}$ values. The left panel shows Dai et al.'s (2018) early-time simulated SEDs as seen by distinct viewing angles from the disk pole: face-on = 0° and edge-on = 90°.

power-law decaying sources. Through largest inclination angles (toward edge-on), the system should be heavily optically thick ($\tau \gg 10$) to the X-rays which should be reprocessed to the lower energies, making the X-rays undetectable, and high lower limits on $L_{\rm BB}/L_{\rm X}$ to be measured. This should explain the TDE population with UV/optical emission only. When seen at intermediate angles, the system is not completely optically thick, but the optical depth is still important ($\tau \sim$ few), and only a small fraction of the X-rays can escape unreprocessed. The SED is then UV/optical-dominated ($L_{\rm BB}/L_{\rm X}$ between few $\times 10^1$ and few $\times 10^3$), but faint X-ray emission is still able to escape and be detected. As the accretion rate decreases, the optical depth of the system decreases, allowing for a larger fraction of the X-ray photons to escape, which would explain the *late-time brightening* sources (Thomsen et al. 2022) and perhaps the *X-ray-faint* sources given some fine-tuning in the evolution of the parameters.

In the left panel of Figure 18, we show four early-time SEDs with a diverse range of $L_{\rm BB}/L_{\rm X}$ values, while in the right panel, we show the four simulated SEDs for distinct inclination angles as presented by Dai et al. (2018). A direct comparison is, of course, not valid, given that in the Dai et al. (2018) models, the only parameter changed between the SEDs is the viewing angle toward the system; every other parameter of the system is fixed, while in reality, our four example sources/SEDs may have distinct black hole mass, black hole spin, impact parameter (β), peak disk temperature, radial profile of the disk temperature, and many other differences that could also shape the SED. However, it is interesting to note that the large diversity of $L_{\rm BB}/L_{\rm X}$ observed can, in principle, be produced just by a change in viewing angle.

This scenario seems to be able to explain several of the observed properties:

(i) the large range of $L_{\rm BB}/L_{\rm X}$ values at early times and the convergence to disklike values at late times;

(ii) the diversity of X-ray light curves, including the suppressed (but still detected) prompt X-ray emission from the *late-time brightening* and *X-ray-faint* sources; and

(iii) the lack of $M_{\rm BH}$ dependence on the presence/absence of luminous X-ray emission.

As we pointed out in Section 4.2, an important characteristic of the early suppression of the X-ray emission in the *late-time brightening* and *X-ray-faint* sources is that such suppression seems to have minimal effect on the measured T_p; given that the expected decline in temperature is still observed, T_p is the highest at early times and decays at late times. This would mean that although a large fraction of the X-rays are absorbed by this reprocessing layer of ionized gas,[19] the output spectrum seems to have a similar temperature (shape) as the supposed underlying emitted spectrum. This would require the absorption and reemission process to have a *"quasi-gray"* net effect in the X-ray 0.3–2.0 range. Such an effect is, however, quite hard to produce; for example, in Thomsen et al.'s (2022) simulations, the early-time output X-ray temperature can be up to ∼50% colder than the injected spectrum, depending on the viewing angle and the ionization state of the gas. This effect does not seem to be present—given the observed decline of T_p with time for all classes of sources—although the temperature of the underlying emission is, of course, not accessible for a direct comparison. Alternatively, if in these sources the absorbing material is heavily optically thick but clumpy or has small holes so that a fraction of the source X-rays can get through unprocessed, then this could explain the apparent suppression of the observed X-ray emission—given that the inferred disk radius would be reduced by a factor of the square root of the transmitted over emitted fluxes—while the emerging temperature would not be strongly modified (Takeuchi et al. 2013; Kobayashi et al. 2018; Yao et al. 2022). Independently of the driven mechanism, the X-ray-emitting structure (consistent with an accretion disk) is promptly formed even in those sources showing a late-time brightening, and their early-time emission seems to point toward a partial absorption/reprocessing scenario.

The *flaring* source, AT 2019ehz, has not been addressed yet. We first note that such short-term flaring differs from the gradual late-time X-ray increase of the *late-time brightening* sources; the reprocessing scenario does not work in this case, given that this system is bright at early times, fades, and then rebrightens, which would disagree with the net brightening predicted under the reprocessing scenario. Furthermore, the flaring behavior is accompanied by an increase in T_p, a relation

[19] Absorption by an ionized gas should not be confused with absorption by a neutral medium (modeled, e.g., by the `TBabs` in `xspec`); neutral absorption has a strong energy dependence in the soft X-rays, while (partially) ionized gas absorption, in contrast, has a higher optical depth in the hard X-rays (Thomsen et al. 2022).

between T_p and L_X is present (interestingly, with the highest best-fit α for an $L_X \propto T^{\alpha}$ relation), and no large variations in R_p are observed, with R_p/R_g always in the physically valid range. This behavior differs from the other sources with early X-ray-faint emission—as extensively discussed above—and instead points toward a disk seen directly without much reprocessing but with intrinsic variability.

One possibility is that X-ray variability is produced by random short-term fluctuations in the peak disk temperature (Mummery & Balbus 2022). Alternatively, the nascent accretion disk may be initially misaligned with respect to the MBH's spin axis, which would induce relativistic torques on the disk and cause it to precess (Lense–Thirring precession), producing repeating flares that should also modulate the observed T_p (Stone & Loeb 2012; Franchini et al. 2016; Pasham et al. 2024). In this scenario, relativistic torque effects align the disk and terminate precession and the flares; the flares are indeed not observed at late times in AT 2019ehz, although the cadence of observation is not enough to confirm this. In both cases, a short-term decoupling between the hotter (X-ray) and colder (UV/optical) emission regions, as observed, would be expected.

A definitive explanation for the flaring behavior of AT 2019ehz is not within the scope of this work, and it may not be possible at all, given the cadence/quality of the available data. A TDE discovered in 2022 (Yao & Gezari 2022) has shown similar flaring behavior; for that source, the cadence of the observations is much higher (several per day for hundreds of days), and distinct models for the flaring behavior will be tested in a forthcoming study (Y. Yao et al. 2024, in preparation).

5.2. On the Large Population of X-Ray-quiet TDEs

As we have shown in Section 4.5, most TDEs (up to 60%) discovered by optical surveys are X-ray-quiet ($L_X \leqslant 10^{42}$ erg s^{-1}); the definitive picture for why that is the case is beyond the scope of this paper. However, a couple of insights can be made.

First, TDEs with detectable X-ray emission but having $L_X \leqslant 10^{42}$ erg s^{-1} do exist, as we have demonstrated, and should be common given (i) the derived LF (see Section 4.6) and (ii) the possible orientation effects (see Section 5.1) that should cause a large fraction of X-ray emission to be absorbed.

However, such X-ray luminosities can hardly be observed unless the TDE happens at extremely low redshifts. Even a modest ∼20 ks XMM-Newton observation upper limit of $L_X \approx 10^{41}$ erg s^{-1} can rarely be placed for the typical redshift range in which TDEs are observed (see the L_X upper limits for the nondetected TDEs in Table 2). Sometimes these sources show a strong late-time X-ray rebrightening, but not always (e.g., AT 2018zr, AT 2018hyz, and AT 2019qiz); besides, if a TDE is not detected at early times—which for $L_X \leqslant 10^{42}$ erg s^{-1} only occurs for the nearest sources—it is unlikely that this source will continue to be followed up by an X-ray instrument, much less by XMM-Newton.

Furthermore, to be able to produce observable radiation in the 0.3–2 keV range from an accretion disk, the inner temperature (T_p) must necessarily be $\geqslant 10^{5.1}$–$10^{5.2}$ K, since at lower peak temperatures, the emission is shifted entirely to the EUV.

For a Galactic gas-to-dust ratio ($N_H = 5.5 \times 10^{21} \times E(B-V)$), soft X-rays are more absorbed than UV light. For instance, with $N_H = 5 \times 10^{20}$ cm^{-2} ($E(B-V) = 0.09$), about 74% of the 0.3 keV X-rays are absorbed, while only 42% of the 2600 Å UV light is. With higher absorption of $N_H = 1 \times 10^{21}$ cm^{-2} ($E(B-V) = 0.18$), 93% of the X-rays and 67% of the UV are absorbed.[20] Therefore, soft X-ray photons are more affected by absorption along our line of sight than UV photons, making them harder to detect given the same emitted flux. See, for example, the cases of AT 2021mhg, AT 2021sdu, and AT 2021yte in Section 4.5.

Finally, it is still possible that the circularization of the stellar debris does not happen, and no accretion disk is formed in these sources. In contrast, another process, independent of accretion, such as shocks produced by the intersection between the streams, would be responsible for all the UV/optical emission. Although it is not clear why the proposed lack of circularization is not dependent on M_{BH}, see Figure 16.

The combination of the effects mentioned above is likely to be able to explain the large fraction of optically discovered TDEs with no observable X-ray emission.

5.3. On the Bolometric Luminosity of TDEs

As pointed out by several authors (e.g., Dai et al. 2018; Lu & Kumar 2018; Thomsen et al. 2022; Mummery et al. 2023), a "missing energy" problem (Piran et al. 2015) will only arise when the integrated UV/optical (fitted with a blackbody function) is incorrectly considered as the bolometric luminosity of the TDE. This is an obvious statement for the sources with detected X-ray emission (see Figure 3) but should also be true for those in which X-ray emission is not detected, since the bulk of the TDE emission should be emitted in the EUV bands (see right panel of Figure 18), which is not adequately modeled by the single-temperature blackbody assumption for the UV/optical emission (see also right panel of Figure 5 in Dai et al. 2018).

When the full SED is consistent with a *bare/unreprocessed* accretion disk, i.e., the extrapolated disk model fitted from the X-rays matches the observed UV/optical (usually when $L_{BB}/L_X < 10$; see the ASASSN-14li and late-time AT 2019azh panel in Figure 15), the bolometric luminosity can be computed simply by integration over the disk SED.

We note, however, that if a *bare/unreprocessed* disk SED is assumed in cases where there is X-ray suppression, e.g., early times of AT 2019azh or AT 2018zr, where $L_{BB}/L_X \gg 100$, the resulting SED will be based on an unphysical normalization ($R_p/R_g \leqslant 0.3$) and hence will underestimate the true bolometric luminosity, even if considering the "disk bolometric luminosity."

For the cases—usually at early times—in which the strong UV/optical excess (i.e., $L_{BB}/L_X > 100$) is present (see again right panel of Figure 18), the SED shape is strongly dependent on the radiative processes involved and has large uncertainties because of the lack of constraints in the unobservable EUV wave band.

5.4. On the Unification of the TDE Population: Survey Selection Biases and the Lack of an Optical/X-Ray Dichotomy

As we have shown, optical surveys can discover TDEs with a large range of L_{BB}/L_X at early times; as we argue in Section 5.1, some (if not most) of this diversity can be

[20] For this calculation, a standard Wilms et al. (2000) abundance was assumed for the X-ray absorption using `TBabs`, while the UV extinction was based on Calzetti et al.'s (2000) law.

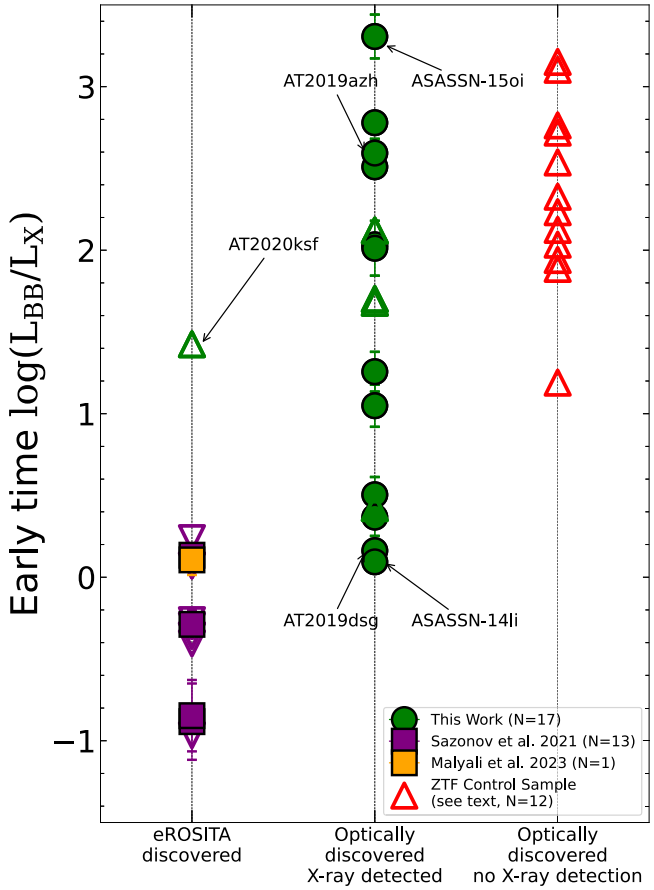

Figure 19. Distribution of early-time L_{BB}/L_X based on discovery wavelength/survey. Extreme sources are marked with arrows. Triangles are lower limits on L_{BB}/L_X (i.e., no X-ray detection), inverse triangles are an upper limit on L_{BB}/L_X (i.e., no UV/optical detection), and filled markers represent detections in both UV/optical and X-rays. Colors represent distinct samples or references. Sources with extreme values are marked with arrows. There is a continuous and wide distribution of L_{BB}/L_X values, instead of a clear dichotomy between optically and X-ray-discovered TDEs.

explained by the viewing angle toward the system. We would like to compare the TDEs discovered by optical surveys and by X-ray surveys to look for differences (or lack thereof) in these populations and, if present, what could drive such differences.

TDEs discovered by most X-ray missions (e.g., ROSAT and XMM-Newton Slew Survey) had very little to no real-time UV/optical follow-up; hence, accessing their L_{BB}/L_X ratio is not possible. We thus focused our analyses on the more recent sources discovered by SRG/eROSITA, particularly the 13 TDEs presented in Sazonov et al. (2021) and eRASSt J074426.3+291606 (hereafter J0744) presented by Malyali et al. (2023). Unfortunately, the sources presented in Sazonov et al. (2021) had no UV follow-up, but some constraints on the optical emission from ground-based optical time-domain surveys were obtained.

As reported by Sazonov et al. (2021), all of their sources had L_g/L_X[21] ratios lower than 0.3. For a typical UV/optical temperature of 20,000 K (Hammerstein et al. 2023a), this translates into $L_{BB}/L_X \leqslant 3$. Such values, however, do not mean that these sources were *"X-ray only."* For example, the early-time L_{BB}/L_X of ASASSN-14li and AT 2019dsg were also lower than 3. This is also true for J0744, which had $L_{BB}/L_X \approx 2$ at early times. Most of the sources in Sazonov et al. (2021) had no optical counterpart detection; given the relatively high redshift range of their sample (all but one have $z > 0.1$, compared with our sample in Table 1), ground-based optical surveys are not sensitive enough to detect the typical optical TDE luminosities at these redshifts. For the sources with detected optical counterparts, the range of L_{BB}/L_X was $\sim 0.1 \leqslant L_{BB}/L_X \leqslant 2$. As discussed in Section 5.1, for these values of L_{BB}/L_X, no UV/optical excess is necessarily present. The shape of the SED is fully consistent with a *bare/unreprocessed* accretion disk; hence, these systems are likely to be seen at lower angles (i.e., toward face-on orientations), similar to ASASSN-14li and AT 2019dsg. The small variations observed in L_{BB}/L_X can be fully explained by a range of values of T_p that, as shown in Appendix B, can produce L_{BB}/L_X as low as ~ 0.05 for the range of T_p found in TDEs.

The distribution of L_{BB}/L_X at early times for sources discovered by distinct methods/surveys is presented in Figure 19. Triangles are lower limits on L_{BB}/L_X (i.e., no X-ray detection), inverse triangles are an upper limit on L_{BB}/L_X (i.e., no UV/optical detection), and filled markers represent detections in both UV/optical and X-rays. In Figure 20, we show the peak L_{BB} versus the early-time L_X, where the distinct symbols show SRG/eROSITA TDEs (squares), optically selected X-ray-detected (circles), and optically selected with no X-ray detection (diamonds); filled markers show detection in both optical/UV (y-axis) and X-ray (x-axis), while the hollow markers show sources in which either UV/optical or X-rays were not detected (at early times); similarly to Figure 19, distinct colors represent the different references.

From Figure 19, it is clear that there is no obvious dichotomy between optical and X-ray-discovered TDEs. Instead, there is a continuous distribution of L_{BB}/L_X values at early times that is at least as wide as $L_{BB}/L_X \in (0.1, 32{,}000)$. This can be explained by the fact that surveys at distinct wavelengths will be biased to discover sources that are brightest in that wavelength range. Optical surveys will discover mostly sources with high L_{BB}/L_X, up to 60% of which have $L_X \leqslant 10^{42}$ erg s^{-1} (see Section 4.5), but will still sometimes discover sources with lower L_{BB}/L_X, such as ASASSN-14li and AT 2019dsg. X-ray surveys, on the other hand, will most likely discover sources with lower L_{BB}/L_X, but not always; AT 202ksf, for example, had no X-ray detection at early times ($L_{BB}/L_X \geqslant 25$), was not identified in real time as a TDE candidate by optical surveys, and was later ($\Delta t \sim 200$ days) discovered by SRG/eROSITA following its X-ray brightening. The same holds for their distribution in the $L_{BB} \times L_X$ plane of Figure 20; there is a continuous distribution of the X-ray and UV/optical selected populations instead of a clear dichotomy between them.

An *unbiased*[22] discovery of TDEs would be possible with either (i) the simultaneous operation of a wide field-of-view (FoV) X-ray survey telescope with UV follow-up capabilities (e.g., STAR-X; Hornschemeier et al. 2023) and a wide FoV optical survey (e.g., LSST; Ivezić et al. 2019) or (ii) the simultaneous and coordinated operation of a wide FoV UV survey telescope (e.g., ULTRASAT and/or UVEX; Sagiv et al. 2014; Kulkarni et al. 2021) and a wide FoV X-ray survey

[21] Where L_g is the optical g-band luminosity.

[22] This is still biased toward dust-free host galaxies. For heavily dust-obscured TDEs, the UV/optical and soft X-rays are absorbed and reemitted in the infrared; see, for example, Panagiotou et al. (2023) and Masterson et al. (2024).

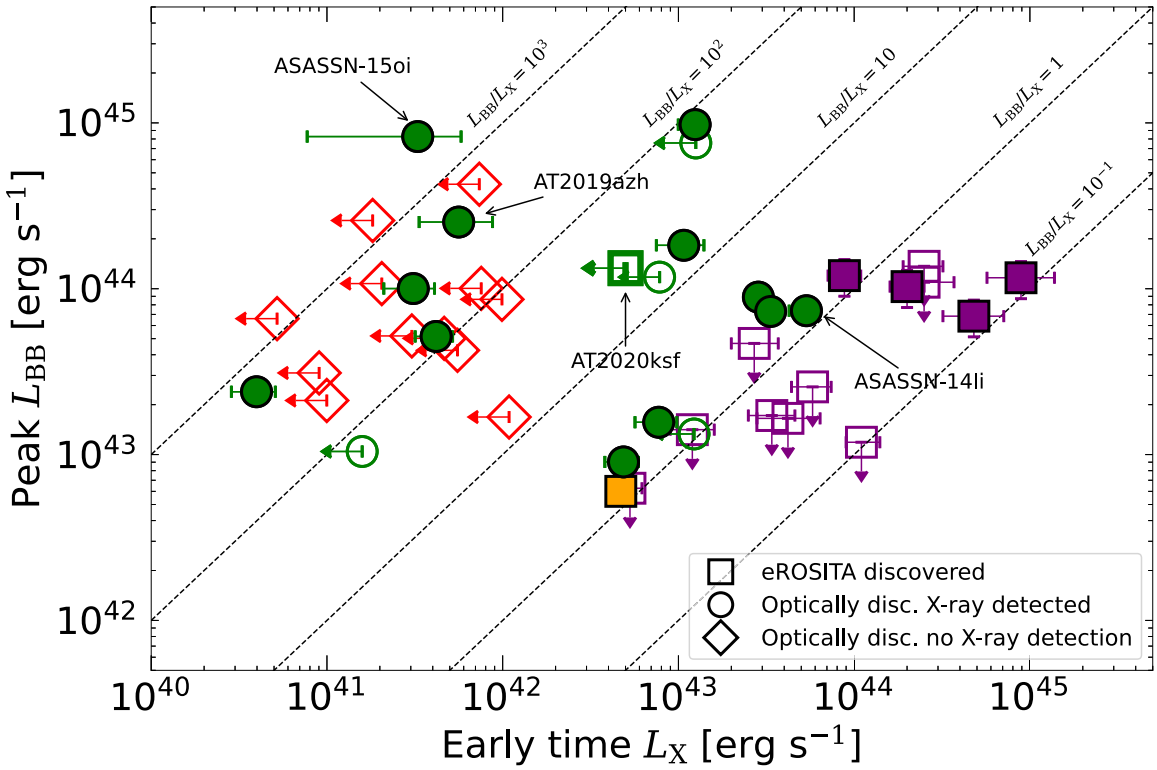

Figure 20. Distribution of peak L_{BB} × early-time L_X for different TDE populations. Squares show SRG/eROSITA (X-ray) discovered sources, circles show optically discovered X-ray-detected, while diamonds show optically discovered with no X-ray detection. Filled markers represent detections in both UV/optical and X-rays (early times), while open symbols represent upper limits in one of the two wavelength bands, where the arrows represent their 3σ upper limit. The colors are the same as in Figure 19.

telescope (e.g., SRG/eROSITA and/or Einstein Probe; Sunyaev et al. 2021; Yuan et al. 2022).

6. Conclusions

We have analyzed the XMM-Newton and Neil Gehrels Swift Observatory X-ray and broadband UV/optical emission of 17 optically selected X-ray-detected TDEs discovered between 2014 and 2021 December; we also compare our sample with the samples of optically discovered X-ray-quiet TDEs and X-ray-discovered TDEs. Our main conclusions are as follows.

1. The X-ray light curves show a large diversity, with sources rarely showing a power-law decay and a large fraction showing a late-time brightening.
2. The X-ray spectra are extremely soft in most sources and epochs, easily distinguishable from AGN X-ray spectra.
3. The overall behavior of the measured radius (normalization) and temperature (shape) resulting from the X-ray spectral fitting is in agreement with that expected for the innermost region of a newly formed and time-evolving accretion disk, including the cooling of the peak temperature and a radius (in most cases) consistent with the innermost stable orbit.
4. Sources with early-time faint X-ray emission show an unphysical radius for the X-ray emission at these epochs, while their temperature behaves as expected, indicating the apparent suppression/absorption of their intrinsic early X-ray emission.
5. The SED shape, as probed by the ratio (L_{BB}/L_X) between the UV/optical and X-ray luminosities, has a large range of values $L_{BB}/L_X \in (0.5, 3000)$ at early times; at late times, the range converges to disklike values, $L_{BB}/L_X \in (0.5, 10)$, for all sources.
6. The combined X-ray spectral and SED properties and evolution favors a change in the optical depth (thick → thin) for the high-energy photons through the line of sight, instead of the delayed formation of the accretion disk, in order to explain the late-time brightening observed in some sources.
7. Three sources show a soft → hard X-ray spectral transition, indicative of the formation of a hot corona akin to active galaxies, with the state transitions occurring at least 200 days after the UV/optical peak, but it is not sustained for more than a couple of months.
8. We estimated that the fraction of optically discovered TDEs that are X-ray-loud, with $L_X \geqslant 10^{42}$ erg s^{-1}, is at least 40% and that X-ray loudness is not dependent on M_{BH}.
9. We show that the TDE X-ray LF from 10^{41} to 10^{45} erg s^{-1} has a broken power-law shape in the form of $dN/dL_X \propto L_X^{-1.0\pm0.2}$ at $L_X < L_{bk}$ and $dN/dL_X \propto L_X^{-2.7\pm1.0}$ at $L_X \geqslant L_{bk}$ with a break luminosity of $\log(L_{bk}) = 44.1^{+0.3}_{-0.5}$ erg s^{-1}, revealing a large population of TDEs with $L_X \leqslant 10^{42}$ erg s^{-1} (and high L_{BB}/L_X) for which the X-ray emission cannot be detected with current instruments unless it occurs at very low z.
10. We show that there is no dichotomy between optical and X-ray-discovered TDEs. Instead, there is a continuous range of early-time L_{BB}/L_X, at least as wide as $L_{BB}/L_X \in (0.1, 3000)$, with X-ray/optical surveys discovering preferentially, but not exclusively, from the lower/higher

portion of the distribution, in agreement with unification models for the overall TDE population.

Acknowledgments

M.G. thanks T. Wevers, J. Krolik, P. Jonker, and E. Coughlin for comments, suggestions, and discussions. M.G. and S.G. are supported in part by NASA XMM-Newton grants 80NSS23K0621 and 80NSSC22K0571. Y.Y. acknowledges support by NASA XMM-Newton grant 80NSSC23K0482. E. H. acknowledges support by NASA under award No. 80GSFC21M0002. This work is based on observations obtained with the Samuel Oschin Telescope 48 inch and the 60 inch telescope at the Palomar Observatory as part of the Zwicky Transient Facility project. ZTF is supported by the National Science Foundation under grant No. AST-2034437 and a collaboration including Caltech, IPAC, the Weizmann Institute of Science, the Oskar Klein Center at Stockholm University, the University of Maryland, Deutsches Elektronen-Synchrotron and Humboldt University, the TANGO Consortium of Taiwan, the University of Wisconsin at Milwaukee, Trinity College Dublin, Lawrence Livermore National Laboratories, IN2P3, the University of Warwick, Ruhr University Bochum, and Northwestern University. Operations are conducted by COO, IPAC, and UW. The ZTF forced-photometry service was funded under Heising-Simons Foundation grant No. 12540303 (PI: Graham). This work has made use of data from the Asteroid Terrestrial-impact Last Alert System (ATLAS) project. The ATLAS project is primarily funded to search for near-Earth asteroids through NASA grants NN12AR55G, 80NSSC18K0284, and 80NSSC18K1575. This work made use of data supplied by the UK Swift Science Data Centre at the University of Leicester.

Facilities: XMM, Swift, eROSITA, PO:1.2 m, OGLE.

Software: `astropy` (Astropy Collaboration et al. 2013), `emcee` (Foreman-Mackey et al. 2013), `heasoft` (Heasarc 2014), `matplotlib` (Hunter 2007), `Prospector` (Johnson et al. 2021), `scipy` (Virtanen et al. 2020), `xspec` (Arnaud 1996).

Appendix A
Modeling of Corona Emission in TDEs with `simPL`

In the study of AGN, the corona is the primary X-ray emitter, while the cold accretion disks mainly emit in the UV bands. AGN X-ray spectra are often described using the `powerlaw` model, despite some attempts to develop more comprehensive models like `Optxagnf` (Done et al. 2012); these face challenges due to numerous parameters and degeneracies. Therefore, the `powerlaw` model remains prevalent in AGN X-ray literature.

In XRBs, the accretion disks are hotter and emit mainly in the X-ray bands. In the soft state of XRBs, the accretion disk dominates the X-ray emission, but as they transition to the hard state, an emergent corona with a power-law spectrum becomes dominant. The `powerlaw` model is widely used in XRB modeling but suffers from the drawback of rising infinitely at low energies, which is inconsistent with Comptonization.

To overcome the limitation of the `powerlaw` model in accurately describing Comptonization, Steiner et al. (2009) introduced `simPL`, a flexible convolution model for fitting X-ray spectra of XRBs. `simPL` captures Comptonization

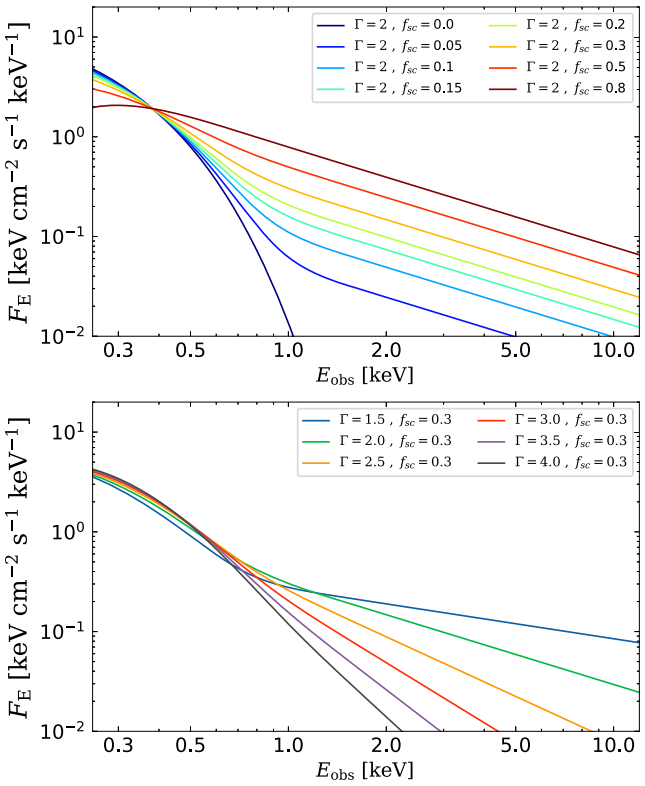

Figure 21. Simulation of `simPL` model spectra. Upper panel: fixed power-law index (Γ_{sc}) varying fraction of upscattered photons (f_{sc}). Bottom panel: fixed f_{sc} varying Γ_{sc}.

effects using any seed photon spectrum and shares parameters such as the photon index (Γ) with the `powerlaw` model. However, it employs the scattered fraction (f_{sc}) as the normalization factor instead of photon flux, simplifying the model by omitting specific details of the Comptonizing medium while maintaining a physically consistent approach. Unlike the `powerlaw` model, `simPL` directly links the power-law component to the input photon energy distribution, resulting in a power-law tail at higher energies without extending indefinitely to lower energies. This behavior aligns with Compton-scattering expectations and is commonly observed in physical Comptonization models. Notably, in the soft X-ray bands, `simPL` exhibits a natural cutoff consistent with Comptonization, whereas the `powerlaw` model continues to rise without limit (Yao et al. 2005).

Similarly to XRBs, TDEs also have a portion of their continuum disk emission in the X-ray. Therefore, a similar approach can be applied to model the X-ray spectra of TDEs. Figure 21 demonstrates the effects of using `simPL` through a series of simulations where a thermal model with $T_p \approx 70$ eV and $R_p \approx 10^{12}$ cm is convoluted with `simPL` using different values of f_{sc} (top panel) and Γ (bottom panel). With $f_{sc} = 0$, there is no corona emission, and the resulting model corresponds to the input disk spectrum. As f_{sc} increases from 0.05, the spectrum remains dominated by the disk but with a faint hard excess. In the range $0.5 \leqslant f_{sc} \leqslant 0.20$, the source enters an intermediate state, where the thermal and nonthermal spectra have similar fluxes. When $f_{sc} \approx 0.3$, the total spectrum becomes almost indistinguishable from a pure power law, and the spectrum remains consistent with a power law for higher values.

An important question for our X-ray spectral analyses (Sections 3 and 4.2) is up to what corona strength (as probed by f_{sc}) the

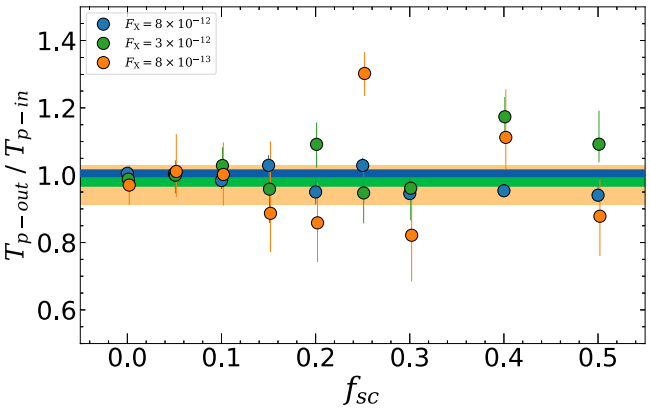

Figure 22. Simulation of the measurement of the underlying disk properties in the presence of corona Comptonization. The y-axis shows the ratio between the input and output T_p as a function of the corona strength (f_{sc}). The color shows distinct fluxes of the mock spectra, and the shaded regions show the uncertainty in the $f_{sc} = 0$ spectra, i.e., the uncertainty from the instrumental S/N.

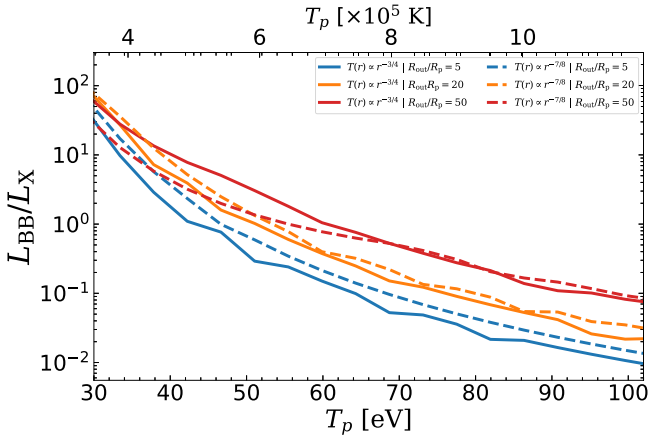

Figure 23. Simulation of the expected UV/optical-to-X-ray luminosity ratio (L_{BB}/L_X) for the standard disk. The y-axis shows the expected L_{BB}/L_X from a *bare/unreprocessed* accretion disk with two distinct temperature profiles (solid and dashed lines) as a function of the peak temperature of the disk (T_p).

underlying thermal continuum can be recovered from the fitting. To answer this question, we simulate mock X-ray spectra using the `fakeit` command in `xspec` for a stacked 30 ks observation with Swift/XRT, assuming `simPL⊗tdediscspec`, a random T_p in the range observed in our sample, three flux ($F_X = 8 \times 10^{-12}$, 3×10^{-12}, and 8×10^{-13} erg cm^{-2} s^{-1}) levels, and varying f_{sc} between 0.0 (no corona) and 0.5. We then fit the mock spectra with the same model in order to measure the best-fit T_p and compare with the input value. Figure 22 summarizes our findings. The underlying (input) temperature can be recovered (within the error bar) considering the uncertainties related to the S/N of the instrument (shaded regions) up to $f_{sc} \approx 0.2$; at higher values, the underlying information on the temperature of the disk is lost by the emergence of the corona in the higher energies of the disk spectrum and cannot be uniquely recovered.

Appendix B
Simulation of Expected L_{BB}/L_X for a Standard Disk

An important observational probe of TDE emission is the ratio L_{BB}/L_X between the UV/optical luminosity (as fitted by a BB) and the 0.3–10 keV X-ray luminosity. Although additional emission processes should be involved, the formation of an accretion disk is a natural prediction of a TDE. In this section, we aim to probe the range of L_{BB}/L_X that can be produced by a *bare/unreprocessed* accretion disk, given the range of inner peak temperatures (T_p) we observe from the X-ray fitting. To obtain that we simulate the accretion disk with varying T_p in the range $5.5\text{K} \leqslant \log T_p \leqslant 6.1$ K, we test two distinct disk solutions for the temperature profile of the disk: the standard vanishing ISCO stress solution (Shakura & Sunyaev 1973; Makishima et al. 1986), $T(R) \propto R^{-3/4}$, and the finite ISCO stress (Agol & Krolik 2000), $T(R) \propto R^{-7/8}$. We also explore a distinct disk outer radius from $R_{out}/R_p \in (5, 50)$. We pass the synthetic SED into the sensibility curve of the six UVOT and two ZTF filters and fit the resulting broadband UV/optical with a blackbody to obtain L_{BB}, the same way it was done in the observed data (see Figure 3 for illustration). The ratio L_{BB}/L_X as a function of T_p for the two distinct disk solutions is shown in Figure 23. For the entire range, L_{BB}/L_X is between 5×10^{-2} and a maximum of $\sim$70. At late times, most of our sample shows disk cooling, and all TDE have $\log T_p \leqslant 5.8$; this limits L_{BB}/L_X to values >0.3 but rarely higher than 10, which is in agreement with our findings in Figure 14.

Appendix C
The BASS AGN Sample

The Swift/BAT 70 month AGN catalog consists of 858 nearby ($z \lesssim 0.3$ for unbeamed) AGN (Koss et al. 2022), and, using soft X-ray observations by XMM-Newton, Swift, ASCA, Chandra, and Suzaku, their broadband X-ray spectra were characterized and presented by Ricci et al. (2017). Some of the properties they constrain are the intrinsic X-ray luminosity (in the 2–10, 20–50, and 14-150 keV bands), the line-of-sight column density of obscuring material (N_H), the slope of the X-ray power-law continuum, and the temperature of the thermal plasma for obscured sources. The many phenomenological models used are broadly classified into four groups: unobscured (352), obscured (386), blazars (97), and other non-AGN models (2). The remaining details of the X-ray modeling of the BASS sample can be found in Ricci et al. (2017).

From among these sources, we selected those that were either obscured or unobscured (which excludes beamed and non-AGN sources) and that had spectroscopic redshift measurements from optical counterparts. This resulted in 617 sources. To calculate the HR, the X-ray spectra were simulated from the models using `XSPEC`, and the count rate was recorded for the soft (0.3–2.0 keV) and hard (2.0–10.0 keV) bands. Spectra were measured with a long response time (1 Ms) to minimize the effects of statistical noise on the HR. This was done twice: with the response files for Swift/XRT photon counting grades 0–12 and XMM-Newton EPIC pn. We also measured the 0.3–10.0 keV intrinsic luminosities by setting all N_H parameters of all model components to 0 (or, in certain cases, the minimum nonzero value allowed by the model) and using the `calcLumin` command.

Appendix D
Model Comparison

In Figure 24, we compare the distribution of the ratio of the statistics (χ^2 for XMM-Newton and "C-statistics," Cash 1979, for Swift/XRT) over dof for all spectra with a negligible "hard excess" (i.e., $f_{scsc} \sim 0.0$) for both `tdediscspec` and

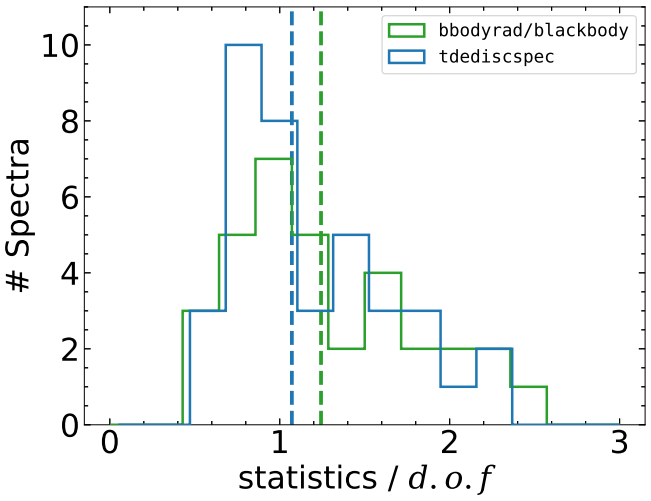

Figure 24. Distribution of the ratio of the statistics (χ^2 for XMM-Newton and "C-statistics," Cash 1979, for Swift/XRT) over dof for spectra with a negligible "hard excess" (i.e., $f_{sc} \sim 0.0$) for `tdediscspec` and blackbody, xspec models. Dashed lines show the median values for the models.

`blackbody`, `xspec` models. The mean ratio is lower `tdediscspec`.

ORCID iDs

Muryel Guolo https://orcid.org/0000-0002-5063-0751
Suvi Gezari https://orcid.org/0000-0003-3703-5154
Yuhan Yao https://orcid.org/0000-0001-6747-8509
Sjoert van Velzen https://orcid.org/0000-0002-3859-8074
Erica Hammerstein https://orcid.org/0000-0002-5698-8703
S. Bradley Cenko https://orcid.org/0000-0003-1673-970X
Yarone M. Tokayer https://orcid.org/0000-0002-0430-5798

References

Agol, E., & Krolik, J. H. 2000, ApJ, 528, 161
Alexander, K. D., Berger, E., Guillochon, J., Zauderer, B. A., & Williams, P. K. G. 2016, ApJL, 819, L25
Arnaud, K. A. 1996, in ASP Conf. Ser. 101, Astronomical Data Analysis Software and Systems V, ed. G. H. Jacoby & J. Barnes (San Francisco, CA: ASP), 17
Astropy Collaboration, Robitaille, T. P., Tollerud, E. J., et al. 2013, A&A, 558, A33
Bade, N., Komossa, S., & Dahlem, M. 1996, A&A, 309, L35
Balbus, S. A., & Hawley, J. F. 1991, ApJ, 376, 214
Blagorodnova, N., Cenko, S. B., Kulkarni, S. R., et al. 2019, ApJ, 873, 92
Blagorodnova, N., Gezari, S., Hung, T., et al. 2017, ApJ, 844, 46
Blagorodnova, N., Neill, J. D., Walters, R., et al. 2018, PASP, 130, 035003
Bonnerot, C., Rossi, E. M., Lodato, G., & Price, D. J. 2016, MNRAS, 455, 2253
Bonnerot, C., Rossi, E. M., & Lodato, G. 2017, MNRAS, 464, 2816
Bright, J. S., Fender, R. P., Motta, S. E., et al. 2018, MNRAS, 475, 4011
Brown, G. C., Levan, A. J., Stanway, E. R., et al. 2017, MNRAS, 472, 4469
Burrows, D. N., Hill, J. E., Nousek, J. A., et al. 2005, SSRv, 120, 165
Calzetti, D., Armus, L., Bohlin, R. C., et al. 2000, ApJ, 533, 682
Cannizzaro, G., Wevers, T., Jonker, P. G., et al. 2021, MNRAS, 504, 792
Cannizzo, J. K., Lee, H. M., & Goodman, J. 1990, ApJ, 351, 38
Cash, W. 1979, ApJ, 228, 939
Cenko, S. B., Cucchiara, A., Roth, N., et al. 2016, ApJL, 818, L32
Cenko, S. B., Krimm, H. A., Horesh, A., et al. 2012, ApJ, 753, 77
Chornock, R., Berger, E., Gezari, S., et al. 2014, ApJ, 780, 44
Conroy, C., Gunn, J. E., & White, M. 2009, ApJ, 699, 486
Coughlin, E. R., & Begelman, M. C. 2014, ApJ, 781, 82
Dai, L., McKinney, J. C., Roth, N., Ramirez-Ruiz, E., & Miller, M. C. 2018, ApJL, 859, L20
Done, C., Davis, S. W., Jin, C., Blaes, O., & Ward, M. 2012, MNRAS, 420, 1848
Evans, P. A., Beardmore, A. P., Page, K. L., et al. 2007, A&A, 469, 379
Evans, P. A., Beardmore, A. P., Page, K. L., et al. 2009, MNRAS, 397, 1177
Fabian, A. C., Zoghbi, A., Ross, R. R., et al. 2009, Natur, 459, 540
Foreman-Mackey, D., Hogg, D. W., Lang, D., & Goodman, J. 2013, PASP, 125, 306
Franchini, A., Lodato, G., & Facchini, S. 2016, MNRAS, 455, 1946
French, K. D., Wevers, T., Law-Smith, J., Graur, O., & Zabludoff, A. I. 2020, SSRv, 216, 32
Gabriel, C., Denby, M., Fyfe, D. J., et al. 2004, in ASP Conf. Ser. 314, Astronomical Data Analysis Software and Systems (ADASS) XIII, ed. F. Ochsenbein, M. G. Allen, & D. Egret (San Francisco, CA: ASP), 759
Gehrels, N. 1986, ApJ, 303, 336
Gehrels, N., Chincarini, G., Giommi, P., et al. 2004, ApJ, 611, 1005
Gezari, S. 2021, ARA&A, 59, 21
Gezari, S., Cenko, S. B., & Arcavi, I. 2017, ApJL, 851, L47
Gezari, S., Chornock, R., Rest, A., et al. 2012, Natur, 485, 217
Gilfanov, M., Sazonov, S., Sunyaev, R., et al. 2020, ATel, 14246, 1
Greiner, J., Schwarz, R., Zharikov, S., & Orio, M. 2000, A&A, 362, L25
Grupe, D., Thomas, H. C., & Leighly, K. M. 1999, A&A, 350, L31
Guillochon, J., Manukian, H., & Ramirez-Ruiz, E. 2014, ApJ, 783, 23
Gültekin, K., King, A. L., Cackett, E. M., et al. 2019, ApJ, 871, 80
Haardt, F., & Maraschi, L. 1991, ApJL, 380, L51
Hammerstein, E., van Velzen, S., Gezari, S., et al. 2023a, ApJ, 942, 9
Hammerstein, E., Cenko, S. B., Gezari, S., et al. 2023b, ApJ, 957, 86
Heasarc, 2014 HEAsoft: Unified Release of FTOOLS and XANADU, Astrophysics Source Code Library, ascl:1408.004
HI4PI Collaboration, Ben Bekhti, N., & Flöer, L. 2016, A&A, 594, A116
Hills, J. G. 1975, Natur, 254, 295
Holoien, T. W. S., Huber, M. E., Shappee, B. J., et al. 2019, ApJ, 880, 120
Holoien, T. W. S., Kochanek, C. S., Prieto, J. L., et al. 2016a, MNRAS, 455, 2918
Holoien, T. W. S., Kochanek, C. S., Prieto, J. L., et al. 2016b, MNRAS, 463, 3813
Holoien, T. W. S., Prieto, J. L., Bersier, D., et al. 2014, MNRAS, 445, 3263
Hornschemeier, A., Zhang, W., STAR-X Team, Kara, E. 2023, AAS Meeting, 55, 120.05
Hung, T., Gezari, S., Blagorodnova, N., et al. 2017, ApJ, 842, 29
Hunter, J. D. 2007, CSE, 9, 90
Jiang, Y.-F., Guillochon, J., & Loeb, A. 2016, ApJ, 830, 125
Johnson, B. D., Leja, J., Conroy, C., & Speagle, J. S. 2021, ApJS, 254, 22
Jonker, P. G., Stone, N. C., Generozov, A., van Velzen, S., & Metzger, B. 2020, ApJ, 889, 166
Ivezić, Ž., Kahn, S. M., Tyson, J. A., et al. 2019, ApJ, 873, 111
Kajava, J. J. E., Giustini, M., Saxton, R. D., & Miniutti, G. 2020, A&A, 639, A100
Kara, E., Dai, L., Reynolds, C. S., & Kallman, T. 2018, MNRAS, 474, 3593
Kobayashi, H., Ohsuga, K., Takahashi, H. R., et al. 2018, PASJ, 70, 22
Komossa, S., & Greiner, J. 1999, A&A, 349, L45
Kosec, P., Pasham, D., Kara, E., & Tombesi, F. 2023, ApJ, 954, 170
Koss, M. J., Ricci, C., Trakhtenbrot, B., et al. 2022, ApJS, 261, 2
Krolik, J., Piran, T., Svirski, G., & Cheng, R. M. 2016, ApJ, 827, 127
Kulkarni, S. R., Harrison, F. A., Grefenstette, B. W., et al. 2021, arXiv:2111.15608
Lin, D., Maksym, P. W., Irwin, J. A., et al. 2015, ApJ, 811, 43
Liu, X.-L., Dou, L.-M., Chen, J.-H., & Shen, R.-F. 2022, ApJ, 925, 67
Lodato, G., & Rossi, E. M. 2011, MNRAS, 410, 359
Loeb, A., & Ulmer, A. 1997, ApJ, 489, 573
Lu, W., & Kumar, P. 2018, ApJ, 865, 128
Madsen, K., Hickox, R., Bachetti, M., et al. 2019, BAAS, 51, 166
Mainzer, A., Bauer, J., Cutri, R. M., et al. 2014, ApJ, 792, 30
Makishima, K., Maejima, Y., Mitsuda, K., et al. 1986, ApJ, 308, 635
Malyali, A., Liu, Z., Merloni, A., et al. 2023, MNRAS, 520, 4209
Masci, F. J., Laher, R. R., Rusholme, B., et al. 2019, PASP, 131, 018003
Masci, F. J., Laher, R. R., Rusholme, B., et al. 2023, arXiv:2305.16279
Masterson, M., De, K., Panagiotou, C., et al. 2024, ApJ, 961, 211
Metzger, B. D. 2022, ApJL, 937, L12
Metzger, B. D., & Stone, N. C. 2016, MNRAS, 461, 948
Miller, J. M., Kaastra, J. S., Miller, M. C., et al. 2015, Natur, 526, 542
Miller, K. A., & Stone, J. M. 2000, ApJ, 534, 398
Mitsuda, K., Inoue, H., Koyama, K., et al. 1984, PASJ, 36, 741
Mummery, A. 2021, MNRAS, 507, L24
Mummery, A., & Balbus, S. 2022, MNRAS, 517, 3423
Mummery, A., & Balbus, S. A. 2020, MNRAS, 492, 5655
Mummery, A., & Balbus, S. A. 2021, MNRAS, 505, 1629
Mummery, A., Wevers, T., Saxton, R., & Pasham, D. 2023, MNRAS, 519, 5828
Nicholl, M., Wevers, T., Oates, S. R., et al. 2020, MNRAS, 499, 482

Panagiotou, C., De, K., Masterson, M., et al. 2023, ApJL, 948, L5
Parkinson, E. J., Knigge, C., Matthews, J. H., et al. 2022, MNRAS, 510, 5426
Pasham, D. R., Cenko, S. B., Levan, A. J., et al. 2015, ApJ, 805, 68
Pasham, D. R., Lucchini, M., Laskar, T., et al. 2023, NatAs, 7, 88
Pasham, D. R., Zajacek, M., Nixon, C. J., et al. 2024, arXiv:2402.09689
Piran, T., Svirski, G., Krolik, J., Cheng, R. M., & Shiokawa, H. 2015, ApJ, 806, 164
Predehl, P., Andritschke, R., Arefiev, V., et al. 2021, A&A, 647, A1
Quintin, E., Webb, N. A., Guillot, S., et al. 2023, A&A, 675, A152
Rees, M. J. 1988, Natur, 333, 523
Remillard, R. A., & McClintock, J. E. 2006, ARA&A, 44, 49
Ricci, C., Kara, E., Loewenstein, M., et al. 2020, ApJL, 898, L1
Ricci, C., Trakhtenbrot, B., Koss, M. J., et al. 2017, ApJS, 233, 17
Roming, P. W. A., Kennedy, T. E., Mason, K. O., et al. 2005, SSRv, 120, 95
Roth, N., Kasen, D., Guillochon, J., & Ramirez-Ruiz, E. 2016, ApJ, 827, 3
Sagiv, I., Gal-Yam, A., Ofek, E. O., et al. 2014, AJ, 147, 79
Saxton, R., Komossa, S., Auchettl, K., & Jonker, P. G. 2020, SSRv, 216, 85
Saxton, R. D., Read, A. M., Komossa, S., et al. 2017, A&A, 598, A29
Sazonov, S., Gilfanov, M., Medvedev, P., et al. 2021, MNRAS, 508, 3820
Schlafly, E. F., & Finkbeiner, D. P. 2011, ApJ, 737, 103
Schmidt, M. 1968, ApJ, 151, 393
Schnittman, J. D., Krolik, J. H., & Noble, S. C. 2016, ApJ, 819, 48
Shakura, N. I., & Sunyaev, R. A. 1973, A&A, 24, 337
Shiokawa, H., Krolik, J. H., Cheng, R. M., Piran, T., & Noble, S. C. 2015, ApJ, 804, 85
Short, P., Nicholl, M., Lawrence, A., et al. 2020, MNRAS, 498, 4119
Stein, R., Velzen, S. v., Kowalski, M., et al. 2021, NatAs, 5, 510
Steiner, J. F., Narayan, R., McClintock, J. E., & Ebisawa, K. 2009, PASP, 121, 1279
Stern, D., Assef, R. J., Benford, D. J., et al. 2012, ApJ, 753, 30
Stone, N., & Loeb, A. 2012, PhRvL, 108, 061302
Strüder, L., Briel, U., Dennerl, K., et al. 2001, A&A, 365, L18
Sunyaev, R., Arefiev, V., Babyshkin, V., et al. 2021, A&A, 656, A132
Takeuchi, S., Ohsuga, K., & Mineshige, S. 2013, PASJ, 65, 88
Thomsen, L. L., Kwan, T. M., Dai, L., et al. 2022, ApJL, 937, L28
Titarchuk, L., & Lyubarskij, Y. 1995, ApJ, 450, 876
Tonry, J. L., Denneau, L., Heinze, A. N., et al. 2018, PASP, 130, 064505
Trakhtenbrot, B., Arcavi, I., MacLeod, C. L., et al. 2019, ApJ, 883, 94
Udalski, A., Szymański, M. K., & Szymański, G. 2015, AcA, 65, 1
Ulmer, A. 1999, ApJ, 514, 180
van Velzen, S. 2018, ApJ, 852, 72
van Velzen, S., Gezari, S., Cenko, S. B., et al. 2019, ApJ, 872, 198
van Velzen, S., Gezari, S., Hammerstein, E., et al. 2021, ApJ, 908, 4
Virtanen, P., Gommers, R., Oliphant, T. E., et al. 2020, NatMe, 17, 261
Wang, J., Kara, E., Lucchini, M., et al. 2022, ApJ, 930, 18
Wen, S., Jonker, P. G., Stone, N. C., Zabludoff, A. I., & Psaltis, D. 2020, ApJ, 897, 80
Wevers, T. 2020, MNRAS, 497, L1
Wevers, T., Nicholl, M., Guolo, M., et al. 2022, A&A, 666, A6
Wevers, T., Pasham, D. R., van Velzen, S., et al. 2019a, MNRAS, 488, 4816
Wevers, T., Stone, N. C., van Velzen, S., et al. 2019b, MNRAS, 487, 4136
Wevers, T., Pasham, D. R., van Velzen, S., et al. 2021, ApJ, 912, 151
Wilms, J., Allen, A., & McCray, R. 2000, ApJ, 542, 914
Wyrzykowski, Ł, Zieliński, M., Kostrzewa-Rutkowska, Z, et al. 2017, MNRAS, 465, L114
Yao, Y., & Gezari, S. 2022, ATel, 15751, 1
Yao, Y., Lu, W., Guolo, M., et al. 2022, ApJ, 937, 8
Yao, Y., Lu, W., Harrison, F., et al. 2024, ApJ, 965, 39
Yao, Y., Ravi, V., Gezari, S., et al. 2023, ApJL, 955, L6
Yao, Y., Wang, Q. D., & Nan Zhang, S. 2005, MNRAS, 362, 229
Yuan, W., Zhang, C., Chen, Y., & Ling, Z. 2022, in Handbook of X-ray and Gamma-ray Astrophysics, ed. C. Bambi & A. Santangelo (Singapore: Springer), 86
Zauderer, B. A., Berger, E., Soderberg, A. M., et al. 2011, Natur, 476, 425